On the Integration of Deformation and Relief Measurement using ESPI

by

David I. Farrant

A Doctoral Thesis
submitted in partial fulfilment
of the requirements for the award of
Doctor of Philosophy
of
Loughborough University

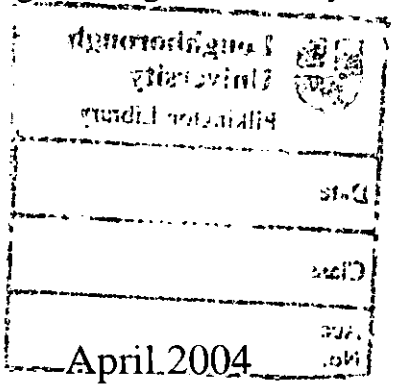

April 2004

Abstract

On the Integration of Deformation and Relief Measurement using ESPI

David I. Farrant

The combination of relief and deformation measurement is investigated for improving the accuracy of Electronic Speckle-Pattern Interferometry (ESPI) data. The nature of sensitivity variations within different types of interferometers and with different shapes of objects is analysed, revealing significant variations for some common interferometers. Novel techniques are developed for real-time measurement of dynamic events by means of carrier fringes. This allows quantification of deformation and relief, where the latter is used in the correction of the sensitivity variations of the former.

Acknowledgements

This work was conducted at Loughborough University, Leicestershire UK and at CSIRO Industrial Physics, Lindfield, Australia. My supervisors at Loughborough were Drs Jon Petzing and John Tyrer and my director of research was Dr Jon Huntley, to whom I am eternally grateful for proposing the topic, for their help in setting up some of the experiments, and for their advice and guidance during the research and the thesis. My gratitude also extends to Dr Bob Oreb of CSIRO, my external supervisor, for much valuable advice during the course of the work, including the published papers. Thanks as well to Dr Christopher Walsh, formerly of CSIRO, for helping to get the research up and running.

I also enjoyed numerous stimulating discussions on matters optical with Abundio Davila, Guillermo Kaufmann, Kieran Larkin and Jan Burke. Furthermore, my appreciation goes to Philip Fairman for local-unwrapping software and Toshiyuki Takatsuji for FTM software, which were used to process some of the images herein.

Thanks are due to my family and friends for their support and encouragement. In particular, Ruimin, for her love and for providing an environment that allowed me to devote more time than otherwise possible to the research. Thanks also to Claire—who arrived in the middle of everything—for providing inspiration (without proving too much of a distraction). Finally, I am also grateful to my parents and brother for their encouragement.

ESPI (es-pē′) *abbrev.* Electronic Speckle-Pattern Interferometry; an electro-optical measurement technique.

espy (es-pī′) *v.t.* to catch sight of; to see at a distance; to discern; to perceive.

Contents

ABSTRACT I

ACKNOWLEDGEMENTS II

CONTENTS III

GLOSSARY V

1 INTRODUCTION 1

2 ESPI MEASUREMENT 11

2.1 Fringe Formation 11
2.1.1 Correlation Fringes 13
2.1.2 Speckle Size 14
2.2 Deformation Measurement 15
2.2.1 Out-of-Plane Deformation 15
2.2.2 In-Plane Deformation 16
2.2.3 Deformation Sensitivities 17
2.3 Profilometry Measurement 18
2.3.1 Projected Fringe Profilometry 19
2.3.2 Correlation Fringe Profilometry 20
2.4 Dynamic Measurement 23
2.4.1 Harmonic Vibrations 24
2.4.2 Transient Vibrations 24
2.5 Phase Demodulation 26
2.5.1 Fringe Fitting 26
2.5.2 Temporal Phase Shifting 27
2.5.3 Spatial Phase Shifting 28
2.5.4 Carrier Fringes 28
2.5.5 Other Techniques 31
2.6 Summary 31

3 CARRIER FRINGES 33

3.1 Carrier Theory 33
3.1.1 Shift Theorem 34
3.2 Carrier Modulation 35
3.2.1 Piezoelectric Transducer 35
3.2.2 Galvanometer 36
3.2.3 Rotating Mirror 36
3.2.4 Dual-Pulsed Laser 37
3.2.5 Pockels Cell 38
3.2.6 Liquid Crystal Device 38
3.2.7 Acousto-Optic Modulator 41
3.2.8 Acousto-Optic Deflector 43
3.3 Carrier Demodulation 58
3.3.1 Fringe Visibility 58
3.3.2 Phase Calculation 60
3.3.3 Strain Calculation 62
3.3.4 Phase Unwrapping 65
3.4 Summary 67

4 SENSITIVITY ANALYSIS 68

4.1 Out-Of-Plane Interferometer 70
4.1.1 Geometry 70
4.1.2 Sensitivity Equations 72
4.2 In-Plane Interferometer 75
4.2.1 Geometry 75
4.2.2 Sensitivity Equations 77
4.3 Sensitivity Errors 78
4.3.1 Ratiometric Parameterisation 79
4.3.2 Out-of-Plane System 79
4.3.3 In-Plane System 86
4.4 Summary 90

5 CARRIER EXPERIMENTS 91

5.1 Harmonic Vibrations 91
5.1.1 Cylindrical Object 92
5.1.2 Internal Combustion Engine 98
5.2 Transient Vibrations 108
5.2.1 Metal Plate 109
5.3 Summary 120

6 CONCLUSIONS 121

6.1 Further Work 125

APPENDIX A: FOURIER STRAIN CALCULATION 127

A.1 Differentiation 128
A.2 Integration 133
A.3 Carrier Demodulation 134

APPENDIX B: SENSITIVITY CALCULATION 138

PUBLICATIONS 146

BIBLIOGRAPHY 147

Glossary

AOD Acousto-Optic Deflector.

AOM Acousto-Optic Modulator.

BS Beamsplitter.

CCD Charge-Coupled Device (camera).

ESPI Electronic Speckle-Pattern Interferometry.

FDT Fourier Derivate Theorem.

FFT Fast Fourier Transform.

FIT Fourier Integral Theorem.

FTM Fourier Transform Method.

GM Galvanometer.

HI Holographic Interferometry.

IP In-Plane sensitive interferometer.

LCD Liquid Crystal Device.

LDV Laser Doppler Velocimetry.

OOP Out-of-Plane sensitive interferometer.

PT Piezoelectric Transducer.

RM Rotating Mirror.

1 Introduction

Across the spectrum of industry and research there are many occasions where an understanding of the mechanical properties of materials and structures is fundamental to the development of new technologies and devices. For example, measuring the strength of materials or the deformation of structures. In these cases there may be a desire to minimise strains, reduce deflections, locate defects or identify failure modes. Adjunct to this are requirements for quality-control testing of production line items, and the testing of objects currently in use to determine their ongoing durability and fitness. The latter may include bridges, pipes, aircraft panels and artworks.

This thesis is primarily concerned with developing and analysing methods for the quantitative measurement of deformation and shape, and improving the accuracy of such methods, for both static and dynamic events.

An early method for measuring some of the above parameters, and one that is still in use today, is mechanical strain gauges. These attach to the object surface and produce a change in electrical resistance with compression or extension as the surface deforms. While strain gauges are accurate, they only provide localised information. Additionally, they may damage the surface of the object, and in the presence of high accelerations they can detach from the surface.

The advent of the laser facilitated a new range of practical measurement techniques, allowing the physical properties of objects to be optically measured through temporal or spatial changes in optical phase. Being optical, they offer non-contact capabilities and relatively rapid deployment. The non-contact aspect is important for susceptible surfaces (e.g. artworks), or inaccessible environments (e.g. high temperatures).

The coherent nature of laser light gives rise to the 'speckle effect', whereby the light scattered by an 'optically rough' surface (roughness larger than the optical wavelength) has random amplitude and phase, giving rise to an interference pattern that is speckled in appearance. The speckle effect occurs for almost all natural surfaces and many man-made surfaces, polished optics being one exception. To extract meaningful phase data, the speckle noise is usually minimised by using interferometric means; that is, comparing a perturbed wavefront with its unperturbed state and measuring the difference.

One optical technique, known as laser Doppler velocimetry (LDV), measures the change in frequency due to Doppler-shifting of a light beam reflected from a vibrating surface, providing information about the velocity (or displacement) of a surface point[1] or in fluids.[2] This is a fast technique, with the constraint that it is highly localised (unless a scanning system, multi-beam system, or streak camera system[3] is used). The principle of LDV is shown in Fig. 1.1. For a surface vibrating with velocity v, and scattering light of wavelength λ and frequency f, then the Doppler frequency shift is given by $\Delta f_D = 2v/\lambda$. This beam is mixed on the photodetector with a frequency-shifted version of the reference beam, $f+f_R$. The frequency of the photodetector output signal is equal to the frequency difference of the two incident beams. The reference beam provides a carrier frequency, allowing determination of both the phase (direction) and amplitude of the surface motion.

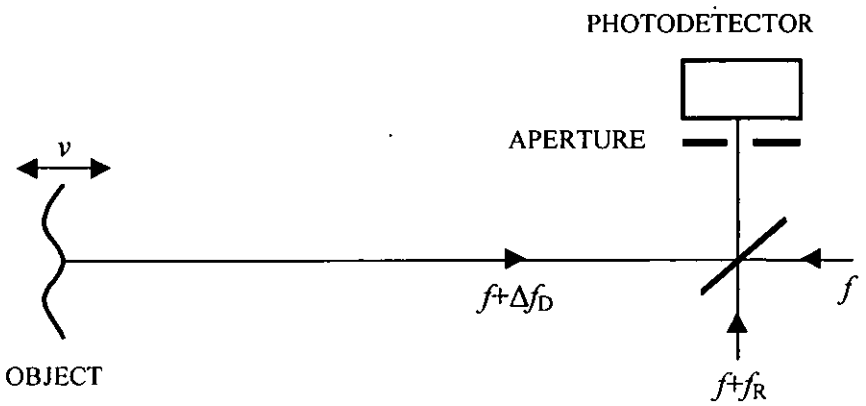

Fig. 1.1: Laser Doppler velocimetry configuration.

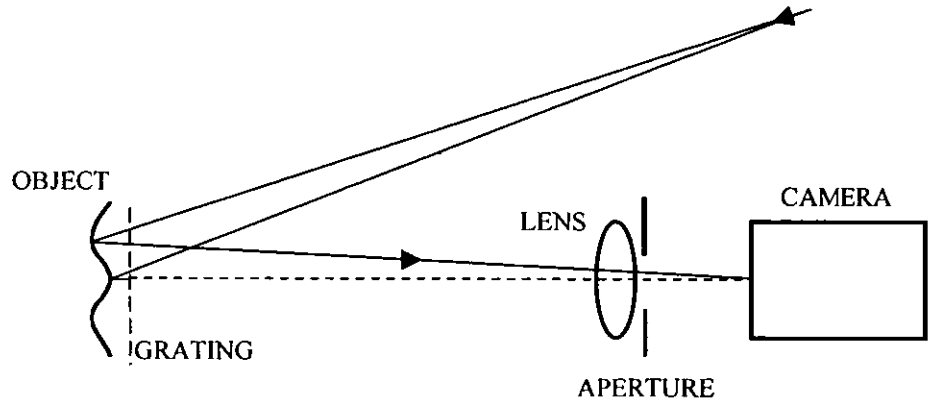

Fig. 1.2: Moiré configuration.

A number of two-dimensional (2D, 'whole-field' or imaging) techniques exist for structural measurements. One such method is moiré, which involves the correlation of two gratings (or patterns) to produce secondary fringes related to the object deformation.[4] A shadow moiré system for measuring out-of-plane (OOP, or along the observation axis) features such as object shape, or changes in shape, is shown in Fig. 1.2. Here, moiré fringes related to surface shape are formed by interaction of the grating with its shadow, and observed with a camera (digital or photographic). For measuring in-plane (IP) deformations (in the plane of the object, or lateral), a pattern is usually physically applied to the surface. Movements of the surface correlate with movements of the pattern, moiré fringes being formed on superposition with a reference grating.

Moiré is usually used with white (incoherent) light, thus avoiding speckle noise, and allowing large structures to be illuminated (e.g. using flash lamps). It generally has lower sensitivity to deformation than laser-based techniques, although this can be an advantage in relatively noisy environments such as factories and outdoors.

Another 2D technique is speckle photography, also known as intensity speckle.[5-7] As shown in Fig. 1.3, an object is illuminated with laser light, forming a speckle pattern that is recorded by the camera. If images are taken before and after IP deformation, then two largely identical but slightly displaced speckle patterns will result. The speckle shifts, and hence object deformation, can be calculated by, for example,

discrete cross-correlation. This offers similar deformation sensitivity as moiré, but does not require grating artefacts, and is more amenable to computer processing.

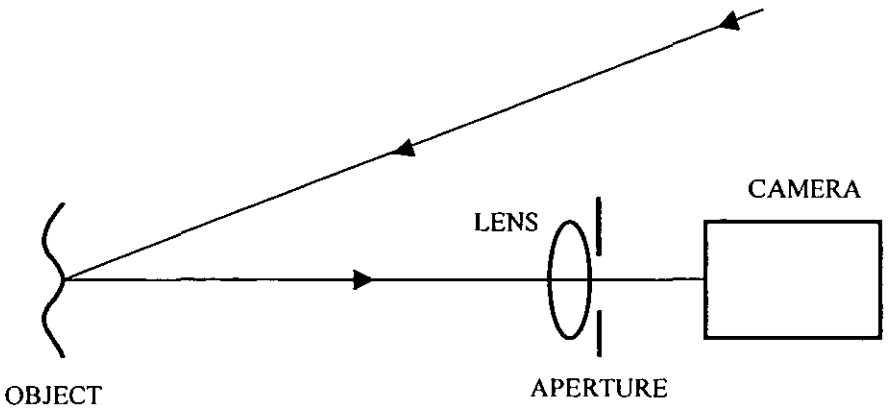

Fig. 1.3: Speckle photography configuration.

An optical method having higher sensitivity to deformation is holographic interferometry (HI).[8] This employs, for example, a photographic plate to record a hologram of an object, using an object and reference beam, as shown in Fig. 1.4. When the object deforms, a set of interference fringes forms, directly related to the surface displacement. Unlike the sparse data of the aforementioned strain gauges and LDV's, HI offers a dense array of data over the surface of objects. Such 'whole field' data is important, for example, to measure complex vibration modes, where it is necessary to establish the sign of the deformation at one position on the object relative to another (something that point techniques cannot readily accomplish).

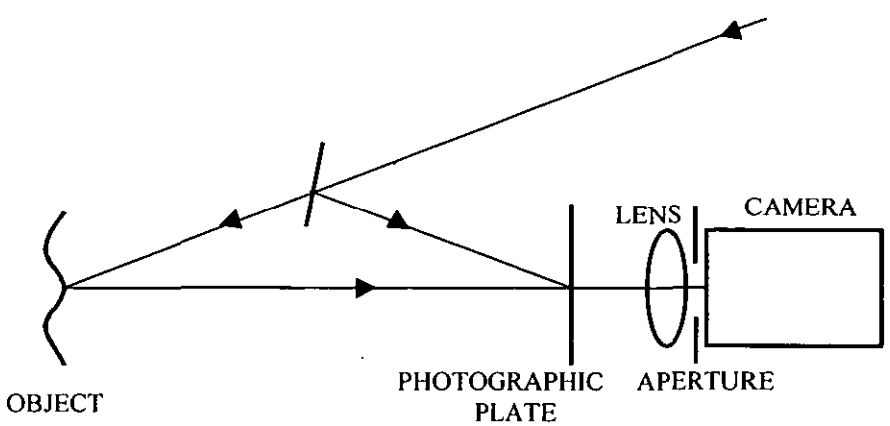

Fig. 1.4: Holographic interferometry configuration.

The high resolution of photographic plates (typically 1000—10 000 line-pairs/mm) serves to minimise speckle noise. However, the relatively long exposure times require a very stable environment (or a pulsed laser), and the chemical or thermal development process can be messy and/or time consuming.

To circumvent some of the limitations of HI, a technique known as Electronic Speckle-Pattern Interferometry (ESPI)[9] was developed in the early 1970s. This has many parallels with HI, the main difference being that it uses an electronic camera to record the interference pattern, as shown in Fig. 1.5.† Such cameras have relatively low spatial resolution (50—100 line-pairs/mm), producing higher levels of speckle noise than HI. However, in many situations this is acceptable, outweighed by the convenience of short exposure times and no development time. The short exposures also sometimes permit measurements in ambient light. ESPI and HI sometimes require a diffuse object surface-finish to reduce specular reflections and/or increase the average surface reflectance. For these instances, the object surface can be coated with white powder or with retro-reflective tape, without causing damage to the surface.

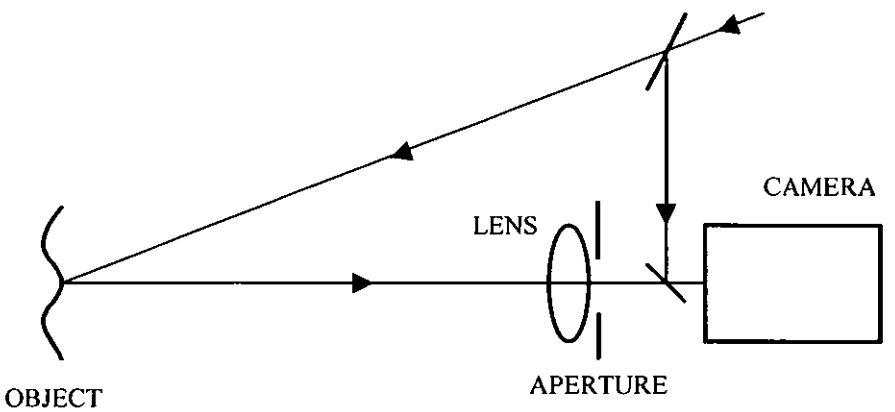

Fig. 1.5: Speckle interferometry configuration.

Apart from measuring deformation, the most common use of ESPI is to measure strain. Strain is particularly important in materials science; it is the lingua franca of fracture mechanics and finite-element analysis (FEA) software packages.

† For this reason ESPI is sometimes known as TV Holography, although it is not restricted to the use of TV-format cameras. ESPI is also known as Electro-optic Holography and Digital Speckle-Pattern Interferometry.

Strain is a function of the derivative of deformation. In practice, the differentiation is produced either numerically or optically. The latter is usually known as shearography[9] or speckle-shearing interferometry, and uses a shearing interferometer of the type shown in Fig. 1.6. This does not use a reference beam, but instead laterally shears the object beam with itself by means of a beamsplitter and two mirrors. As a common-path interferometer, it is largely insensitive to environmental effects, so sometimes finds favour in industrial measurements. In such cases, deformation data is obtainable by numerically integrating the native strain data.

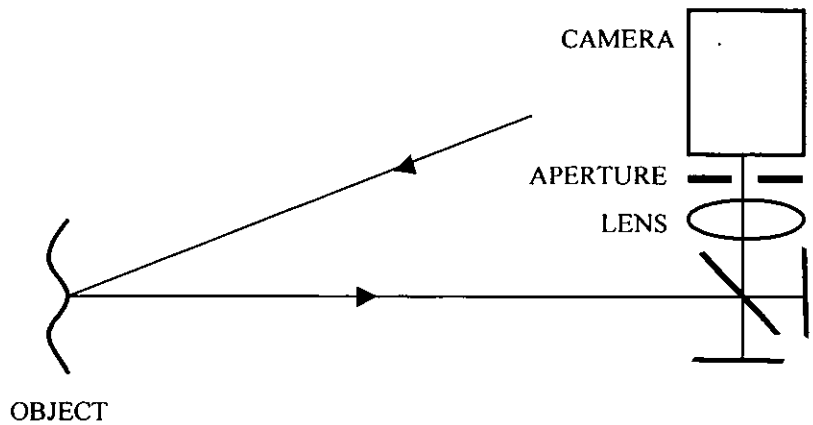

Fig. 1.6: Speckle-shearing interferometry configuration.

A brief summary of key aspects of the above measurement techniques is given in Table 1.1. Based on deformation sensitivity, spatial coverage, fast cycle times and setup times, ESPI finds use in many applications, and is well suited to the aims of this thesis. ESPI is suitable for measuring both static and dynamic deformations, the latter being of particular interest to industry. For example, analysing vibrating structures to identify the nature of the vibration, so that it can be enhanced or attenuated. Dynamic events can be either harmonic or transient in nature, the measurement of which is performed by pulsed lasers, or by strobing a continuous-wave laser through external modulation of the beam.

Using ESPI, any optical path-length difference can be measured including refractive index changes, therefore permitting optically-transparent solids to be studied as well as gas and liquid flows.

Feature	ESPI	HI	Speckle Photography	Moiré	LDV	Strain Gauge
Native Mode	Deformation	Deformation	Deformation	Deformation	Velocity	Strain
Usual component	IP/OOP	IP/OOP	IP	IP/OOP	OOP	IP
Sensitivity	High	High	Medium	Medium	High	High
Spatial coverage	High	High	High	High	Low[1]	Low
Spatial resol'n	Medium	High	Medium	Medium	High	Low
Temporal resol'n	Medium[2]	Medium[2]	Medium[2]	Medium[2]	High	High
Static events	✓	✓	✓	✓	✓	✓
Dynamic events	✓	✓	✓	✓	✓	✓
Setup time	Medium	Medium	Medium	Medium	Short	Long
Cycle time	Short	Long	Short	Short	Short	Short
Non-contact	✓	✓	✓	✓	✓	×
Daylight use	✓	×	✓	✓	✓	✓

1. Multi-point or scanning systems can offer medium spatial coverage.
2. Fast-framing cameras can offer high temporal resolution.

Table 1.1: Structural measurement methods and their features.

The field of speckle interferometry has matured to the extent that several textbooks have been produced in the last decade or so. For a general introduction to speckle interferometry and the other techniques mentioned above see: Sirohi,[9] Rastogi,[5] Williams,[4] and Jones and Wykes;[10] for interferogram analysis see Robinson and Reid;[11] and for speckle theory see Dainty.[12]

The early ESPI systems were mostly qualitative.[13,14] They used video tape for image storage and analog electronics for processing. It was not until the early 1980s that systems with digital storage and processing were demonstrated.[15] Apart from allowing greater speed and flexibility, they also offered improved accuracy in extracting quantitative phase information. In the intervening years until the present, considerable fundamental and applied research have helped to establish ESPI firmly in the stable of non-destructive testing methodologies.

Despite some level of maturity, a better understanding of speckle interferometry is still being realised through theory and experiment. It is a focus of this thesis to extend the capabilities and accuracy of speckle interferometry, to increase its utility for deformation and shape measurement.

ESPI can be employed for shape measurement, although it has not been used extensively for this purpose, possibly because of its limited accuracy. However, shape is important when measuring deformation (or strain) on curved or irregularly-shaped objects. This is because the local sensitivity vectors of deformation are a function of both the illumination and observation directions, which vary with the three-dimensional (3D) position of each point of the object surface. Accordingly, the direction of the sensitivity vectors varies across an object and also with the relief of the object, unless collimated illumination is used, which is mostly impractical. Therefore, accurate deformation vectors can only be recovered if the surface shape is also known. Indeed, as the usage of ESPI has grown, so have questions concerning its accuracy.

One of the objectives of the present study is to investigate the behaviour of the sensitivity vector for different interferometer configurations and object shapes. This is something that has hitherto been addressed in an ad hoc manner, either very sparsely, or very specific to a particular interferometer. It is envisioned that a more comprehensive understanding of sensitivity variations will identify situations where such effects limit a system's accuracy, and ultimately lead to the design of improved interferometers.

A second aim is to develop and analyse methods for producing interferometric carrier fringes, as a means of measuring the relief and deformation of objects within a single configuration of interferometer, in order to apply sensitivity corrections to deformation data.

The third aim is to apply such carriers in real-time to the measurement of dynamic events and address the attendant problems of speed, fringe visibility and phase demodulation.

Chapter 2 commences with a review of the interferometric theory and techniques pertinent to the aforementioned aims; namely: fringe formation, deformation and relief measurement (and the sensitivity ranges of both), dynamic measurement, and phase demodulation. This chapter also serves to identify the strengths and limitations of existing techniques, and establishes some of the theoretical framework for subsequent chapters.

In Chapter 3 the subject of carrier fringes is covered in detail. It begins with a brief treatment of carrier theory, from both geometrical optics and wave optics foundations. Then, practical methods for dynamic carrier phase modulation are presented and analysed, including a number of novel techniques involving galvanometer mirrors, liquid crystal devices and acousto-optic devices. For the latter, new configurations are derived, which open-up a whole new class of coherent applications. Lastly, this chapter deals with the issue of phase demodulation for extracting the object phase (e.g. deformation) from the carrier fringes. A novel algorithm for enhancing poor-visibility fringes is presented, along with phase calculation, strain calculation and phase unwrapping algorithms.

Chapter 4 is devoted to the subject of noncollimated interferometer sensitivity variations. A unique, comprehensive 3D model of the component sensitivities for both in-plane and out-of-plane interferometers is developed. Sensitivity equations are derived, along with error functions for the three orthogonal components of the displacement vector. Then, a novel, scalable parameterisation is developed to make the model generic to a wide range of interferometers. Finally, the sensitivity variations are plotted and discussed for various interferometer geometries. A systematic and analytic approach is adopted throughout to elucidate the sensitivity behaviour and provide scalability.

The new phase measurement and sensitivity analyses are then brought together in Chapter 5, where a number of experiments are conducted to demonstrate their practicality and efficacy. Two harmonically vibrating objects are measured for both deformation and relief: a cylinder, as a form of deterministic object; and an internal combustion engine, as a practical example of a vibration-minimisation problem. A

transiently vibrating object, a metal plate, is measured as an example of real-time implementation of carrier fringes, with a dual-pulsed laser.

Finally, the appendices contain simulations of the Fourier derivative/strain theory of Chapter 3, plus Mathcad code for interferometer sensitivity calculations.

2 ESPI Measurement

The measurement of object deformation and relief using ESPI covers a broad range of techniques. However, many of these techniques are based on certain fundamental principles of optical interferometry. In this chapter, some of the essential precepts of ESPI measurement are reviewed in the context of the thesis' research, including an analysis of their features and limitations. This provides a foundation and direction for the theory and measurements in subsequent chapters.

An ESPI system comprises a mixture of optics, electronics hardware and software. A flow chart delineating the major elements involved in acquiring and processing ESPI data is shown in Table 2.1. Aspects of acquisition and processing as they relate to deformation and relief measurement, and the combination thereof, are now examined.

2.1 FRINGE FORMATION

As an essential precursor to forming ESPI (or HI) fringes that relate to, for example, contours of deformation, 'primary' interferograms must first be acquired. A primary interferogram (or specklegram) consists of a coherent addition of a direct portion of the illuminating laser beam (reference beam) with a portion that has been scattered by the object (object beam). For in-plane ESPI and shearography, the reference beam is 'virtual', being formed by self-reference of the object beam/s. A primary interferogram has a very similar appearance to an intensity speckle field formed with only an object beam, but has different speckle statistics[16] and is witnessed as a 'live' speckle field, highly sensitive to object movement.

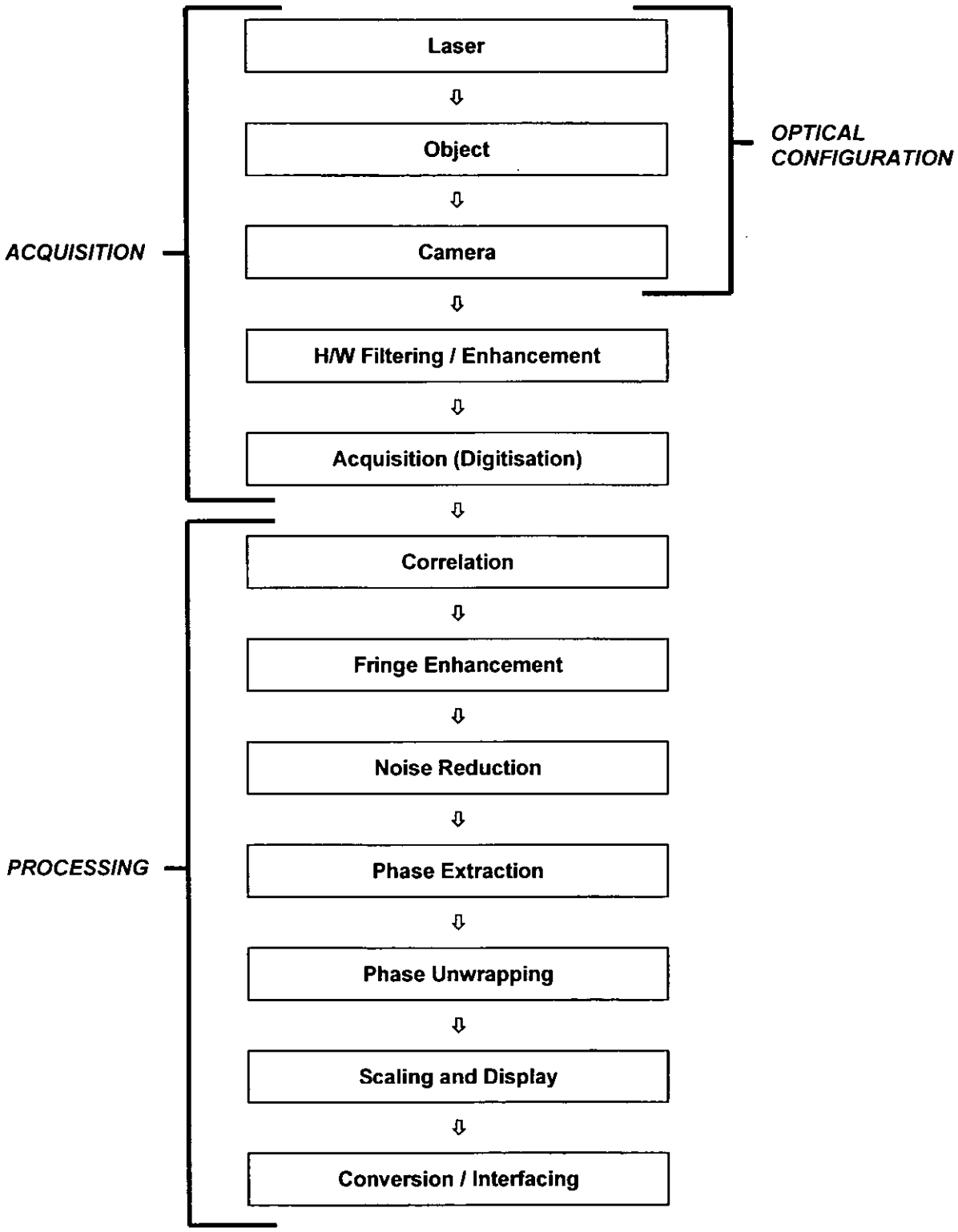

Table 2.1: ESPI acquisition and processing.

2.1.1 Correlation Fringes

ESPI fringes representing path-length changes (e.g. displacement) are formed by correlating the images of two primary speckle interferograms, one recorded before (I_1) and one recorded after (I_2) deformation. The correlation produces a 'secondary' interferogram that contains the speckled fringes.† Depending on the type of measurement, the correlation can produce very-low visibility fringes, which makes processing difficult. The two main correlation methods are subtraction and addition. Subtraction of the two primary interferograms (more properly, *difference* or *modulus of subtraction*, to convert negative values so they can be displayed on a monitor) effectively removes the background and fixed speckle noise and gives good-visibility fringes. Conversely, addition fringes are much noisier and have lower visibility. The interferogram I_S for subtractive ESPI can be represented[10] by

$$\begin{aligned} I_S &= I_2 - I_1 = 2\sqrt{I_o I_r}\left[\cos(\psi + \Delta\phi + \Delta\alpha) - \cos\psi\right] \\ &= 4\sqrt{I_o I_r}\,\sin\left(\frac{\Delta\phi + \Delta\alpha}{2}\right)\sin\left(\psi + \frac{\Delta\phi + \Delta\alpha}{2}\right) \end{aligned} \tag{2.1}$$

where I_o and I_r are the object and reference beam irradiances respectively, ψ is the random speckle phase, $\Delta\phi$ is the phase due to deformation and $\Delta\alpha$ is the phase introduced by rigid-body motion, environmental disturbances or a carrier term. Each of the above variables is spatially (x, y) dependent (omitted here for clarity).

In certain circumstances such as fast acquisitions, it is not possible to acquire the two primary interferograms in separate camera fields. In these cases the primary interferograms are instead incoherently added on the camera sensor, within a single camera field. The interference fringes for additive ESPI can be described[10] by

$$\begin{aligned} I_A &= I_1 + I_2 = 2(I_o + I_r) + 2\sqrt{I_o I_r}\left[\cos(\psi + \Delta\phi + \Delta\alpha) + \cos\psi\right] \\ &= 2(I_o + I_r) + 4\sqrt{I_o I_r}\,\cos\left(\frac{\Delta\phi + \Delta\alpha}{2}\right)\cos\left(\psi + \frac{\Delta\phi + \Delta\alpha}{2}\right) \end{aligned} \tag{2.2}$$

† For this reason ESPI is sometimes known as Electronic Speckle-Pattern Correlation Interferometry.

The first term on the right-hand side of Eq. (2.2), which is not present in Eq. (2.1), represents a background intensity level that reduces fringe visibility and increases noise (particularly the I_o term, since the I_r term is usually spatially filtered and hence has low noise). The ψ terms in the same equation ensure that even without deformation ($\Delta\phi = 0$) or other phase modulation ($\Delta\alpha = 0$), the addition fringes will be noisy, unlike subtraction fringes that are nominally zero (dark) when no deformation is present, to wit the first sine term in Eq. (2.1). However, by use of suitable algorithms (section 3.3.1), addition fringes with visibility approaching that of subtraction fringes can be achieved.

Another method of producing fringes is to perform a spatial numerical correlation on the two primary speckle maps.[17] This produces uniform fringes of good visibility even when the speckle maps are of low or varying quality (as is sometimes the case when using pulsed lasers), but is computationally expensive and can only be used when both maps (I_1 and I_2) are available separately (i.e. when using subtraction).

2.1.2 Speckle Size

The mean size[16] of the speckles in the image plane of the camera is inversely proportional to the lens aperture, and is given by

$$\sigma_s = 1.2\lambda F(1+M) \tag{2.3}$$

where F is the aperture ratio (f/number) and M is the magnification of the imaging system (image size to object size). The speckles should be large enough such that they are at least partially resolved by the camera pixels. Small speckles will cause increased decorrelation,[16] and hence reduced fringe visibility with large deformations. If the speckles are too large, such that their size approaches that of the fringe spacing, then fringe visibility will again decrease. Another trade-off is that large speckles require a small camera aperture, which is less light efficient.

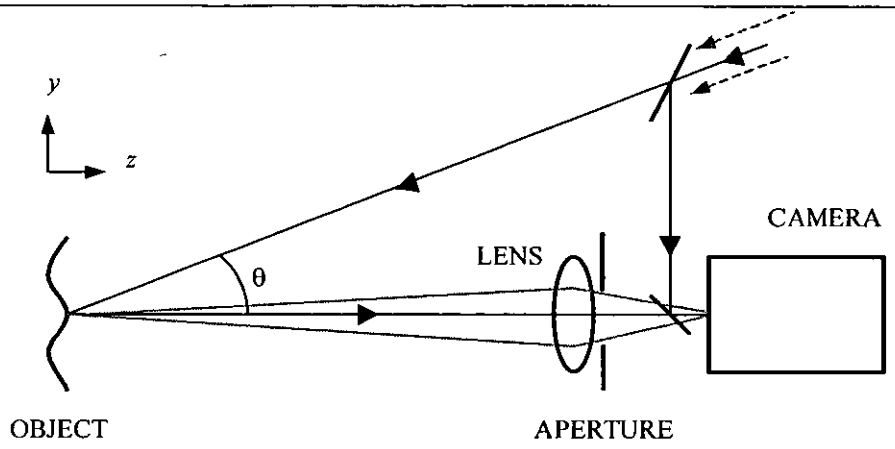

Fig. 2.1: ESPI OOP deformation measurement configuration.

2.2 DEFORMATION MEASUREMENT

Object deformation can be decomposed into three orthogonal vectors of displacement for each point on the surface. The orientation of the coordinate system is arbitrary, but for convenience, and by convention, it is usually defined as out-of-plane (perpendicular to the plane of the object, or along the optical axis), and the two orthogonal in-plane (lateral) directions. Usually only one component of displacement is measured at one time, although all three can be measured simultaneously using an apposite configuration as outlined in section 2.5.4, and the corresponding theory of section 4.1.1.

2.2.1 Out-of-Plane Deformation

A typical out-of-plane (OOP) deformation-measuring ESPI configuration is shown in Fig. 2.1. Light scattered by the object forms a speckle field that is interfered with a reference beam and registered on a camera in the image plane of the lens. Deformation of the object produces a phase change at the camera directly proportional to the component of deformation in the direction of the sensitivity vector, which lies along the bisector of the illumination and observation directions (see section 4.1.1 for further information on sensitivity vectors). Then, the phase change $\Delta\phi(x, y)$ along the axis of observation due to axial (z) deformation $d_3(x, y)$ is given[9] by

$$\Delta\phi(x,y) = \frac{2\pi}{\lambda} d_3(x,y)(1+\cos\theta) \tag{2.4}$$

where λ is the irradiation wavelength, θ is the angle of the irradiating beam from the observation direction. Thus, one fringe represents a deformation of

$$d_3(x,y) = \frac{\lambda}{1+\cos\theta} \tag{2.5}$$

2.2.2 In-Plane Deformation

An example of an in-plane (IP) ESPI configuration is shown in Fig. 2.2. The object is irradiated with two beams inclined at equal and opposite angles θ. The phase change at each point $\Delta\phi(x, y)$ due to lateral deformation $d_2(x, y)$ in the y-direction is given[9] by

$$\Delta\phi(x,y) = \frac{4\pi}{\lambda} d_2(x,y)\sin\theta \tag{2.6}$$

Here the vectors representing the irradiating beams will change differentially only for y-direction displacements. Hence, this configuration is insensitive to OOP components and IP components orthogonal to the plane of incidence, i.e. IP components in the x-direction, $d_1(x, y)$.

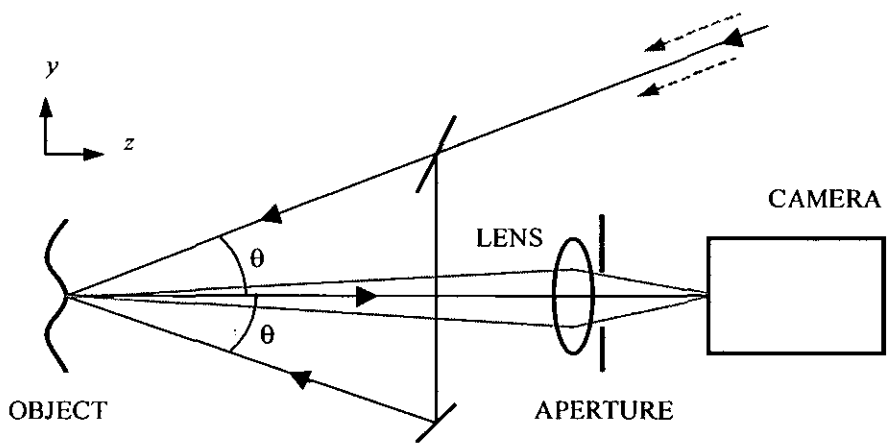

Fig. 2.2: ESPI IP deformation measurement configuration, with sensitivity in the y-direction.

2.2.3 Deformation Sensitivities

The sensitivity of an interferometer can be defined as the rate of phase change for a given deformation, i.e. $\Delta\phi(x, y) / d(x, y)$. The fundamental sensitivity variation for deformation measurements is due to the angle θ, as given in Eqns. (2.4)–(2.6), assuming the wavelength is constant. Thus for an OOP interferometer, the sensitivity will be highest on-axis, reducing as the source moves off-axis. Owing to the unity factor in the denominator of Eq. (2.5), the change in sensitivity is limited to a factor of two when θ ranges over 0–90° (further desensitisation for measuring larger deformations can be achieved by also changing the observation angle as is shown in Chapter 4). The sensitivity variation (relative to $2\pi/\lambda$) with respect to θ is plotted in Fig. 2.3, in which the cos θ Lambertian reflectivity of the object (assuming a diffusely-reflecting surface) is also plotted, assuming a reflectivity of one at normal incidence. Thus, as θ increases, the light efficiency will reduce, dropping by an order of magnitude once θ reaches 84°.

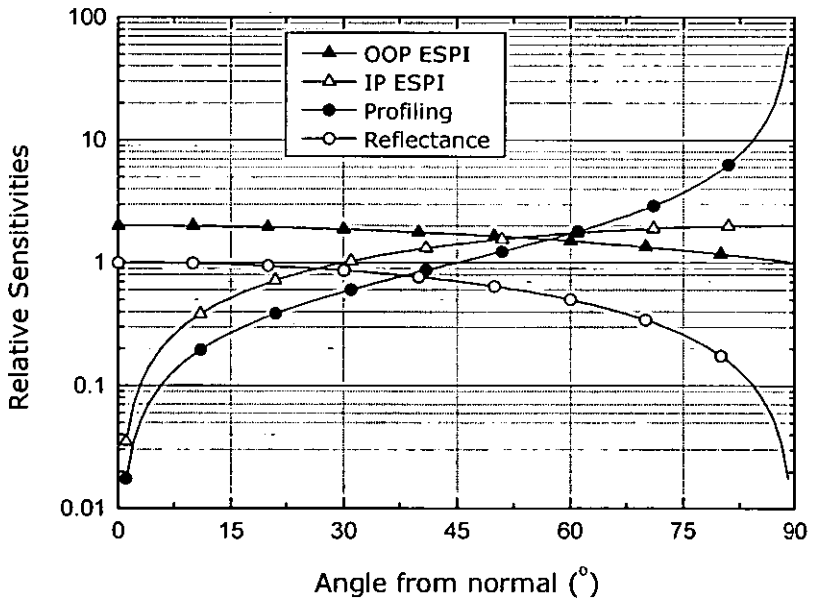

Fig. 2.3: Comparison of relative sensitivities (relative to $2\pi/\lambda$) versus angle θ for deformation and profiling measurements.

For an IP interferometer, the sensitivity is maximal off-axis and reduces as the two sources move on-axis, i.e. the reverse of the OOP case. Unlike the OOP case, the lower end of the IP sensitivity is unbounded, as shown in Fig. 2.3.

Equations (2.4)–(2.6) are valid for collimated (plane wavefront) illumination. However, because of the large size of some objects, or the constrictions of measurement environments, noncollimated (divergent) illumination is often used. In this case, the above equations are only an approximation since the sensitivity vector of deformation is a function of both illumination and observation directions, which vary across an object and with the relief of an object. Chapter 4 is devoted to a detailed analysis of the sensitivity variations that occur when using noncollimated illumination.

2.3 PROFILOMETRY MEASUREMENT

ESPI, as used for deformation measurement, is a differential technique that measures the change in the shape of an object, usually over a small range (nm—μm). Profilometry, however, measures the actual shape or relief of an object, usually over larger ranges (μm—mm). Speckle has not been used extensively for profiling, probably because the noisy fringes limit the accuracy. However, the accuracy is adequate for many applications, including combined deformation and shape measurement.

Whole-field optical profilometry (i.e. excluding point- and line-scanning techniques) is usually achieved through one of two different means: projected fringes[18] or correlation fringes,[19,20] both of which can be implemented with an ESPI system. Other techniques that are available include moiré,[21-23] stereo,[24] and low-coherence interferometry[25] (LCI)—sometimes known as coherence radar[26] or white-light interferometry.[27] Moiré is a simple configuration, but leaves a residual fringe pattern superposed with the contour fringes, making automatic processing of the fringes difficult. Stereo is computationally intensive and requires the use of two cameras which must be accurately calibrated. LCI can measure large height differences ($z \gg \lambda$) with interferometric resolution, and can also cope with discontinuous surfaces and/or spatially-isolated surfaces. However, LCI requires the acquisition of a large number of

images which is expensive timewise and costwise, and it is difficult to apply when the height range is greater than the range of a piezoelectric transducer (typically less than a millimetre).

2.3.1 Projected Fringe Profilometry

Projected fringe methods are based on triangulation. This involves projecting a set of fringes onto the object and then observing the deformation of the fringes from a viewing angle different to the projection angle. The phase of the fringes—in this case related to the shape of the object—can be calculated using phase shifting (see section 2.5.2) or Fourier methods (see section 2.5.4). The phase change $\Delta\phi$ is related to object shape z by[28]

$$\Delta\phi = \frac{2\pi}{\lambda_o} z \tan\theta \tag{2.7}$$

where λ_o is the spatial wavelength of the fringes on the object (perpendicular to the direction of viewing) and θ is the angle of projection from the object normal, and assuming viewing at normal incidence. Note that due to the projection angle, some surfaces will have regions that are in shadow. The above equation assumes the illumination is collimated, i.e. the fringes are equispaced. When the illumination is noncollimated, the equations of Bremand[29] or Oreb[18] can be used. The fringes can be formed by simple interference (e.g. Farrant[30]) and then projected onto the surface of the object. The fringes in this case are visible on the object. The fringes can also be formed using a physical grating,[18] or an electro-optic modulator (e.g. spatial light modulator[31]), although these are not interferometric techniques.

Plotted in Fig. 2.3, along with the deformation sensitivities, is the profiling sensitivity, relative to $2\pi/\lambda_o$. This varies with angle θ over a wide range, allowing a combined deformation and profilometry system to be optimised for the profiling sensitivity without compromising the deformation sensitivity appreciably.

The range of this technique can be extended (while maintaining its resolution) by using multiple spatial wavelengths. These can be applied sequentially (i.e. temporal

multiplexing) or simultaneously (i.e. spatial multiplexing). An example of the former is temporal phase unwrapping.[32] The latter can be effected with angular multiplexing[33] (e.g. gratings at different angles, separated by Fourier methods) or wavelength multiplexing[34] (e.g. gratings of different temporal wavelengths, separated by a colour camera).

2.3.2 Correlation Fringe Profilometry

Correlation fringes are formed by differential interference, and are thus not visible on the object. Here the incident beam is modulated between exposures, and shape fringes are formed upon correlation. This technique has the advantage that it can be used with only minor modifications to the optical configuration used for the displacement measurement.

The phase modulation can be produced in one of several ways. The laser wavelength or frequency can be varied (e.g. frequency tuning of a laser diode[20,35]), in which case the phase change is given by

$$\Delta\phi = \frac{2\pi}{\hat{\lambda}} z \tag{2.8}$$

where z is the height of the object and

$$\hat{\lambda} = \frac{\lambda_1 \lambda_2}{2|\lambda_1 - \lambda_2|\cos\theta} \tag{2.9}$$

is the synthetic wavelength, where θ is the angle of incidence of the beam from the object normal. For small changes in wavelength, $\Delta\lambda$, and $\theta = 0°$, the above can be approximated by

$$\Delta\phi = \frac{4\pi\Delta\lambda}{\lambda^2} z \tag{2.10}$$

The refractive index of the medium through which the object beam passes can be changed (by means of temperature or pressure, or a change of media such as two different liquids), here giving a phase change of

$$\Delta\phi = \frac{4\pi}{\lambda}|n_1 - n_2|z \tag{2.11}$$

where n_1 and n_2 are the two refractive indices.

The above correlation schemes rely on optical-path difference (rather than triangulation), so can operate at normal incidence, thus minimising the chance of shadowing.

As something of a hybrid technique,[19] the modulation can also be effected by incorporating a linear phase term into one of the beams (by means of translating the source or tilting the beam), or by tilting the object. This is the profiling method pursued in this thesis. It produces carrier fringes (upon correlation) modulated by the object shape, when the illumination and observation directions are non-coincidental (as with triangulation). Such carrier fringes are amenable to processing with Fourier methods, a feature that is also advantageous for reducing the speckle noise. However, the carriers are usually introduced by manual tilting. Preferably they should be generated using electro-optic modulators—essential for an automated system offering fast and repeatable measurements.

To derive an equation describing this method, it is first noted that the spatial wavelength λ_o on the object (perpendicular to the direction of viewing) is related to the spatial wavelength λ_s perpendicular to the direction of illumination by

$$\lambda_o = \frac{\lambda_s}{\cos\theta} \tag{2.12}$$

Substituting this into Eq. (2.7) gives

$$\begin{aligned}\Delta\phi &= \frac{2\pi}{\lambda_s} z\cos\theta\tan\theta \\ &= \frac{2\pi}{\lambda_s} z\sin\theta\end{aligned} \tag{2.13}$$

The spatial wavelength λ_s is determined[10] by the tilt angle α and temporal wavelength λ of the illumination beam:

$$\lambda_s = \frac{\lambda}{2\sin(\alpha/2)} \tag{2.14}$$

Now substituting this into Eq (2.13) and assuming α is small, then

$$\begin{aligned}\Delta\phi &= \frac{4\pi}{\lambda} z\sin\theta\sin(\alpha/2) \\ &\approx \frac{2\pi}{\lambda} z\sin\theta\sin\alpha\end{aligned} \tag{2.15}$$

Equation (2.15) is equivalent to Rodriguez-Vera *et al.*,[36] although derived in a different manner [i.e. $z = \lambda l/(\Delta s.\sin\theta)$, where l is source-to-object distance and Δs is source translation; now since $\sin\alpha \approx \Delta s/l$, this is then equivalent to Eq. (2.15)]. The method of tilting the object (instead of the beam) gives the same equation as Eq. (2.15) but for a factor of two on the right-hand side, because tilting the object changes the path length by a factor of two.[37]

Winther and Slettemoen[38] were the first to use an ESPI system for profiling, in which the depth contour fringes were induced by manually tilting the object beam. Ganesan and Sirohi[37] and Joenathan *et al.*[39] reported similar results, in this case by manually tilting the object—something that is not always practical or repeatable. One profiling approach using electro-optic modulators, in this case three acousto-optic modulators (AOM's), was presented by Blatt *et al.*,[40] although this is a moiré rather than a

correlation system. Wang *et al.*,[41] presented a system for combined shape and 3D deformation measurement. This used manual source translation for the shape measurement, and manual shutters to switch between multiple object beams for the deformation measurement. The authors also fitted a first-order polynomial to the deformation data, which was then differentiated to give strain values, although these were not corrected for the object shape. Wang and Krishnaswamy[42] demonstrated a complicated shape-measurement system for noisy environments using an AOM to strobe the illumination and a motorised tilting mirror to generate the carrier fringes. A PZT was used to generate a π phase-shift between frames, giving high contrast subtraction-of-addition fringes. A second PZT was employed to step the phase by $\pi/2$ so that the object height could be calculated by means of a phase-shifting algorithm. Manual decorrelation and frame averaging was used to reduce speckle noise in an effort to assist the phase-unwrapping process.

2.4 DYNAMIC MEASUREMENT

The measurement of dynamic (vibrationary) events is particularly important to industry. For example, characterising and attenuating disc brake vibration[43,44] in an effort to reduce brake 'squeal', or enhancing the vibration mode of ultrasonic cutting blades[45] to ensure faster, cleaner cutting. Dynamic events can be classified as those where the resulting fringe motion occurs faster than the eye can resolve. Devices such as strain gauges and LDV's can measure dynamic events in real-time, due to their one-dimensional (1D)/temporal nature. While ESPI is no match for the temporal resolution of LDV's, it can be used to capture real-time events, although the speed and/or number of samples are usually limited by the large (2D) volume of data involved. This problem can be circumvented somewhat by fast-framing electronic cameras[46] (e.g. 16 frames storage at rates of up to one million frames-per-second), which are now becoming available. Alternatively, due to the reasonably fast cycle time of ESPI (in the order of a camera field time, say 20 ms), dynamic events can be sampled in time, allowing a picture of their behaviour to be constructed over time. Some approaches of this type are examined in this section.

Another significant issue with ESPI is the interpretation of the data. ESPI data is generally in the form of fringes, which provide a good qualitative picture of deformation but the extraction of quantitative information is much more difficult, particularly so in dynamic measurements, as is discussed below and in Phase Extraction (section 2.5).

2.4.1 Harmonic Vibrations

When vibrations are harmonic (periodic) and pulsed illumination is being used, then if the illumination can be synchronised to the vibration, the subtraction ESPI method can be used by subtracting the vibration interferogram from an at-rest interferogram. This is known as stroboscopic ESPI[47,48] and can be used with temporal phase-shifting (section 2.5.2) to determine the phase and amplitude of the deformation. By varying the phase of the illumination pulse, different parts of the vibration cycle can be examined.[49] A pulse width equivalent to less than $\lambda/4$ of the wavefront change is required to freeze the motion and maintain fringe visibility. However, because the motion is periodic, multiple exposures can be made within one camera field time, increasing the photometric sensitivity over that of a single-exposure system (see Transient Vibrations below).

With continuous illumination and no synchronisation, time-averaged[10] fringes are obtained (assuming stationary and not traveling waves), whose visibility varies with the amplitude of deformation according to a Bessel function. Although this setup is simple it does not give the phase of the deformation (only the amplitude) and the high-order fringes have low visibility.

2.4.2 Transient Vibrations

Transient and/or non-periodic vibrations usually require a single light pulse to freeze the motion and cannot make use of multiple exposures for increased sensitivity. Therefore a pulsed laser is required, which can release a large amount of light energy in a short time interval. Sometimes a dual-pulse laser that can deliver two pulses in quick succession is preferred. This helps prevent rigid-body motion and environmental effects from corrupting the measurements.

Due to the short time intervals involved, transient events are usually captured using addition ESPI, whereby the primary interferograms are incoherently added on the camera array within one frame/field time. As mentioned in section 2.1, additive fringes are noisy and have low visibility. Their quality can be improved, however, by numerical processing as outlined in section 3.3.1.

Several authors have used subtraction ESPI for transient deformations by exploiting the characteristics of CCD cameras. For example, Spooren[50] used an interline-transfer camera to record a separate primary interferogram in each TV field.† The pulses were generated using a single laser, *Q*-switched twice within the flashlamp cycle, allowing pulse separations of 10 μs to 500 μs. Pedrini[51] extended the method by applying spatial phase-shifting (see section 2.5.3) to determine the phase distribution of the fringes, a technique that places stringent requirements on the alignment of the object and reference beams.

The interlaced structure of interline-transfer CCD cameras results in each field having typically half the spatial resolution (at least in the vertical dimension) obtainable with a comparable frame-transfer imaging sensor. This necessitates a larger speckle size to maintain correlation and hence a smaller camera aperture, which is less light-efficient. Also, owing to the field-transfer time of the camera, the pulse separation cannot be reduced below ~1 μs. Thus the price paid for the improved fringe visibility of the pulsed subtraction method is reduced spatial resolution of the image, loss of light, and a minimum pulse separation imposed by the camera. The spatial resolution problem can be solved using a frame-transfer camera, but this will increase the minimum pulse separation to several-hundred microseconds.

† This paper also includes a neat analysis of fringe visibility as a function of both pulse-to-pulse intensity ratio and reference beam rms contrast.

2.5 PHASE DEMODULATION

The irradiance of simple two-beam interference fringes can be represented by

$$I(x,y) = \bar{I}(x,y)\{1 + \gamma(x,y)\cos[\phi(x,y)]\} \tag{2.16}$$

where $\bar{I}(x, y)$ is the background (dc) intensity, $\gamma(x, y)$ is the fringe visibility (or contrast), and $\phi(x, y)$ is the fringe phase of interest (e.g. representing deformation or

Feature	Fringe Fitting	Phase Shifting		Fourier	
		Temporal	Spatial	Carrier	No Carrier
N°. Frames Required	1	≥3	1	1	1
Dynamic Event Analysis	Yes	Partly	Yes	Yes	Yes
Immunity to Environmental Disturbances (e.g. vibration)	High	Low-Med	High	High	High
Speed of Processing	Low	High	High	Med	Low
Achievable Accuracy	Low-Med	High	Med	Med	Med
Automatic Sign Determination	No	Yes	Yes†	Yes	No
Detector Spatial Resolution Required	1×	1×	3×	2-3×	1×
Immunity to Random Errors	Low-Med	High	Med	Med-High	Med-High
Immunity to Fringe Harmonics	Med	Med-High	Med	High	High
Immunity to Spatial Variation in Detector Gains	Med	High	Med	High	High

†When a spatial carrier is used.

Table 2.2: Comparison of common phase demodulation methodologies.

relief). Since there are three unknowns, either a minimum of three measurements are required to determine the phase, or additional information about the interferogram must be known or assumed. A summary of the three most common phase demodulation methods is shown in Table 2.2. These methods are compared in more detail in the following subsections.

2.5.1 Fringe Fitting

When only a single fringe map is available, fringe tracking can be employed, which involves searching for the local minima and/or maxima of the fringes. This is the most rudimentary form of fringe analysis, having poor spatial resolution and being very

susceptible to noise, and is not suitable for anything other than the crudest of measurements. A better alternative is nonlinear regression, which can be used to fit a model (e.g. polynomial) to the fringes; see, for example, a 1D approach by Schemm.[52] This can offer up to an order-of-magnitude accuracy improvement over Fourier techniques (discussed below), particularly when the number of fringes is small, and it does not suffer from Fourier windowing effects. It is however more susceptible to noise than Fourier methods and has a computation time in the order of ten-times longer (e.g. 2D approach by Slepicka[53]). Nonlinear regression requires an iterative solution, and unlike linear regression, requires an initial estimate of the parameters.

2.5.2 Temporal Phase Shifting

Within the field of interferometry, the most common method of extracting quantitative phase data from interferograms is to use temporal phase-shifting.[54] This involves acquiring three or more interferograms, with a phase shift between each of them. A simple calculation then gives both sign and magnitude of the phase. A three-step formula for phase shifts of $2\pi/3$ is given by

$$\phi(x,y) = \arctan\left(\sqrt{3}\frac{I_2 - I_1}{2I_0 - I_1 - I_2}\right) \tag{2.17}$$

where $\phi(x, y)$ is the desired phase and I_0 to I_2 are the interferograms successively phase shifted by $2\pi/3$, where the (x, y) dependence of the I_n terms has been omitted for clarity.

Phase-shifting algorithms provide one of the fastest and most accurate phase calculation methods, capable of less than $\lambda/1000$ rms error in the retrieved phase[55] (on optically-smooth surfaces), and they can be tailored to cope with various harmonics and phase-shift errors in the fringes.[56] However, dynamic events often occur too quickly for temporal phase-shifting to be used. Also, the resulting phase is very noisy when using speckled fringes, unless careful filtering is performed first.[57,58]

A recent approach using phase shifting for studying dynamic processes with ESPI is provided by a multi-camera optical configuration which enables simultaneous

recording of three phase-stepped fringe patterns.[59] This system is analogous to temporal phase-shifting, except that it produces the phase-shifted images—one from each camera—separated in space rather than time. This offers the advantage of being practically insensitive to time-dependent external perturbations. However, due to the use of three CCD cameras, the optical setup is more complicated and a special calibration procedure must be used to tune the modulation intensity of one of the cameras to the other two. As a result, the system accuracy is reduced relative to that of a single-camera system.

2.5.3 Spatial Phase Shifting

Phase-shifting algorithms are usually applied in the temporal domain, but can be used in the spatial domain if the phase can be constrained to vary spatially by a known amount.[60] For example, if carrier fringes (see below) are introduced with a frequency of 0.33 pixel^{-1}, then the phase difference from pixel-to-pixel will be approximately $2\pi/3$, and the standard three-sample (120°) phase-shifting algorithm[54] can be used, e.g. Eq. (2.17). This is known as spatial-carrier phase shifting (SCPS). It is sometimes attributed to Shough[61] (1990) or Kujawinska[62] (1991), but in fact appears much earlier under the title of *Sinusoid Fitting*. For example, Mertz[63] (1983), Macy[64] (1983), and Ransom[65] (1986). Mertz demonstrated a real-time system using digital electronics hardware and a three-sample phase-shifting algorithm. However, with SCPS the carrier fringes cannot always be constrained to the correct frequency, and (unlike temporal phase-shifting) the method is sensitive to spatial variations in detector element sensitivities.

2.5.4 Carrier Fringes

Another approach for the calculation of deformation phase from fringe patterns is through the introduction of carrier fringes between the two primary interferograms. The carrier is formed by incorporating a phase term that is a linear function of one or more of the coordinates, e.g. $\Delta\alpha(x, y)$ in Eq. (2.1). This can be effected, for example, by tilting one of the beams[†]. Like phase shifting, carrier fringes is a bipolar phase

[†] This is acceptable for ESPI, although not recommended for high-precision interferometry; a tilt will induce retrace errors in the interferogram.

demodulation technique, allowing the sign or polarity of the phase to be determined, as well as permitting straightforward extraction of the phase magnitude by means of various techniques, including several that require only a single fringe map. Carrier fringes slightly reduce the magnitude of deformation that can be measured,[66] but this is usually not a significant problem. Techniques for producing carrier fringes are presented in Chapter 3.

Spatial Synchronous Detection

For calculating a phase distribution from carrier fringes, a computationally-efficient method known as spatial synchronous detection (SSD)[67] can be used. This method (sometimes referred to as quadrature multiplicative moiré—QMM) is based on the multiplication of a fringe pattern by two carrier fringe patterns in phase quadrature, and then the two images are low-pass filtered to isolate the moiré pattern representing deformation. Ichioko[68] implemented a system using analog electronics hardware for real-time analysis.

Fourier Transform Method

Another technique for phase extraction from carrier fringes and one that lends itself to automation is the Fourier Transform Method (FTM). The FTM is the frequency-domain equivalent of the SSD (which is performed in the spatial domain). Roddier[69] proposed the FTM for 2D phase extraction from astronomical interferograms circa 1979.‡ Shortly after, Takeda[70] suggested a similar method for 1D reduction of interferograms.

The introduction of a carrier is a form of heterodyning, which in the Fourier domain separates the positive- and negative-frequency components of the interferogram from each other. By filtering to retain only the positive-frequency components of interest, the phase can be retrieved. This filtering process also removes most of the speckle noise (which is broadband) from the phase. The FTM is capable of accuracies of

‡ The FTM's genesis (in a qualitative form) lies in phase imaging by means of optical Fourier filtering, such as the Schlieren knife-edge test, which dates back to Foucault in 1859.

$\lambda/100$ rms, or better, on optically-smooth surfaces.[71] The mathematical details of the FTM are presented in Chapter 3.

A quasi-2D technique by Macy,[64] used 1D slices over a 2D data set. A comprehensive 2D approach was presented by Bone,[72] including consideration of sampling and windowing effects, as well as data extension (sometimes termed extrapolation or edge promotion). Further examinations of the technique include Roddier[69] (automated extrapolation via Gerchberg's iterative algorithm for analytic continuation[73-75]), Kujawinska[71,76] (windowing, extrapolation, and accuracy), Davila[66] (separability of frequency components), and Kaufmann[77] (comparison of FTM and phase-shifting methods).

Little consideration has been given to automated masking of spatial frequency terms, although its significance has been noted.[78] This is important if the FTM is to approach the speed, accuracy and repeatability of phase shifting, which calculates phase without user-intervention. In one approach,[79] a thresholded Gaussian filter was used to isolate components, but little detail was given.

Carrier fringes also allow simultaneous measurement of more than one dimension of deformation (see section 4.1.1 for theory). A configuration for concurrently measuring IP and OOP deformations using two reference and two object beams that form spatial carriers was demonstrated by Pedrini.[80] This used a short (180 mm) coherence length He-Ne laser. A delay line between the two halves of the system allowed the two primary interferograms to be recorded as an incoherent superposition, eliminating cross-interference terms which would corrupt the phase maps. As with spatial phase shifting,[51,60] spatial carriers demand stringent alignment of the beams.

Takatsuji *et al.*[81] presented another method of simultaneously measuring multiple components of deformation, by using multiple object beams and controlling their polarisation vectors to prevent co-interferences. Carrier fringes were generated by tilting the object beams. Three orthogonal components of deformation were measured concurrently with a single camera, and later separated using the FTM. This was an extension of a previous method by Moore and Tyrer[82] that simultaneously measured

two components of deformation (without carriers) and used two cameras (requiring careful alignment). The single-camera method produced good results, but did have the disadvantage that the carriers were manually adjusted (precluding dynamic measurements). Both methods have a requirement that the object surface reasonably preserve the polarisation state of the beams upon reflection (i.e. should be conductive). This is at odds with the situation where an object surface is dielectric, or is sprayed with white paint to provide a diffuse and highly-reflecting surface as a means of improving fringe quality.

2.5.5 Other Techniques

A phase distribution can be calculated from raw (non-carrier) fringes by the Kreis method of Fourier filtering, with bandpass masks in the spatial frequency half-planes.[83] Unfortunately, owing to the use of such masks, a phase inversion takes place for non-monotonic wrapped phase distributions (i.e., those calculated from closed fringes). Even though this ambiguity can be solved interactively by the operator, the procedure cannot be automated.

For closed fringes, a preferred approach is to use the analytical 2D Hilbert transform, or "vortex transform," method of Larkin.[84] This is also Fourier-based, but incorporates a spiral-phase filter function in the frequency domain, derived from local fringe direction. This method avoids phase inversions and does not require user-intervention.

However, both of these techniques (along with other closed-fringe methods) have the drawback that they cannot intrinsically determine the polarity of the underlying phase distribution, leaving an ambiguity between convex and concave deformation (or relief).

2.6 SUMMARY

This chapter has shown how deformation or relief can produce a phase change in scattered light, and this phase change then measured in an analytical manner. It is evident for many practical measurements that environmental limitations restrict the interferometer to the capture of only a single fringe pattern. For example, when

vibration or air-currents are present, if the acquisition time can be made short then the environmental disturbances will be effectively 'frozen'. Fast captures also confer an advantage when measuring transient deformations—a situation where short time intervals permit the acquisition of only one interferogram. Circumstances such as these rule out the multiple frames of phase-shifting algorithms. If the sign of the phase is required, in addition to its magnitude, then another bipolar phase modulation/demodulation method is essential. Thus the combination of carrier fringes and the FTM is a preferred option from the point-of-view of signed, quantitative phase. The acquisition of dynamic events often requires the use of addition fringes. Although these have poor contrast, suitable algorithms can increase the contrast to functional levels. In the next chapter, methods are examined for producing, enhancing and analysing carrier fringes.

3 Carrier Fringes

The discussion in Chapter 2 demonstrated the need for carrier fringes if the sign of the phase-change due to deformation is sought and only one fringe pattern is available. Several methods for modulating and demodulating carrier fringes are now examined in this chapter. Most techniques are based on two-beam interference. On one level, the theory for this is well established, but on another level there are subtleties and practicalities that need to be addressed. First the theory is presented, and then some practical configurations are presented and discussed.

3.1 CARRIER THEORY

As mentioned in Section 2.5.4, introducing a linear phase term, e.g. $\Delta\alpha(x, y)$ in Eq. (2.1), into one of the interferometer arms (object or reference beam) can form carrier fringes. Two methods of producing such a phase term are division of wavefront and division of amplitude. The former involves, for example, two parallel slits intersecting a beam to produce Young's fringes. The latter uses one or more beamsplitters to divide and re-combine the whole area of a beam, for example a Michelson interferometer. The division of amplitude approach is used in this thesis, for its convenience and flexibility.

If the beams have plane wavefronts, the fringes will be equispaced. The fringe spacing λ_s is determined[10] by the angle α between the two beams and is given by

$$\lambda_s = \frac{\lambda}{2\sin(\alpha/2)} \approx \frac{\lambda}{\alpha}, \text{ for } \alpha << 1 \tag{3.1}$$

Note that this equation is equivalent to Eq. (2.14). Thus for a fringe spacing of 0.3 mm (20 fringes over a 6 mm imaging sensor) and $\lambda = 0.633$ μm, then $\alpha = 2.2$ mrad = 0.12°.

Because this is a small angle, precise adjustment is required for the desired number of fringes.

3.1.1 Shift Theorem

Equation (3.1) is derived on geometrical grounds. However, a frequency-space consideration offers more utility in some circumstances. For situations where a source is moved laterally to produce carrier fringes, the Fourier shift theorem[85] neatly characterises the phase modulation that occurs. If a function is represented by $f(x)$, then the spatially shifted version is $I(x) = f(x - a)$, where a is the lateral shift in the x-direction. Fourier transforming this yields

$$\tilde{I}(u) = \mathcal{F}\{f(x-a)\} = \exp(-2\pi i u a)F(u) \tag{3.2}$$

where $\mathcal{F}$ is the Fourier operator, i is the imaginary operator and the Fourier transform is

$$\begin{aligned} F(u) = \mathcal{F}\{f(x)\} &= \int_{-\infty}^{\infty} f(x)\exp(-2\pi i u x)dx \\ &= \int_{-\infty}^{\infty} f(x)\cos(2\pi u x)dx - i\int_{-\infty}^{\infty} f(x)\sin(2\pi u x)dx \end{aligned} \tag{3.3}$$

in continuous form, where u is the spatial frequency in the frequency domain and the Euler relation has been used. Note that if $f(x)$ is an even function, i.e. $f(x) = f(-x)$, then the sine integral equals zero. Therefore, a shifted function will produce, in the far field (or near field using a lens), no change in amplitude but a linear spatial phase delay proportional to u. This phase delay is effectively a ramp of slope $2\pi a/u$, and when combined with a similar function having a different slope, carrier fringes are formed.

A special case of this is when two point sources, represented by delta functions $\delta(x \pm a)$, are in close proximity. Now in the far field:

$$\begin{aligned} \tilde{I}(u) &= \mathcal{F}\{\delta(x-a) + \delta(x+a)\} = \exp(-2\pi i u a) + \exp(2\pi i u a) \\ &= 2\cos 2\pi u a \end{aligned} \tag{3.4}$$

noting that $\mathcal{F}\{\delta(x)\} = 1$, a plane wave. Therefore, this produces cosinusoidal carrier fringes perpendicular to the x-axis.

3.2 CARRIER MODULATION

The simplest method of producing carriers is to induce a tilt in the object or reference beam by manual adjustment (e.g. tilting a mirror or tilting the object). However, this does not offer good repeatability (especially with small angles), nor does it allow operation at high speeds for capturing vibrations or transients. Therefore, it is desirable to use some form of electrically-operated modulator to meet these aims. There are two main types of such modulators: electro-mechanical, which physically move a mirror or lens; and electro-optical, which alter the optical properties of a component. Several examples of each type are now examined.

3.2.1 Piezoelectric Transducer

Piezoelectric transducers (PT) such as PZT (lead zirconate titanate) offer a practical means of achieving the small, repeatable movements required for producing carrier fringes. The simplest configuration is a hinged mirror, one edge of which is attached to a PT allowing the mirror to be tilted, as in Fig. 3.1 (left). The carrier fringes are then governed by Eq. (3.1). Another approach is to use a PT to translate a beam-expanding lens in a direction perpendicular to its optical axis.[86] A preferable approach is to translate a collimating lens as shown in Fig. 3.1 (right), which avoids nonlinearities in the carrier fringes that can occur when using divergent illumination. In this instance, the system can be described by the shift theorem of Eq. (3.2).

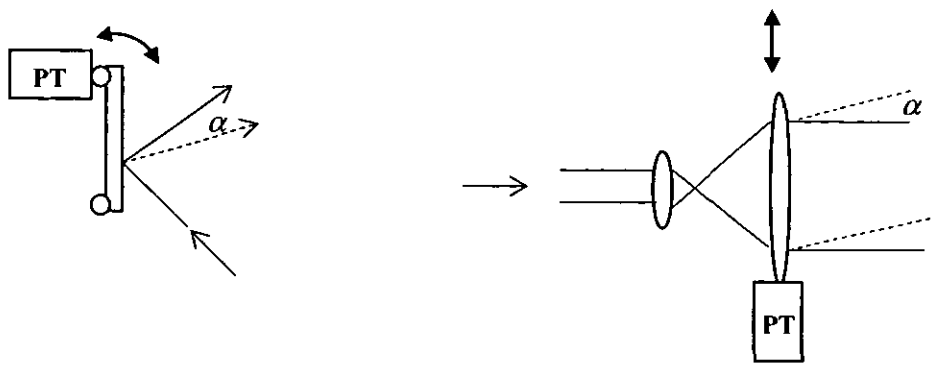

Fig. 3.1: Piezoelectric transducer (PT) carrier schemes: mirror tilting (left); lens translating (right).

PT's can operate at speeds of up to a few tens-of-kilohertz, making them suitable for static measurements, or dynamic measurements at low to medium frequencies.

However, PT's suffer from nonlinearities and hysteresis, placing extra demands on their usage.

3.2.2 Galvanometer

A mirror galvanometer (GM) consists of a galvanometric-driven shaft to which a small mirror is attached (see Fig. 3.2). It rotates through a small angle α ($< 5°$) that depends on the voltage applied to it. A rotation of α produces a tilt of 2α in the reflected beam,[†] independent of the angle of incidence ϕ, with the number of carrier fringes proportional to α, as in Eq. (3.1). The frequency response of GM's is usually limited to the low-kilohertz region,[87] restricting their use to static measurements or slow transients.[88] Since front-surface mirrors can be made with very good optical quality, the reflected beam will not be degraded as much as it will by electro-optical modulators, which use refractive or diffractive means.

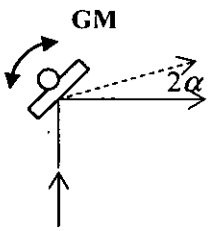

Fig. 3.2: Mirror galvanometer (GM), deflecting incident beam through small angle.

3.2.3 Rotating Mirror

An extension of the mirror galvanometer idea is to employ a continuously-rotating mirror[88] (RM). When combined with a pulsed laser, the narrow laser pulses effectively freeze the motion of the mirror. Unlike PT's or GM's that are driven synchronously, the RM rotates asynchronously. In this case the RM must be the master timing source from which a synchronisation signal is derived, e.g. by means of a continuous-wave source and a photodetector, as shown in Fig. 3.3. In this case the rotating mirror triggers the pulsed lasers continuously. When an acquisition is initiated, a single impulse is delivered to the object, and a single camera acquisition is performed.

[†] The mirror normal rotates by α, plus the reflected beam rotates α from the normal, thus giving 2α.

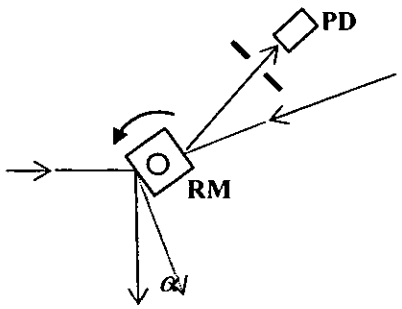

Fig. 3.3: Continuously-rotating faceted mirror (RM) for deflecting incident beam at high speed, shown with synchronisation system of auxiliary beam, aperture and photodetector (PD).

As an example, if an angle of 5 mrad is required and the laser pulse separation is 2.5 ms, then the angular velocity required is 1 rad/s, or a speed of 9.5 rev/min. If the pulse separation is only 10 μs, then the angular speed must be 2390 rev/min., which is readily achievable with small motors. Even for this case, the pulse-separation to pulse-width ratio is still high at 1000:1 (assuming 10 ns laser pulses), causing insignificant movement of the beam during image capture.

3.2.4 Dual-Pulsed Laser

Most pulsed lasers emit very short temporal pulses, of the order of a few nanoseconds or less. However their repetition rate is often much less, usually of the order of a few tens-of-hertz. If the repetition rate were higher, it would be possible to use two successive pulses to capture vibrations. The region of most interest for vibrations is 100 Hz to 10 kHz. One way of achieving this is to use a twin pulsed-laser,[48] such as the Spectron SL800 shown in Fig. 3.4. This laser consists of two separate Q-switched Nd:YAG cavities, commonly seeded by a laser diode to obtain mutual coherence. The two beams are then optionally amplified and made collinear, before passing through a frequency-doubling crystal to produce a beam at 532 nm. If a tilt is introduced between the two laser pulses, for example using a GM or RM, then carrier fringes can be formed.

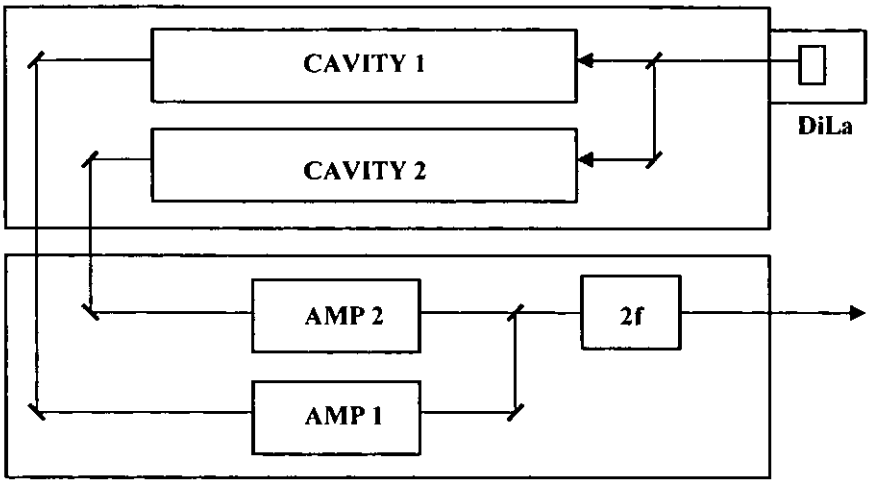

Fig. 3.4: Spectron SL800 dual pulsed laser; DiLa: diode laser seeder, CAVITY: rod, flashlamp, Q-switch; AMP: amplifier; 2f: frequency doubler.

The cavities can run at a rate of up to 50 Hz, producing a beam that is continuous to the eye and a TV camera, which is convenient for aligning the system. This is too slow for capturing vibration phenomena, but since the cavities can be triggered independently of each other, the time separation between two pulses can be quite small, limited only by the resolution of the pulse generators and the stability of the laser. Triggering can be initiated by an external source, thus allowing the laser pulses to be synchronised to either the object's movement or the camera's frame synchronisation signal.

3.2.5 Pockels Cell

A Pockels cell consists of a crystal whose birefringence can be altered with an applied electric field. This rotates the plane of polarisation of the incident beam, and after passing through an analyser, contrast ratios of 1000:1 can be readily achieved. Switching speeds can also be very fast—1 GHz or higher. The high voltages required (~5 kV) impose limitations, as well as affecting the stability due to heating effects. The use of Pockels cells for producing carriers by means of a Michelson interferometer has been covered by others, in both static[66] and dynamic[89] systems, and will not be discussed further here.

3.2.6 Liquid Crystal Device

A liquid crystal device (LCD), or cell, can be used to rotate the polarisation of an incident beam, producing an effect similar to a Pockels cell. However, LCD's operate

in a different manner. A LCD comprises a thin layer (~10 μm) of liquid, sandwiched between two parallel plates of glass that are coated with transparent electrodes. The liquid is composed of birefringent molecules (hence crystal-like) having dielectric anisotropy. With the application of an electric field the molecules realign and the change in birefringence influences the phase of the incident beam.[90] LCD's only require a low voltage (~10 V), and although they are not as fast (low-kilohertz switching speeds) as Pockels cells, they are adequate for some ESPI systems.

Most often, LCD's are employed in twisted-nematic polarisation-rotation mode. Here the 'director' (major axis) of the molecules undergoes a helical rotation about the optical axis of, typically, 90° between one electrode and the other. This rotates the plane of polarisation of the incident linearly-polarised beam by the same amount.† Now, when an electric field is applied the molecules 'stand-up', that is, begin to align themselves along the optical axis, parallel to the electric field. In this orientation, the birefringence is such that the incident polarisation is not rotated. With an analyser on the output beam, the LCD forms an intensity modulator. This is the mode used for LC televisions, computer screens, etc., when combined with patterned electrodes that form individual pixels.

However, LCD's can also be designed for isotropic phase modulation, with no rotatory effects. By aligning the LC molecules to have the same orientation at both electrodes, and with suitable LC material, the molecules will preserve the plane of polarisation throughout the thickness of the cell. If an electric field is applied between the electrodes, the molecules will again 'stand-up', changing the refractive index and hence the phase delay. The phase change $\Delta\phi$ is a function[91] of the refractive index change Δn, the cell thickness d and the wavelength:

$$\Delta\phi = \frac{2\pi d\Delta n}{\lambda} \tag{3.5}$$

† The molecular rotation is influenced by the surface preparation of the electrodes and the doping of the LC material. The polarisation rotation is due to a combination of waveguiding and birefringence.

Now, in a novel approach, if the cell is made with the glass plates wedged rather than parallel, the phase change will vary across the width of the cell (assuming $n_{cell} > n_{air}$). The optical path length (OPL) through the cell is then a linear function of the distance x from the edge of the cell, say $OPL(x) = ax + c$ (where a and c are constants), the cell thus creating a linear phase modulation in the x direction. Increasing the voltage will increase Δn, consequently varying the tilt of the beam. This, of course, is the prerequisite for carrier fringes. Such a device is shown in Fig. 3.5.

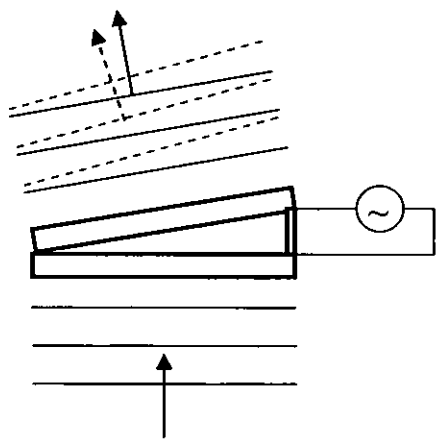

Fig. 3.5: Liquid crystal cell linear phase modulator. Plane wavefront incident from below passes through cell and is tilted due to wedged cell. Application of a voltage across the cell changes the optical path length, altering the linear phase delay and changing the tilt of the exit beam.

The response time[92] τ of molecular realignment within a LC cell is proportional to the rotational viscosity γ_r of the material and the cell thickness d squared:

$$\tau = \frac{\gamma_r d^2}{K\pi^2} \tag{3.6}$$

where K is the elastic constant of the material. The high sensitivity to d demonstrates the importance of keeping the thickness small to ensure fast response times. Note that for a wedged cell the response time will be quadratic across the width of the cell. Furthermore, the rise time has an inverse-square relationship with the drive voltage.[93] Therefore a faster response can also be effected by using a higher voltage (this will not improve the fall time, but in a system for measuring transients only the rise time is important).

3.2.7 Acousto-Optic Modulator

Acousto-optic modulators (AOM's) offer a means of switching and deflecting beams very quickly and repeatably. AOM's comprise a photo-acoustic medium, in which an acoustic wave is induced by means of a PT attached to one end of the medium, while the other end contains an absorber to minimise reflections (see Fig. 3.6). The acoustic wave modulates the refractive index of the medium through the elasto-optic effect, effectively creating a phase grating. The drive frequency (RF, typically in the range 40 – 1000 MHz) determines the period of the grating, while the drive amplitude (usually a few watts power) determines the depth of phase modulation and hence the diffraction efficiency.

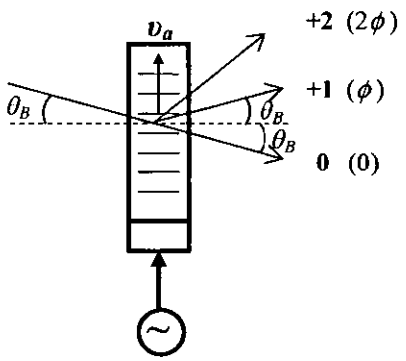

Fig. 3.6: Acousto-optic modulator showing 0, +1 and +2 diffraction orders, with corresponding phase modulation rates (see text). Beam angles have been exaggerated for clarity.

With no drive signal, a laser beam will pass through the modulator undiffracted with approximately 95% transmission. This is termed the zero-order beam, $I(0)$. With a drive signal, the beam will be diffracted, producing a first-order beam with typically 85% diffraction efficiency, $I(1)$. When used as a switch, the $I(0)$ beam will give a contrast ratio in the order of 10:1, based on the diffraction efficiency. However, by using the $I(1)$ beam contrast ratios of more than 1000:1 are readily achievable, determined mainly by scatter.

The switching time is a function of the transit time of the acoustic wave across the laser beam and is given by[94]

$$t_o = \frac{0.65w}{v_a} \tag{3.7}$$

where w is the $1/e^2$ width of the laser beam, v_a is the acoustic velocity and t_o is the optical rise time. For typical values of $v_a = 4000$ m/s and $w = 1$ mm, then $t_o = 160$ ns. Shorter times are possible by focussing the laser to a smaller diameter (with the qualification, from diffraction theory, that beam divergence will increase thus decreasing the resolution in scanning-spot systems—something that is not particularly important in the current application). It should be noted that as the switching time t_s approaches t_o the contrast ratio falls off, dropping to less than 10:1 for $t_s/t_o = 1$.[95]

The angle of the input beam should optimally be the Bragg angle θ_B (measured from the device normal), and is given by[96]

$$\sin\theta_B = \frac{\lambda}{2\Lambda} \tag{3.8}$$

where the acoustic wavelength is

$$\Lambda = \frac{v_a}{f} \tag{3.9}$$

and f is the drive frequency. For $v_a = 4000$ m/s, $f = 40$ MHz and $\lambda = 500$ nm, then $\Lambda = 0.1$ mm and $\theta_B = 2.5$ mrad. The m^{th}-order beam then makes an angle θ_m with respect to the zero-order beam, where

$$\theta_m = 2m\theta_B \approx \frac{m\lambda}{\Lambda} = \frac{m\lambda f}{v_a} \tag{3.10}$$

When the Bragg condition is met, the first-order beam will dominate. Higher-order beams will exist, but will generally have negligible intensity. This is the case for Bragg-type modulators, which subject the optical beam to multiple diffraction.[96]

An example of an AOM system for producing carrier fringes is shown in Fig. 3.7. An AOM is placed in each arm of a Mach-Zehnder interferometer,† such that the zero-order beams are passed and then recombined to form the reference beam of an ESPI system (alternatively, the first-order beams could be used for higher contrast). One of the mirrors is then tilted to give carrier fringes. With both modulators on, the first-order beams are blocked and no output beam is present. The two modulators are then momentarily pulsed off in sequence, one before deformation and the other after deformation. This results in a high-speed carrier-modulated reference beam that can be synchronised to the object deformation and laser pulses.

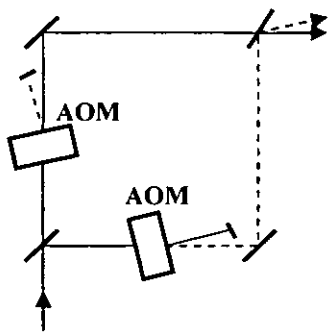

Fig. 3.7: Acousto-optic modulators in a Mach-Zehnder arrangement for fast generation of carrier fringes.

3.2.8 Acousto-Optic Deflector

A variation of the AOM is an acousto-optic deflector (AOD), as illustrated in Fig. 3.8. This works on the same basic principle, but is designed to operate over a much wider bandwidth (e.g. 25 MHz, cf. 7 MHz for AOM). Because the beam deflection angle is proportional to the drive frequency, the beam can be steered or tilted by varying the frequency (e.g. $\Delta\theta = 3.9$ mrad for 25 MHz bandwidth).

† A Michelson, or other type of interferometer, could be used instead as long as there are two separate optical paths in which to position the two AOM's. A Mach-Zehnder configuration has the advantage that the beams make only a single-pass through the AOM's, offering better beam quality than the double-pass of, say, a Michelson.

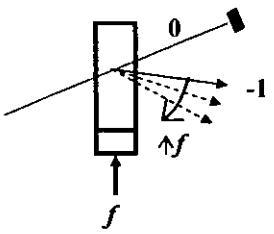

Fig. 3.8: Single AOD showing variation of the negative first-order beam angle with change in drive frequency.

One limitation of using an AOD (or AOM) in an interferometric system is that the acoustic wave is not stationary but travelling with velocity v_a, thus producing a time-dependent phase modulation of the diffracted beam(s). This modulation can be conveniently modelled by invoking the Fourier shift theorem of Eq. (3.2). If $I(x) = g(x - v_a t)$ describes the phase grating propagating in the x direction within the modulator, where t is time, then the diffraction pattern is given by

$$\tilde{I}(u) = \mathcal{F}\{g(x - v_a t)\} = \exp(-2\pi i u v_a t) G(u) \tag{3.11}$$

Where $G(u)$ is the Fourier transform of $g(x)$. Equation (3.11) shows that there is no amplitude modulation, but a temporal phase modulation that is synchronous with the order u of the diffracted beam. Thus if the rate of phase change is $d\phi/dt$ for the first-order beam, then it will be $m\, d\phi/dt$ for the m^{th}-order beam (see Fig. 3.6). Note that there is no phase modulation of the zero-order beam ($u = 0$).†

In terms of frequency, the phase ramping is a Doppler shift in the frequency of the diffracted beams, by an amount $\pm mf$. An upshift (+1) or downshift (−1) occurs depending on whether the incident beam is facing to or away from the wavefront, respectively. The +1 order is diffracted away from the wavefront (Fig. 3.6) and the −1 order toward the wavefront (Fig. 3.8). Since f is typically seven orders-of-magnitude less than the optical frequency, the effect is negligible in most cases, although has been exploited for heterodyne interferometry.[97,98]

† Somewhat counter-intuitive, in that it still 'sees' the moving grating.

It should be noted that when varying the drive frequency of an AOD the acoustic wavelength will vary, forcing a departure from the Bragg condition. This will reduce the intensity of the first-order beam and increase that of other beams.[99,100]

The aforementioned phase modulation characteristics present problems when using the diffracted beam(s) in coherent interferometric applications, for example using the first-order beam to tilt a wavefront in an interferometer. The resulting fringes, modulated at tens of megahertz, will be 'washed out' to both the eye and a CCD camera. Several methods for overcoming these limitations are now examined.

If the incident beam is pulsed with sufficiently short temporal width, then the phase grating can be effectively 'frozen' in time. A moiré fringe projection system using this idea has been implemented by Blatt et al.[40] They used an 80 MHz AOM, amplitude modulated with 50 ns pulses, to strobe the beam before passing through an AOD. Short pulse widths such as this are necessary to freeze the grating, but they also reduce the intensity of the AOM beam.

A means of circumventing this constraint, and simplifying the optical path in the process, is to use a pulsed laser (gas or diode) in place of the AOM. Most pulsed lasers have temporal widths of 10 ns or less, making them ideal for this application.

A system of this nature was demonstrated by Mermelstein *et al.*,[101] using synthesised, multi-frequency signals to modulate both the AOM and a diode laser. Pulsed or modulated systems such as these allow rapid modulation of the carrier frequency, and hence can be used with temporal phase unwrapping[32] (section 3.3.4) to measure large deformations or discontinuous profiles, at video rates. One disadvantage is that the optical power efficiency is generally less than 50%.

A novel idea for inhibiting the phase modulation is to use two AODs in series.[30] Working from the premise that if a pair of AODs are oriented such that their velocity vectors are parallel but in opposite directions, then there exist two counterpropagating gratings of the same frequency. Modelling this using phasor notation, then if one

grating is described by $A_1\exp(i\upsilon_a t)$, the other will be $A_2\exp(-i\upsilon_a t)$. The transmission through the two gratings will then be $A_1A_2\exp[i(\upsilon_a t - \upsilon_a t)] = A^2$ (assuming $A_1 = A_2$), thus cancelling the phase modulation.

However, a simple model such as this does not convey the full conditions regarding diffraction, velocities, orientations, and drive frequency. Perusal of the literature reveals a number of models[102] for acousto-optic interaction, although these mostly examine intensity rather than phase.[99,103] Indeed most AO devices are used as intensity modulators, beam deflectors or optical switches.[96] As it transpires, the Doppler frequency shift provides the utility required. This is now examined in more detail.

The optical transmittance of the modulator can be described by the space-time function

$$t(x,t) = \exp[ig(x - \upsilon_a t)]\mathrm{rect}(x/L) \tag{3.12}$$

where L is the width of the modulator aperture. Using an amplitude $a(x)$ and phase $\varphi(x)$ modulated cosinusoidal signal, the function $g(x)$ will be

$$g(x) = a(x)\cos[2\pi x f_x + \varphi(x)] \tag{3.13}$$

where $f_x = 1/\Lambda$ is the spatial frequency of the acoustic wave. Therefore:

$$g(x - \upsilon_a t) = a(x - \upsilon_a t)\cos[2\pi(x - \upsilon_a t)f_x + \varphi(x - \upsilon_a t)] \tag{3.14}$$

Now, substituting this into Eq. (3.12) yields

$$t(x,t) \cong 1 + ia(x - \upsilon_a t)\cos[2\pi(x - \upsilon_a t)f_x + \varphi(x - \upsilon_a t)] \tag{3.15}$$

where the approximation[104] $\exp(i\psi) = 1 + i\psi$, for $\psi << 1$ is used and the aperture is ignored (since this is a second-order spatial effect, while the interest here is with temporal effects).

Assuming that the drive signal has no amplitude or phase modulation, $a(x) = 1$ and $\varphi(x) = 0$, and using the exponential form of the cosine:

$$t(x,t) = 1 + \tfrac{1}{2}i\{\exp[i2\pi(x - v_a t)f_x] + \exp[-i2\pi(x - v_a t)f_x]\} \tag{3.16}$$

A planar optical wave used as a source can be described by the fundamental wave equation $E(z,t) = \exp i(k_z z - \omega t)$, where $k_z = 2\pi/\lambda$ is the propagation constant in the z direction, $\omega = 2\pi\nu$ is the angular frequency and ν is the optical frequency. If such a plane wave is incident on the modulator, it emerges with an amplitude of

$$\begin{aligned} u(x,t) &= t(x,t)E(z,t) \\ &= \exp[i(k_z z - \omega t)] \\ &\quad + \tfrac{1}{2}i\exp[i(\omega_x x + k_z z)]\exp[-i(\omega + \omega_x v_a)t] \\ &\quad + \tfrac{1}{2}i\exp[i(-\omega_x x + k_z z)]\exp[-i(\omega - \omega_x v_a)t] \end{aligned} \tag{3.17}$$

where $\omega_x = 2\pi f_x = 2\pi/\Lambda$ is the spatial angular frequency. Diffraction orders higher than the first have been ignored. The three terms in Eq. (3.17) represent the zero, +1 and −1 beams, respectively. Now, from the second term, the angle of the first-order beam is given by

$$\theta = \arctan(\omega_x / k_z) = \arctan(\lambda/\Lambda) \tag{3.18}$$

which is equivalent to Eq. (3.10) for small angles, and the frequency of the +1 order beam is given by

$$f_{+1} = (\omega + \omega_x v_a)/2\pi = \nu + f \tag{3.19}$$

where it is noted from Eq. (3.9) that $f = v_a/\Lambda = v_a f_x$. This equation represents the optical input frequency Doppler-upshifted by the drive frequency. From Eq. (3.17), this manifests as a temporal phase modulation at the new frequency.

Thus, if the first-order beam is interfered with a zero-order (unmodulated) beam, the phase difference between the two beams is not constant, but modulated at the difference frequency f, effectively a beat frequency. Because of the phase modulation,

any fringes formed from the two beams will be phase modulated at frequency f, and hence not temporally resolvable by most area detectors. Noting that the +1 and −1 order beams have opposite frequency shifts, then a mutual interference of these two beams should cancel the frequency modulation and produce stable fringes. The two beams could be produced from a pair of devices in parallel (similar to Fig. 3.7), or by one device detuned from the Bragg angle to produce simultaneous +1 and −1 beams.

A scheme such as Fig. 3.9 with a pair of devices in series can also be envisioned, where the −1 order beam from the second AOD tilts with a change in drive frequency, thus allowing the generation of spatial carrier fringes. Taking care with ±diffraction orders, the frequency shift will cancel, as shown in Fig. 3.9.

In such a configuration, the output beam (+1, −1) can be used as the reference beam and the input beam (0) as the object beam. The two beams can be interfered because their relative phase is stationary (assuming both devices are driven with the same frequency). The output beam will tilt when the drive frequency f is varied, allowing carrier fringes to be introduced in real time. The output beam forms an angle of $4\theta_B$ with respect to the input beam due to the cascading effect of the two AOD's (assuming that the acoustic velocities have equal magnitudes).

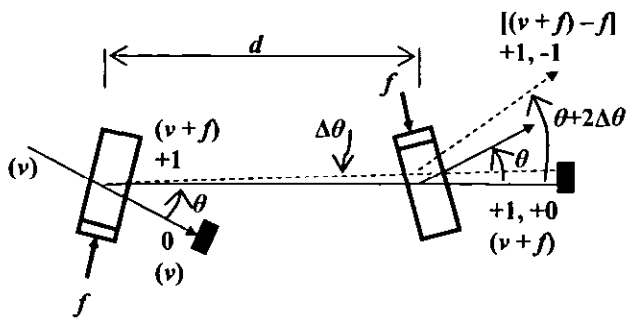

Fig. 3.9: Dual-AOD system for producing carrier fringes by varying the angle of the output (reference) beam while simultaneously cancelling its phase modulation. Illumination frequency: ν; Drive frequency: f (solid line), $f+\Delta f$ (dashed line).

The combined change in tilt angle $\Delta\theta_T$ due to a change in frequency Δf is then

$$\Delta\theta_T = 2\Delta\theta = \frac{2\lambda\Delta f}{v_a} \tag{3.20}$$

Now from Eq. (3.1), subsequent carrier fringes will have a spatial wavelength of

$$\lambda_s = \frac{\lambda}{2\lambda(f+\Delta f)/v_a - \theta_0} \tag{3.21}$$

where θ_0 is the offset or 'nulling' angle that sets the initial fringe spacing. These two equations show that the beam angle and carrier frequency are independent of the device separation and vary solely with the drive frequency† (assuming the wavelength and the acoustic velocities are constant), thus slight mismatches in device characteristics should not affect the stability of the fringes. For the special condition of $\theta_0 = 0$, Eq. (3.21) also reveals that the carrier frequency is independent of the illumination wavelength. Such achromaticity then opens up applications in white-light interferometry (Section 2.3). Note that for this condition, and using the previously specified device parameters, then the fringe spacing will be small: $\lambda_s = 50$ μm.

A system such as Fig. 3.9 is 'static', requiring no modulation of the input beam, thus higher optical efficiencies are theoretically possible, compared with the pulsed/modulated systems mentioned earlier in this section. Assuming 85% diffraction efficiency for first-order beams, then the (+1, −1) beam would be 72%.

Angular alignment is important, however: if the second AOD is tilted so that the output beam is (+1, +1) order, the interference phase will no longer be stationary due to a double-upshift in frequency, and the output beam will translate rather than tilt. The double Doppler-upshift, may however, find utility in applications such as laser Doppler velocimetry.

† Whether the carrier frequency varies directly or inversely with drive frequency depends on the relative directions of the object and reference beams (θ_0).

A system somewhat similar to Fig. 3.9 has been demonstrated more recently for fast, nonlinear scanning of a focussed point (an intensity application),[105] but not yet for interferometric applications.

An experiment is now devised to confirm the above phase-cancellation theory. With reference to Fig. 3.10, an incident monochromatic beam (λ = 514 nm) passes through an attenuator (A) before being split into two beams by a variable beamsplitter (VBS). The direct beam passes through two AOD's: Andersen Laboratories, model DLM40V7 (strictly, these are AOM's, but their bandwidth of 7 MHz allows them to mimic AOD's over a bandwidth sufficient for the experiment). The first AOD is aligned to produce a +1 order beam, which is then directed through the second, aligned to produce a −1 order beam. The resulting (+1, −1) beam is then combined with the zero-order, or reference (R), beam using a beamsplitter (BS). A lens magnifies the beams to make the fringes readily discernible to the eye and for a CCD camera. The VBS is adjusted to equalise the irradiances of the two beams, to optimise fringe visibility. Because the devices are operating in isotropic diffraction mode, they have no polarisation effect.[106]

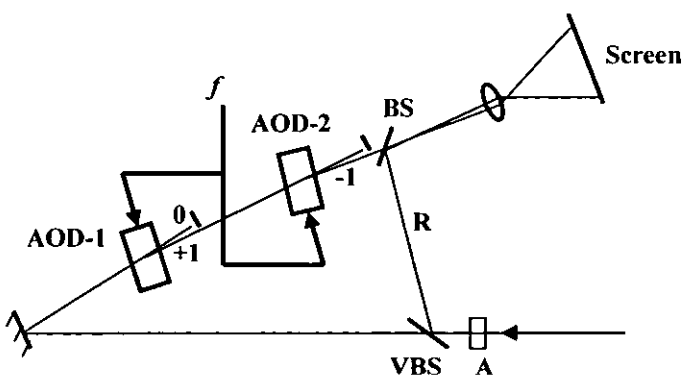

Fig. 3.10: Dual-AOD system for demonstrating electrically-tuneable carrier fringes by interfering zero-order beam with variable-angle diffracted beam. A: attenuator; VBS: variable beamsplitter; BS: beamsplitter; R: reference beam.

A photograph of the experimental system is shown in Fig. 3.11, where the laser beam path has been highlighted for clarity. The AOD's are driven with a sinusoid of

common frequency (40 MHz), with the drive in opposing directions. The left-foreground of the photo shows the frequency source, HP8116A Function Generator, driving the AOD's though an RF amplifier, Amplifier Research, model 25A100. The amplifier is rated at 25 W over a 10 kHz to 100 MHz bandwidth.

Fig. 3.11: Experimental system with dual AOD's; laser path highlighted.

To begin, the second AOD was removed and the +1 order beam from the first AOD was interfered with the R beam. As expected, no fringes were observed due to the high-speed temporal phase modulation of the +1 beam. The resulting image is shown in Fig. 3.12.

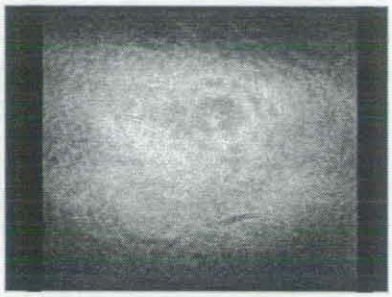

Fig. 3.12: Interference between +1 and 0 order beams—no fringes visible due to inherent high-speed temporal phase modulation.

Next, the second AOD was reinstated, and this time stationary fringes were observed, as shown in Fig. 3.13. This figure shows the carrier fringe frequency varying with the drive frequency. The first image (top left) is for 35 MHz drive frequency, where the beamsplitter was adjusted for approximately three fringes over the field of view. The frequency was then increased in 1 MHz steps (left-to-right, top-to-bottom), up to 40 MHz, where approximately nine fringes are observed. The fringes were very stable, with no noticeable drift. In practise, this is limited by the RF frequency stability of the source, and the stability of the acoustic velocity within the AOD's.

The theory predicts that the complementary (−1, +1) configuration should give the same result as a (+1, −1) one—an experiment confirmed that this was indeed the case. Conversely, an even-even (+1, +1) or odd-odd (−1, −1) configuration should not yield visible fringes due to the double-upshift in frequency; this was also confirmed by experiments.

The AOD separation was $d = 300$ mm; although the carrier frequency is not sensitive to this parameter, practically it should be minimised to keep the +1 beam within the aperture of the second AOD. Additionally, the AOD's should be placed as close as practicable to the object, to minimise beam walk-off from the object (preferably, the AOD beam should be used as the reference beam, in close proximity to the camera,

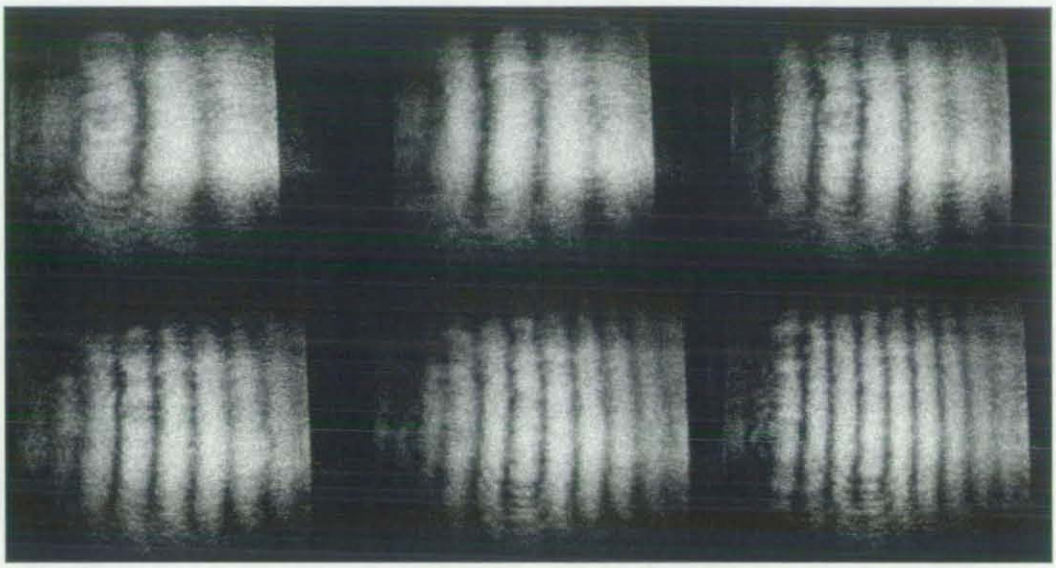

Fig. 3.13: Interference between (+1, −1) and 0 order beams, showing vertical carrier fringes varying with drive frequency; 35 to 40 MHz in 1 MHz steps (left-to-right, top-to-bottom).

thus having negligible walk-off). Note that as a proof-of-principle experiment, little attention was paid to optimising the fringe quality; spatial filtering of the beams may help to reduce coherent noise and also improve the fringe contrast.

A neat variation of the above strategy is to use a single AOD with the −1 (or +1) order used for both the object and reference beams, as shown in Fig. 3.14. Changing the drive frequency will tilt the beams, generating the carrier phase. Because all beams have the same order, they possess the same phase modulation and thus can be interfered.

One drawback is that both object and reference beams will tilt, cancelling the carrier phase. However, they can be made to tilt in different directions—a countertilt—effectively doubling the tilt. To achieve a countertilt, the reference beam must undergo an even number of reflections and the object beam an odd number of reflections (or vice versa), as illustrated in Fig. 3.14, for example. Here the angle of the arrowed lines shows the direction of beam tilt with increased drive frequency, while the arrowheads show the direction of phase modulation. It is apparent that this configuration also produces opposing phase modulation vectors, therefore cancelling the phase modulation in the process.

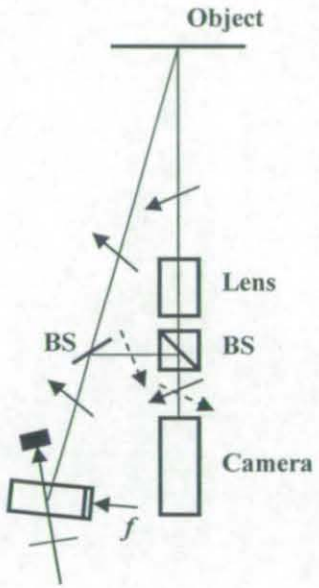

Fig. 3.14: Single-AOD system for producing variable carrier fringes by phase-cancelling countertilts in reference and object beams. The angle of the arrowed lines indicates direction of beam tilt with increased drive frequency, while the arrowheads show the direction of phase modulation.

One proviso is that the beam will translate slightly on the object *and* the camera. However, for a beam tilt of 5 mrad and object distance of 1 m, then the translation on the object will be only 5 mm. Apart from its simplicity, such a system is attractive because it controls both object and reference beams simultaneously—the AOD can thus double as a strobe for performing stroboscopic measurements of vibrating objects. The results of an experiment using the system of Fig. 3.14 are shown in Fig. 3.15, where the frequency was varied from 38 MHz to 41 MHz in steps of 1 MHz (from left-to-right). The system showed similar behaviour and stability to the dual-AOD system, but with simpler configuration and alignment.

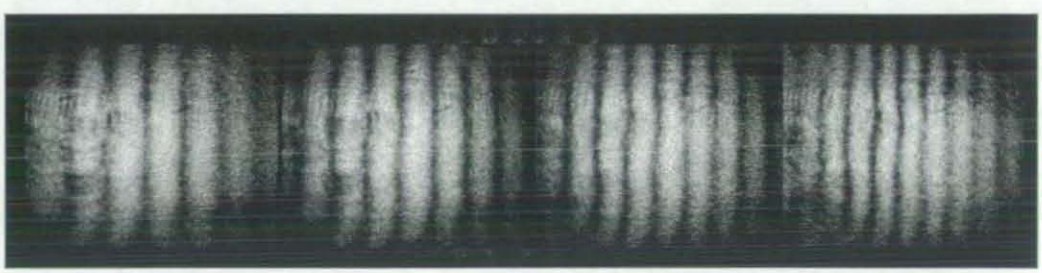

Fig. 3.15: Carrier fringes produced with a single AOD. Drive frequencies: 38, 39, 40, 41 MHz (left-to-right).

The question now arises: in a dual-AOD system, what happens if both devices are oriented such that their gratings are copropagating? Counter to the original hypothesis, the theory predicts that if the odd-even (or even-odd) relationship is maintained, the phase modulation will still cancel. This is possible given that Eq. (3.17) has no dependence on acoustic velocity, but only on the sign of the diffraction order.

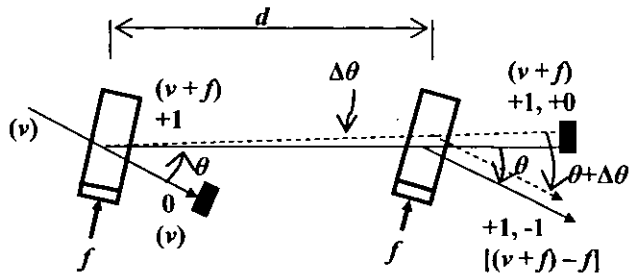

Fig. 3.16: Dual-AOD system for phase shifting by translating the beam, while simultaneously cancelling the Doppler phase modulation. Note orientation of the AOD's. Drive frequency: f (solid line), $f+\Delta f$ (dashed line).

Such a system is shown in Fig. 3.16, where it is noted that the output beam translates (but remains parallel) with a change in drive frequency. This induces a change in the optical path length (OPL), which of course, is the prerequisite for phase shifting. Because the beam does not tilt, there will be no change in spatial fringe frequency. The OPL difference due to a change in beam angle $\Delta\theta$ is then

$$\Delta\mathrm{OPL} = d\left(\frac{1}{\cos\theta} - \frac{1}{\cos(\theta+\Delta\theta)}\right) \tag{3.22}$$

In terms of the drive frequency, the resulting phase shift will be

$$\Delta\phi \approx \frac{2\pi d}{\lambda}\left(\frac{1}{\cos[\lambda f/v_a]} - \frac{1}{\cos[\lambda(f+\Delta f)/v_a]}\right) \tag{3.23}$$

Therefore the phase shift depends on the device separation and the drive frequency (assuming the acoustic velocity and optical wavelength are constant). To effect a phase shift of 2π with a drive frequency of 40 MHz, $\lambda = 0.514$ μm, $v_a = 4037$ m/s, and a device separation of $d = 0.30$ m, then $\Delta f = 2.74$ MHz is required. This also induces a

lateral translation to the beam of 104 μm. If the beam is, say, at least 1 mm wide, then this translation should be insignificant for most applications (i.e. there is still 90% overlap region for interference).

An experiment to confirm the phase-shifting property was conducted. The configuration is shown in Fig. 3.17, similar to the carrier frequency system of Fig. 3.10. Again, the AOD separation was 300 mm. Firstly, with the AOD's running at 39 MHz, the beamsplitter was adjusted to give approximately eight fringes across the field of view. Secondly, the frequency was changed to 40 MHz and then 41 MHz. The results are shown in Fig. 3.18, where the phase shift is approximately 120° between each image.

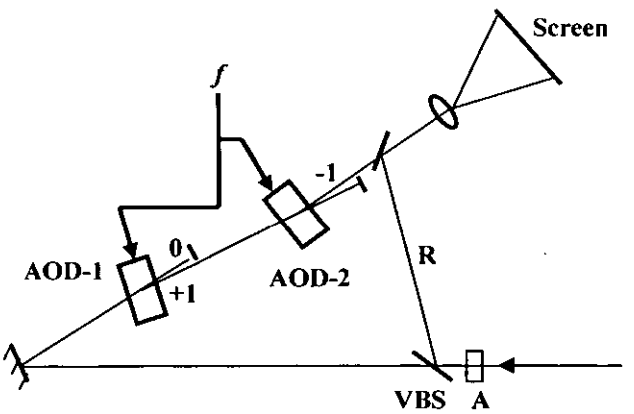

Fig. 3.17: Dual-AOD system for demonstrating electrically-tuneable phase shifting by interfering zero-order beam with variable-delay diffracted beam. A: attenuator; VBS: variable beamsplitter; R: reference beam.

Unlike the carrier-frequency system, the phase-shifting system is directly dependent on the device separation. Therefore, in harsh environments, the device separation should be minimised and then compensated for by a larger change in drive frequency. However, for the experiments reported herein with 300 mm separation on an optical bench, the stability was very good, with no perceptible drift in fringe position.

These experiments have proven that stable fringes are indeed possible using just one or two AOD's, and also that the carrier frequency or phase shift can readily be set by the AOD drive frequency. The results are not necessarily confined to bulk devices such as AOD's; they are equally applicable to surface-wave acoustic devices. Although the

phase-shifting method is not used for the carrier fringe method described in this thesis, it has applicability to a wide range of interferometry applications (see Section 2.5.2).

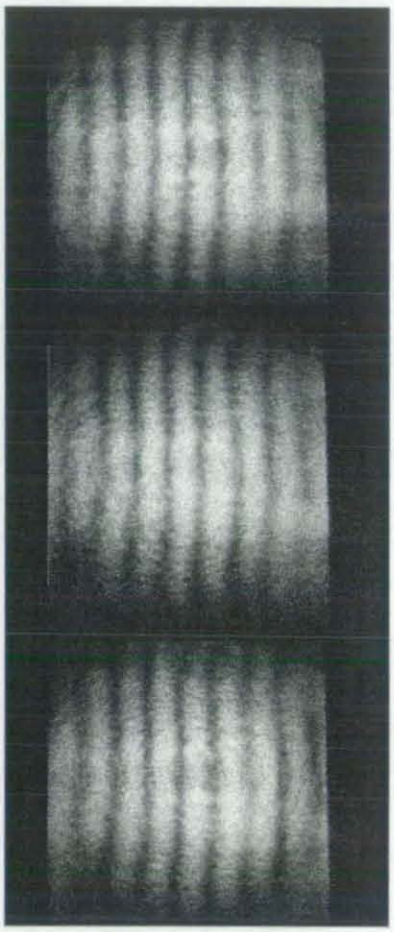

Fig. 3.18: Phase-shifting results for the dual-AOD system. Drive frequencies: 39, 40, 41 MHz (top-to-bottom).

Finally, some other points to note: Eq. (3.17) predicts that if the drive frequency to only one of the modulators is varied, a continuous phase shift will occur, at a rate proportional to the frequency difference. For a carrier-fringe system such as Fig. 3.10, this would allow phase shifting independent of the carrier frequency modulation (e.g. if f = 40 MHz and Δf = 10 Hz, beam tilt would be insignificant, but phase would be shifted at 10 Hz rate). Similarly, for a phase-shifting system such as Fig. 3.17, phase shifting could be achieved with minimal beam translation. An experiment of this nature was not feasible due to insufficient resolution in the frequency source. Furthermore, in either type of system, if the phase of one of the drive signals is changed (equivalent to translating one of the modulators in the x direction), there

should be a corresponding phase change in the interference fringes. In this manner, phase shifting can be accomplished completely independent of (or in addition to) beam tilting or translating.

3.3 CARRIER DEMODULATION

Having introduced carrier fringes into the interferograms to furnish the sign of the phase and facilitate the phase calculation, it is now necessary to decouple, or demodulate, the carrier phase from the object phase and then calculate the object phase. In the following sections, techniques for processing the interferograms are presented.

3.3.1 Fringe Visibility

When measuring transient deformations, addition fringes are often used, as described in Section 2.1.1. In this case an enhancement technique must be used before phase calculation to improve the low visibility of the addition fringes. The visibility is defined as $V = (\langle I \rangle_{max} - \langle I \rangle_{min}) / (\langle I \rangle_{max} + \langle I \rangle_{min})$, where $\langle I \rangle_{max}$ and $\langle I \rangle_{min}$ are the average maximum and minimum irradiance of the interference fringes.

The $(I_o + I_r)$ term in Eq. (2.2) represents a background-intensity level that reduces the fringe visibility. This term is not present when subtraction fringes are used. The I_o and ψ terms in the second part of the same equation also contribute noise that degrades the fringes.

One method of enhancing addition fringes is to capture a similar speckle pattern but with the object at rest, and then subtract this from the deformation fringes.[107] This method reduces background and fixed speckle noise but can produce spurious fringes,[108-110] owing to both rigid-body motion and object deformation. The spurious fringes cannot easily be separated from the deformation fringes, making automatic processing difficult.

A more valid method of enhancing fringe visibility is to remove the low-frequency background terms by means of filtering. Fourier-domain filtering[66] works well for

some images, although it is a global technique and is not optimised when there is localised noise or a Gaussian illumination profile within the image. Similarly, an analog high-pass filter can be applied to the video signal before it is digitised.[109]

Another form of high-pass filter is a variance filter, which replaces each pixel in the image by its variance calculated over a small window centred on it.[111] This filter also has an averaging effect that helps to eliminate speckle noise, but it does reduce the spatial resolution of the image slightly. However, it is a localised filter, and as such it copes reasonably well with highlights (e.g. specular reflections) within the image. The variance filter is given by

$$I_V(x,y) = \frac{1}{\hat{I}(x,y)} \sum_{i,j=-k}^{+k} \left[I(x+i, y+j) - \hat{I}(x,y) \right]^2 \tag{3.24}$$

where $\hat{I}(x\ y)$ is the mean of the pixel values in a $N \times N$ window centred on (x, y), and $k = (N-1)/2$. That is,

$$\hat{I}(x,y) = \frac{1}{N^2} \sum_{i,j=-k}^{+k} I(x+i, y+j) \tag{3.25}$$

Note that this filter (along with a number of other speckle-processing algorithms) is nonlinear, so it may produce harmonics in the calculated phase when using a phase-shifting algorithm.[112] Although its effects are mitigated when the Fourier method of Section 3.3.2 is used, a preferred approach[88] is to use a bilinear operator such as the average (or absolute) deviation:

$$I_{|D|}(x,y) = \frac{1}{N^2} \sum_{i,j=-k}^{+k} \left| I(x+i, y+j) - \hat{I}(x,y) \right| \tag{3.26}$$

This filter is of lower-order than the variance, making it less susceptible to highlights. Note that the influence of highlights can be further reduced by normalisation with $\hat{I}(x, y)$ instead of N^2. It also preserves the linearity of the fringes, lessening any quantisation effects. This was the filter used in the experiments in Chapter 5. Both

filters operate on the basis of the multiplicative noise term $\sqrt{I_o I_r}$ in Eq. (2.2). When the fringe amplitude due to object deformation is large then the fringes will be noisier and the localised deviation will also be large. In this way, the deviation is proportional to amplitude.

3.3.2 Phase Calculation

To extract quantitative, signed phase information from the fringes within an interferogram, some form of phase calculation method is required. From the discussion of phase extraction in Section 2.5, frequency-domain processing using the Fourier-transform method (FTM)[70,113] is a preferred technique, especially when using carrier fringes. This method will now be examined in more detail.

Supposing an interferogram is modulated by a linear vertical carrier fringe pattern[†] of frequency f, then Eq. (2.2) may be generalised as

$$I(x,y) = a(x,y) + b(x,y)\cos[\phi(x,y) + 2\pi fx] \tag{3.27}$$

where $a(x, y)$ represents the background intensity, $b(x, y)$ is the local contrast of the fringes and $\phi(x, y)$ is the object phase term to be evaluated.

The method is based on the assumption that the spatial variations of $a(x, y)$, $b(x, y)$ and $\phi(x, y)$ are slow compared with f. If these conditions are met the resulting phase will be a monotonic function, so that a unique phase will be determined both in magnitude and in sign. In this case, Eq. (3.27) is rewritten as

$$I(x,y) = a(x,y) + c(x,y)\exp[2\pi ifx] + c^*(x,y)\exp[-2\pi ifx] \tag{3.28}$$

where $c(x,y) = \frac{1}{2}b(x,y)\exp[i\phi(x,y)]$ and (*) denotes complex conjugation.

[†] Although the carrier frequency is shown as a function of one-dimension only, it may also have a component in the orthogonal direction, by design (Section 2.5.4) or through alignment errors.

Then, the fringe pattern given by Eq. (3.28) is Fourier transformed using a two-dimensional fast-Fourier transform algorithm to give

$$\tilde{I}(\upsilon,\nu) = A(\upsilon,\nu) + C(\upsilon - f,\nu) + C^*(-\upsilon - f,-\nu) \tag{3.29}$$

where the capital letters denote the Fourier transform and υ and ν are the spatial frequencies in the x and y directions, respectively.

Since the intensity $I(x, y)$ is a real distribution in the spatial domain, it can be shown that the amplitude spectrum is point symmetric to the zero frequency $(\upsilon, \nu) = (0, 0)$ and consists of three separated terms, corresponding to the three terms of Eq. (3.29).

One of these, the $C(\upsilon - f, \nu)$ term, may then be isolated by use of a bandpass filter function in the frequency plane. As the remaining spectrum is no longer Hermitian,[85] the inverse Fourier transform applied to $G(\upsilon, \nu) = C(\upsilon - f, \nu)$ gives a complex $g(x, y)$ with non-vanishing real and imaginary parts. Then the wrapped phase map of the addition fringes (object phase plus the carrier frequency) is calculated pointwise by

$$\phi(x,y) + 2\pi fx = \arctan\left\{\frac{\mathrm{Im}[g(x,y)]}{\mathrm{Re}[g(x,y)]}\right\} \tag{3.30}$$

with values wrapped between $-\pi$ and $+\pi$.

After unwrapping the phase (see next Section) from Eq. (3.30), the object phase $\phi(x, y)$ is determined by subtraction of the linear phase term $2\pi fx$, which is due to the carrier frequency. This can be performed by frequency-shifting $G(\upsilon, \nu)$ to the origin within the Fourier domain,[76,114] but this can cause problems if f is not an exact multiple of the pixel spacing (however, it does reduce the phase gradient thus reducing the number of phase wraps, which may be advantageous when unwrapping high-noise fringes). For this reason, the carrier frequency term is often found with a two-dimensional linear least-squares fit to the unwrapped phase.

3.3.3 Strain Calculation

Strain is used extensively in experimental mechanics for predicting and measuring the properties of materials and structures. Strain is a result of variations in the deformation throughout a body and is a function of the derivatives of displacement. If u, v and w are the components of displacement in the x, y and z directions, respectively, then the normal strains[115] are:

$$\varepsilon_x = \frac{\partial u}{\partial x}, \qquad \varepsilon_y = \frac{\partial v}{\partial y}, \qquad \varepsilon_z = \frac{\partial w}{\partial z} \tag{3.31}$$

The shear strain, for example the in-plane case, is given by

$$\gamma_{xy} = \gamma_{yx} = \frac{\partial u}{\partial y} + \frac{\partial v}{\partial x} \tag{3.32}$$

These partial derivatives can be calculated by numerical differentiation of the deformation data. However, if using simple finite-difference methods, the high noise content of the speckle fringes will produce highly noisy strain data. This can be mitigated by firstly reducing the noise in the speckle fringes through filtering, then calculating the phase, and lastly fitting a plane to the phase values in the neighbourhood of each pixel.[116,117] The plane, fitted using least-squares, gives the gradients in x and y simultaneously.

If using phase shifting, the phase derivatives can be calculated directly from the phase-shifted interferograms, without prior evaluation of the deformation.[118,119] This makes the process faster, and also avoids the need for phase unwrapping since the arctangent operator is not used.

Strain fringes can also be produced optically by means of shearing interferometry.[9] Shearing brings the light rays scattered from two neighbouring points on the surface into mutual interference. Shearing offers several advantages over deformation interferometers. Firstly, as the optical system is a common-path interferometer, the effects of air turbulence, as well as rigid-body motions such as tilt, are minimised.

Because no reference beam is required, the optical system is simpler. Finally, less demand is placed on the coherence of the source.

Carrier fringes have also been generated in shearing interferometers by using a divergent illumination source, which is then translated along its optical axis.[120,121] This induces a quadratic phase factor in the wavefront, the derivative of which (by means of the shearing system) gives linear carrier fringes.

Another means of calculating derivatives is through filtering in the frequency domain, specifically the Fourier derivative theorem (FDT).[85] If a function $f(x)$ has the Fourier transform $F(u)$, see Eq. (3.3), then the derivative $f'(x)$ has the Fourier transform of

$$\tilde{I}'(u) = \mathcal{F}\{f'(x)\} = 2\pi i u F(u) \tag{3.33}$$

Thus taking the 1st derivative of a function is equivalent to multiplying its transform by an imaginary linear filter of slope u. Inverse Fourier transforming then yields $f'(x)$:

$$f'(x) = \mathcal{F}^{-1}\{\tilde{I}'(u)\} = \int_{-\infty}^{\infty} \exp(2\pi i u x) 2\pi i u F(u) du \tag{3.34}$$

It then follows that the n^{th} derivative can be calculated using $(2\pi i u)^n$ as the filter term in Eq. (3.33). The FDT may be conveniently applied when extracting deformation phase from carrier fringe data while in the Fourier domain, i.e. the FTM and FDT can be combined to give strain and/or deformation data. Noting that the linear frequency-filter term effectively attenuates low frequencies and enhances high frequencies, this method also exhibits sensitivity to noise. However, with the combination of a low-pass filter in the frequency domain, the noise effects can be minimised.

The environmental robustness of shearing interferometers (due to their common path nature) sometimes makes them more suitable than deformation interferometers. However, in these cases deformation data is sometimes desired, rather than the native strain data. Deformation data can then be attained by integrating the strain data. As with derivatives, integrals are often cumbersome using numerical methods. However, the complement of the FDT, the Fourier Integral Theorem (FIT) can be employed to

good effect. If the Fourier transform of the sheared data is represented by $\tilde{I}'(u)$, then dividing by $2\pi iu$ and inverse Fourier transforming yields the deformation data, $f(x)$:

$$f(x) = \mathcal{F}^{-1}\{\tilde{I}'(u)/2\pi iu\} \tag{3.35}$$

The obvious singularity at $u = 0$ can be avoided by setting $\tilde{I}'(u)$ to zero at the zero frequency; since in this case the divisor represents the d.c. or 'piston' term in the imaginary spatial domain, and the data in only the real spatial domain is of interest, its value is arbitrary.

Example calculations demonstrating the utility of the FDT and FIT are given in Chapter 5 and Appendix A, the latter also showing a novel apodisation scheme to attenuate ringing and noise in the spatial domain, plus a novel amalgamation with the Fourier transform method for carrier fringes. The FDT and FIT, while not strictly new, have not been used extensively within the field of speckle, particularly so for the FDT.

One approach[47,122] to the FDT applied computer-generated carrier fringes to the wrapped deformation phase (to elucidate the sign of deformation), and then calculate the strain phase from the FDT. Also, the Gerchberg[123] iterative extrapolation algorithm was used to minimise aperture effects. Three points should be noted here: firstly, carrier fringes are not necessary for the FDT (see Appendix A); secondly, if using carrier fringes, the FDT can be combined with the FTM, thus eliminating a step (see Appendix A); lastly, non-iterative apodisation can be employed to mitigate aperture effects (see Appendix A).

For the FIT, some[124,125] have used a complex filter function to minimise the noise propagation to the integrated data, although no deformation data was shown. Another work[126] has compared the frequency responses of the FIT and numerical methods, concluding that the FIT has a flatter response. To cope with large shears, a novel technique[127] used masks to reconstruct the data over the full aperture (including non-sheared edges), although only presented simulated data.

3.3.4 Phase Unwrapping

Owing to the cosinusoidal nature of interference fringes, the phase calculated from them is naturally periodic. Most phase calculation methods incorporate the arctangent function [e.g. Eq. (3.30)], which wraps the phase modulo-2π. The wrapped phase must then be unwrapped to form a continuous phase map.

This is a straightforward process[128] in well-behaved phase maps. In such maps the absolute phase gradient $|\Delta\phi(x)|$ between adjacent samples is less than π (except for the 2π arctangent wrapping, i.e. $-\pi < |\Delta\phi(x)| \leq \pi$). It is then a simple matter to progress through the phase map, adding or subtracting integer multiples of 2π such that the absolute phase gradient is less than π:

$$\phi(x, y) = \psi(x, y) + 2\pi k(x, y) \tag{3.36}$$

where $\psi(x, y)$ is the wrapped phase in the interval $(-\pi, \pi]$, $k(x, y)$ are integers and $\phi(x, y)$ is the unwrapped phase. Ordinarily the unwrapped phase should be independent of the path taken during the unwrapping process since the phase is single-valued.

When the π-gradient condition is exceeded in the continuous phase, unwrapping becomes more difficult. The condition can be exceeded because of noise, low fringe modulation, discontinuous object phase (discontinuous object surface or absence of phase information owing to shadows or occlusions), or spatial undersampling of the fringe pattern. The ideal phase-unwrapping algorithm, then, should work with complex object shapes and flow around obstacles, be path-independent, recognise real discontinuities and keep the noise localised in high-noise situations.

The field of phase unwrapping research is very diverse and prolific. Many different types of algorithms have been proposed, in domains from ESPI to synthetic-aperture radar. Despite the diversity of phase-unwrapping algorithms, most fall into one of only a few categories, namely: localised path-following, global optimisation, or temporal. Comprehensive reviews of techniques have been published by several authors,[11,129,130] along with a comparison between local and global schemes,[131] a comparison based on

fidelity of unwrapping different types of phase maps[132] and a comparison based on the noise-sensitivity of different algorithms.[133]

Local techniques[128,129] are often simple one-dimensional path-following algorithms applied in two dimensions. These tend to suffer in the presence of noise (especially the high noise levels inherent in ESPI fringes), because noise can easily propagate spatially in one or more dimensions. Local techniques are also sometimes heuristic, and often rely on user input to fine-tune the result. The effects of noise can be mitigated somewhat by unwrapping by means of local neighbourhoods.[116]

Temporal algorithms[32,134] work on the basis of multiple phase maps being acquired during the deformation of an object. If the maps are acquired at a sufficient rate so that the phase difference between successive maps is less than π, then simple one-dimensional unwrapping can be performed at each pixel along the time axis, independent of other pixels. This has the advantage that errors tend to remain highly localised, unlike many of the spatial techniques. It does, however, require that the data be acquired quickly enough (including time for phase shifting or carrier modulation) so that the phase does not alias in the time direction and that the acquisition system can handle a large number of interferograms.

Global unwrapping methods utilise the whole phase map to minimise the overall error in the unwrapped phase. They also tend to be analytically based, unlike many local techniques. Most global algorithms employ statistical minimisation, such as least-squares, but differ in the method of solution and the conditions they impose on the solution. The least-squares formulations appear suited to ESPI due to their robustness in the presence of noise.

One such global algorithm is based on a two-dimensional least-squares formulation (LSF), with the discrete cosine transform in the solution.[135,136] By taking the gradient of the wrapped phase, re-wrapping over the interval $(-\pi, \pi]$ to remove discontinuities and then comparing this with the gradient of the (notionally) final unwrapped phase, the problem can be cast as a least-squares error minimisation. The least-squares equation then conveniently takes the form of a 2nd-order partial differential equation,

which can be solved using one of a variety of standard techniques. By using a cosine expansion, a solution can be implemented using the computationally-efficient cosine transform,[85] the continuous form of which is given by

$$\mathcal{F}_C\{f(x)\} = 2\int_0^\infty f(x)\cos(2\pi ux)dx \tag{3.37}$$

Note: this is equivalent to a Fourier transform if $f(x)$ is an even function, cf. Eq. (3.3).

A limitation of this type of algorithm is its use of first differences of the phase in its solution—a poor estimator of the phase gradient when the phase is noisy, as with ESPI. To circumvent this problem, the bandpass filter in the Fourier phase calculation method of Section 3.3.2 should be narrow enough to block most of the speckle noise—a condition that is readily achievable in practice. As a further precaution against noise or other inconsistencies, the algorithm can be designed to incorporate a mask that removes inconsistent data from the unwrapping process.[123†] By use of a weighting matrix that assigns a weight of zero to problem pixels, these pixels are ignored in the LSF solution and then interpolated from good neighbouring data in the unwrapped phase. This form of the LSF requires iterative solution, but is generally fast to converge; for this reason and for its robustness against noise, it was used for the experiments in this thesis.

3.4 SUMMARY

In this chapter, the gamut of carrier fringe modulation, demodulation, phase calculation, strain calculation and phase unwrapping were covered. Various practical configurations for carrier generation were designed and analysed, employing both electro-mechanical and electro-optical modulators. For simplicity, stability and repeatability, galvanometer mirrors and acousto-optic modulators appear to offer many benefits. However, measuring phase is of little use if its accuracy is unknown. In the next chapter, the accuracy of different types of interferometer geometries is analysed, and options for minimising or eliminating errors are presented.

† This book also contains source code.

4 Sensitivity Analysis

Optical interferometric techniques such as ESPI and Holographic Interferometry (HI) have been used for many years in laboratories and industries as diagnostic tools. In recent years, the increasing and widening use of these techniques has focused more attention to questions concerning their accuracy.

A variety of systematic and random errors can affect interferometric measurements. A major source of systematic error can arise in the calculation of the object deformation phase from the primary data, the interferometric fringe patterns. As discussed in Chapter 2, the two main methods of phase calculation are phase shifting and the Fourier transform. Significant effort has been directed towards phase-shifting algorithms, desensitising them to spatial errors in phase-shift interval (linear and nonlinear), as well as intensity nonlinearities in detectors.[56,137] Errors induced by filtering phase-shifted ESPI fringes have also been examined.[138] The errors that can result from the Fourier transform method have also been discussed by a number of authors.[71,114,139]

A source of systematic error that has received less attention is one that arises when using noncollimated illumination, specifically when calculating the physical object deformation from the interferometric phase. Because of the size of many objects (large relative to the optical components of the interferometer) or the physical constraints of the measurement environment (e.g. endoscopic systems,[140] or internal combustion engines,[141]) divergent illumination is often used. This is perhaps typified by the design of instrumentation currently available from commercial vendors. However, the standard models of deformation measurement[142] (as introduced in Chapter 2) are typically valid only for collimated illumination, or noncollimated illumination in the paraxial region. This is because the sensitivity vector of deformation is a function of both the illumination and observation directions, which

vary with the three-dimensional (3D) position of each point on the object surface. Thus the direction of the sensitivity vector will vary across an object, and also vary with the relief of the object.[143,144]

Recently, several authors have investigated aspects of the errors that can result from this situation. Examples include one-dimensional (1D) out-of-plane (OOP) cases,[145] two-dimensional (2D) planar objects for specific OOP and in-plane (IP) geometries,[146] OOP endoscopic systems with planar objects,[140] and 1D errors associated with OOP speckle-shearing measurements.[147] The 1D and 2D theoretical models that have been proposed have in some cases been supported by experimental data. Although these have generally produced good correlations, most of the data has been analysed in 1D. However, because of divergent (spherical) illumination (i.e. the wavefront gradient varies in 2D), 1D analyses do not give an accurate representation over the full extent of objects, which are mostly 2D or 3D. Another limitation of existing analyses is that they are usually confined to systems of specific dimensions,[148,149] the results of which cannot easily be extrapolated to other systems because of the nonlinear nature of the sensitivity equations.

In this Chapter, the issue of 3D error mapping is analysed.[144] A comprehensive deconstruction of the 3D systematic sensitivity variations of both OOP and IP interferometers as a function of noncollimated illumination is presented, in which the deformation of nonplanar 2D objects is considered. Furthermore, a scalable approach to system parameters is employed to make the analysis generic, and hence applicable to a wide variety of interferometers. Error functions are derived, and from the plots of these functions it is observed that the error magnitudes can be considerable. The plots can be used as a guide to when errors start to become significant, and the functions can be used to correct for sensitivity errors once they become excessive. The second-order effects of positional errors are small and are addressed briefly in section 4.3.2.

To begin, sensitivity equations are derived for both OOP and IP interferometers. Then a novel, generic geometrical description is introduced to make the analyses scalable. Finally, the sensitivity errors are plotted to demonstrate the behaviour of the errors for different interferometer geometries.

4.1 OUT-OF-PLANE INTERFEROMETER

An OOP displacement-sensitive interferometer configuration is the first to be considered. In this section the sensitivity equations are derived, along with the error functions for when divergent illumination is used.

4.1.1 Geometry

With reference to the OOP interferometer of Fig. 4.1, an object in the (x, y, L) plane is illuminated by a point source s in the (x, y, 0) plane (parallel and coincident with the object plane), and the scattered light is observed with a camera at a point t in the same plane. The object's maximum dimensions are between $-X_m$ to $+X_m$ and $-Y_m$ to $+Y_m$ laterally and between $-Z_m$ to $+Z_m$ in relief. When the object undergoes deformation, the resulting displacement vector **d** of a particular point produces an optical path difference (OPD), which causes a phase change in the signal detected at the camera. The displacement is defined as $\mathbf{d} = d_1\mathbf{u} + d_2\mathbf{v} + d_3\mathbf{w}$, where **u**, **v**, **w** are the unit vectors

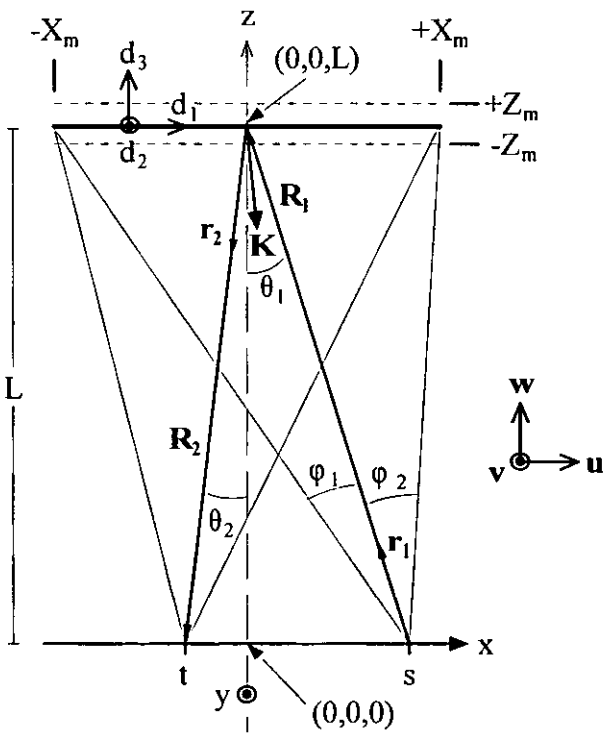

Fig. 4.1: OOP deformation interferometer configuration.

in the x, y, z directions, respectively. The phase change $\Delta\phi$ is given by the scalar product:

$$\Delta\phi = \mathbf{K} \cdot \mathbf{d} = \frac{2\pi}{\lambda}(\mathbf{r}_2 - \mathbf{r}_1) \cdot \mathbf{d} \tag{4.1}$$

where **K** is the sensitivity vector with a direction along the bisector of the illumination (unit vector $\mathbf{r}_1$) and observation (unit vector $\mathbf{r}_2$) beams, and λ is the wavelength of illumination.

Because **d** is 3D, the interferometer is not sensitive solely to OOP displacement components, for certain directions of **K**. To isolate the three vector components of displacement, three illumination beams can be used.[81,115] If the three resulting sensitivity vectors are noncoplanar, then the vector displacement can be determined from

$$\begin{bmatrix} \Delta\phi_1 \\ \Delta\phi_2 \\ \Delta\phi_3 \end{bmatrix} = \frac{2\pi\hat{\mathbf{K}}}{\lambda} \cdot \begin{bmatrix} d_1 \\ d_2 \\ d_3 \end{bmatrix} \tag{4.2}$$

where $\hat{\mathbf{K}}$ is a 3×3 sensitivity matrix defined by the geometry of the system. However, multiple object beams are not well-suited to dynamic measurements or noisy environments because of the time taken to introduce carrier fringes or perform phase shifting. Additionally, in many situations, objects deform primarily in one direction.

For a single direction of illumination, Eq. (4.1) can be reduced[142] to the common form:

$$\Delta\phi = \frac{2\pi}{\lambda}[(\cos\theta_1 + \cos\theta_2)d_3 + (\sin\theta_1 - \sin\theta_2)d_1] \tag{4.3}$$

When $\theta_1 = \theta_2 = 0$, Eq. (4.3) reduces to the conventional form of Eq. (2.4), and is wholly-sensitive to d_3 displacements. Note that when $\theta_1 \neq \theta_2$, the system also exhibits sensitivity to d_1 displacements. Note also that if $\theta_1 \neq 0$ and $\theta_2 \neq 0$, then the sensitivity range can be extended beyond that of Eq. (2.4). Equation (4.3) is a good

approximation around the object centre $(x, y) = (0, 0)$ or when collimated illumination is used (i.e. the illumination vectors are parallel). However, when divergent illumination is employed, the direction of the sensitivity vector will vary point-by-point across the object in x, y and z. A similar effect occurs as a consequence of using a nontelecentric imaging system. It is therefore necessary to derive equations that more fully describe a divergent system and then quantify the associated errors.

4.1.2 Sensitivity Equations

Some previous investigations have used a wave approach[147] to analyse sensitivity, in which the assumption was that planar objects were being examined. It is appropriate in the current context to use a ray-based approach because it is more versatile for the task at hand, particularly when the object relief varies. It is assumed that the source lies in the (x, y, z) plane at a position $(s, 0, 0)$. This forms an illumination vector $\mathbf{R}_1$ with the object. Similarly, the entrance pupil of the imaging system lies at position $(-t, 0, 0)$ and forms an imaging vector $\mathbf{R}_2$. Now, $\mathbf{R}_1$ can be expressed as

$$\mathbf{R}_1 = (x - s)\mathbf{u} + y\mathbf{v} + z\mathbf{w} \tag{4.4}$$

The magnitude of $\mathbf{R}_1$ is then

$$|\mathbf{R}_1| = \sqrt{(x - s)^2 + y^2 + z^2} \tag{4.5}$$

The equivalent unit vector of $\mathbf{R}_1$ is given by

$$\mathbf{r}_1 = \frac{x - s}{|\mathbf{R}_1|}\mathbf{u} + \frac{y}{|\mathbf{R}_1|}\mathbf{v} + \frac{z}{|\mathbf{R}_1|}\mathbf{w} \tag{4.6}$$

A similar unit vector can be formed for $\mathbf{R}_2$:

$$\mathbf{r}_2 = \frac{t - x}{|\mathbf{R}_2|}\mathbf{u} - \frac{y}{|\mathbf{R}_2|}\mathbf{v} - \frac{z}{|\mathbf{R}_2|}\mathbf{w} \tag{4.7}$$

Now, substituting Eqs. (4.6) and (4.7) into Eq. (4.1) and expanding, yields the phase difference at the detector plane:

$$\Delta\phi(x, y, z) = \frac{2\pi}{\lambda}\left\{\left[\frac{t - x}{\sqrt{(t - x)^2 + y^2 + z^2}} - \frac{x - s}{\sqrt{(x - s)^2 + y^2 + z^2}}\right]d_1\right.$$

$$+\left[\frac{-y}{\sqrt{(t - x)^2 + y^2 + z^2}} - \frac{y}{\sqrt{(x - s)^2 + y^2 + z^2}}\right]d_2$$

$$\left.+\left[\frac{-z}{\sqrt{(t - x)^2 + y^2 + z^2}} - \frac{z}{\sqrt{(x - s)^2 + y^2 + z^2}}\right]d_3\right\} \tag{4.8}$$

Equation (4.8) represents the phase difference for the noncollimated illumination case.

It is now necessary to compare Eq. (4.8) with the collimated (plane wavefront) case, to determine the relative errors associated with divergent illumination. It is noted that, for the collimated case, the direction of $\mathbf{r}_1$ is constant over the object. That is, its direction is the same as $\mathbf{r}_1$ at (0, 0, z), for the noncollimated case. Thus if $\Delta\phi(x, y, z)$ is calculated at (0, 0, z), then this forms a reference sensitivity, allowing the calculation of a relative sensitivity error for the whole system. In order to simplify the sensitivities, Eq. (4.8) is redefined as

$$\Delta\phi(x, y, z) = \frac{2\pi}{\lambda}(K_1 d_1 + K_2 d_2 + K_3 d_3) \tag{4.9}$$

where K_1 is the horizontal IP sensitivity, K_2 is the vertical IP sensitivity and K_3 is the OOP sensitivity (their x, y, z dependencies have been dropped for clarity). The sensitivities for the collimated case can now be defined as

$$K_{1_c} = K_1(0, 0, z)$$

and similarly for K_{2_c} and K_{3_c}.

In many experimental and commercial systems, the camera axis is set perpendicular to, and coincident with the centre of, the object (i.e. $t = 0$). This avoids the need to correct the image for perspective distortions. Using this geometry, then from Eq. (4.8) it can be seen that, for the collimated case $\Delta\phi(0, 0, z)$, the following will hold true:

$$K_{1_c} = \frac{s}{\sqrt{s^2 + z^2}} \tag{4.10}$$

$$K_{2_c} = 0 \tag{4.11}$$

$$K_{3_c} = -\left(1 + \frac{z}{\sqrt{s^2 + z^2}}\right) = -(1 + \cos\theta_1) \tag{4.12}$$

where it is noted that Eq. (4.12) is the d_3 sensitivity factor of the conventional OOP equation [Eq. (4.3)], for $t = 0$. Because K_{2_c} is zero, there is no vertical IP sensitivity, as expected. However, K_{1_c} is nonzero (when $s \neq 0$), indicating that the OOP configuration is sensitive to horizontal IP displacement when $\theta_1 \neq 0$. A relative measure of this is

$$K_{1_c}/K_{3_c} = \frac{-s}{z + \sqrt{s^2 + z^2}} \tag{4.13}$$

For example, if $\theta_1 = 45°$, then a collimated OOP system will exhibit 40% sensitivity to any horizontal IP displacement, relative to the OOP sensitivity.

For the noncollimated case, a set of relative sensitivities is defined. Because in this case the primary interest is in the measurement of OOP displacement compared with the collimated case, K_{3_c} is used as a reference to form the following quotients:

$$\rho_{31} = K_1 / K_{3_e} \tag{4.14}$$

$$\rho_{32} = K_2 / K_{3_e} \tag{4.15}$$

$$\rho_{33} = (K_3 - K_{3_e}) / K_{3_e} \tag{4.16}$$

where ρ_{31}, ρ_{32} and ρ_{33} are the relative sensitivities of an OOP configuration to horizontal IP, vertical IP, and OOP displacement, respectively. ρ_{31} and ρ_{32} may also be termed the cross-sensitivities, and ρ_{33} the OOP auto-sensitivity. Equations (4.14)–(4.16) are a measure of the error, or sensitivity variation, associated with use of divergent illumination in place of a plane wavefront and ideally should be zero. Their actual values are plotted in Section 4.3 for a range of typical situations.

4.2 IN-PLANE INTERFEROMETER

The sensitivity equations and error functions are now derived for an IP displacement-sensitive interferometer that uses divergent illumination.

4.2.1 Geometry

An IP interferometer should ideally have 100% sensitivity to one direction of IP displacement and zero sensitivity to the other two orthogonal directions of displacement. Typically, an IP interferometer consists of two illumination sources, s_1 and s_2, positioned either side of a detector with entrance pupil at (0, 0, 0), as shown in Fig. 4.2. These illuminate the object situated in the (x, y) plane, centred at (0, 0, L). For this analysis, it is assumed that the illumination and detection systems are centred with respect to the centre of the object. The phase difference that is due to a displacement **d** is given by

$$\Delta\phi = \frac{2\pi}{\lambda} (\mathbf{r}_1 - \mathbf{r}_2) \cdot \mathbf{d} \tag{4.17}$$

In this instance, the sensitivity vector **K** is perpendicular to the bisector of the two illumination beams ($\mathbf{r}_1$ and $\mathbf{r}_2$). When collimated illumination is used, Eq. (4.17) can be approximated[142] by

$$\Delta\phi = \frac{2\pi}{\lambda}[(\sin\theta_1 + \sin\theta_2)d_1 + (\cos\theta_1 - \cos\theta_2)d_3] \tag{4.18}$$

Now, if $-s_1 = s_2$ (i.e. $\theta_1 = \theta_2$), Eq. (4.18) reduces to the conventional form of Eq. (2.6). For this condition, then $\mathbf{K} = 2\pi(\mathbf{r}_1 - \mathbf{r}_2)/\lambda$ is parallel to the x (horizontal) axis, and hence sensitive to only d_1 displacements and is also independent of the viewing direction. When $\theta_1 \neq \theta_2$, the system also exhibits sensitivity to d_3 displacements. However, as will be shown Section 4.3, even when $\theta_1 = \theta_2$ the system exhibits sensitivity to d_2 and d_3 displacements if noncollimated illumination is used.

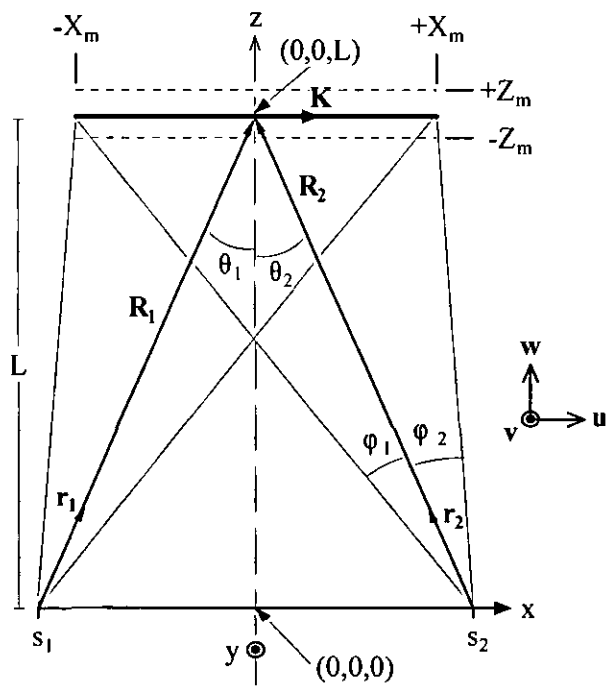

Fig. 4.2: IP deformation interferometer configuration.

4.2.2 Sensitivity Equations

As with the OOP case, equations are formed for the two major vectors, in this case the two illumination vectors $\mathbf{R}_1$ and $\mathbf{R}_2$ shown in Fig. 4.2:

$$\mathbf{R}_1 = (x - s_1)\mathbf{u} + y\mathbf{v} + z\mathbf{w} \tag{4.19}$$

$$\mathbf{R}_2 = (x - s_2)\mathbf{u} + y\mathbf{v} + z\mathbf{w} \tag{4.20}$$

The corresponding unit vectors are then given by

$$\mathbf{r}_1 = \frac{x - s_1}{|\mathbf{R}_1|}\mathbf{u} + \frac{y}{|\mathbf{R}_1|}\mathbf{v} + \frac{z}{|\mathbf{R}_1|}\mathbf{w} \tag{4.21}$$

$$\mathbf{r}_2 = \frac{x - s_2}{|\mathbf{R}_2|}\mathbf{u} + \frac{y}{|\mathbf{R}_2|}\mathbf{v} + \frac{z}{|\mathbf{R}_2|}\mathbf{w} \tag{4.22}$$

Substituting Eqs. (4.21) and (4.22) into Eq. (4.17) yields the phase difference related to the geometry of the system:

$$\Delta\phi(x, y, z) = \frac{2\pi}{\lambda}\left\{\left[\frac{x - s_1}{\sqrt{(x - s_1)^2 + y^2 + z^2}} - \frac{x - s_2}{\sqrt{(x - s_2)^2 + y^2 + z^2}}\right]d_1\right.$$

$$+\left[\frac{y}{\sqrt{(x - s_1)^2 + y^2 + z^2}} - \frac{y}{\sqrt{(x - s_2)^2 + y^2 + z^2}}\right]d_2$$

$$\left.+\left[\frac{z}{\sqrt{(x - s_1)^2 + y^2 + z^2}} - \frac{z}{\sqrt{(x - s_2)^2 + y^2 + z^2}}\right]d_3\right\} \tag{4.23}$$

As described for Eq. (4.8), Eq. (4.23) can be simplified to the form of Eq. (4.9). For collimated illumination, $\mathbf{r}_1$ and $\mathbf{r}_2$ have constant direction over the object and are the same as the noncollimated case at $\Delta\phi(0, 0, z)$. Then from Eq. (4.23), and assuming $s = -s_1 = s_2$, the sensitivities for the collimated case are

$$K_{1_e} = \frac{2s}{\sqrt{s^2 + z^2}} = 2 \sin \theta \tag{4.24}$$

$$K_{2_e} = 0 \tag{4.25}$$

$$K_{3_e} = 0 \tag{4.26}$$

It is noted that there is no OOP or vertical IP sensitivity, as expected, and that Eq. (4.24) represents the sensitivity factor of the conventional IP equation [Eq. (4.18)], when $\theta_1 = \theta_2$.

For the noncollimated case, a series of relative sensitivities can be formed, similar to the OOP configuration. Here the concern is primarily with the horizontal IP sensitivity, hence K_{1_e} is used as the reference:

$$\rho_{11} = (K_1 - K_{1_e})/K_{1_e} \tag{4.27}$$

$$\rho_{12} = K_2/K_{1_e} \tag{4.28}$$

$$\rho_{13} = K_3/K_{1_e} \tag{4.29}$$

Equations (4.27)–(4.29) represent the relative error, or sensitivity variation, associated with use of divergent illumination over collimated illumination for a horizontal IP interferometer, when subject to horizontal IP, vertical IP and OOP displacements, respectively.

4.3 SENSITIVITY ERRORS

Having derived sensitivity and error functions for both OOP and IP interferometers, it is now time to employ these functions in the characterisation of different interferometer geometries. A generalised, scalable parameterisation is introduced, followed by plots of the sensitivity variations and discussion of the errors for various geometries of OOP and IP interferometers.

4.3.1 Ratiometric Parameterisation

To make the sensitivity models applicable to a wide range of interferometer geometries, a generic, scalable description is required. One means of achieving this is to use dimensionless quantities, such as ratios of the basic system parameters. Several of these are defined as follows:

Aspect ratio, $R_A = |L/2\,X_m|$ (4.30)

Profile (relief) ratio, $R_P = |L/Z_m|$ (4.31)

Source offset ratio, $R_S = |s/L| = |\tan\theta|$ (4.32)

Object ratio, $R_O = |X_m/Z_m| = R_P/2\,R_A$ (4.33)

These ratiometric parameters are chosen to reflect the major features of an interferometer, such as distance from image plane to object, as well as aspects of the object itself, such as object size and object surface feature magnitude. It is expected, for example, that as R_A increases then the illumination more closely approximates a planar wavefront and the sensitivity errors will decrease. For a given R_A, and assuming the other parameters remain constant, the error should not change even though the scale of the system may change. For systems with folded optical paths (e.g. with mirrors to direct the beams), the equivalent unfolded path lengths can be used.

4.3.2 Out-of-Plane System

Using the ratios of Eqs. (4.30)–(4.33) the sensitivity error can be plotted in a manner that allows direct comparison with a system of any size and having different arrangements of elements; for example, plotting error against R_A for multiple values of R_S. To evaluate the contributions of the individual components of displacement on the OOP configuration of Fig. 4.1, the errors were separately assessed for each of the three terms ρ_{31}, ρ_{32} and ρ_{33}, corresponding directly to the three components of displacement d_1, d_2 and d_3. The combined error could be calculated instead, but as this is dependent on the magnitude and direction of each displacement component, these components would have to be known *a priori*. The sensitivity calculations were performed using Mathcad. Examples of the calculations are shown in Appendix B.

For the initial analysis, the error variation across a planar object is considered for a fixed R_A. For the purposes of the calculations, some realistic values are chosen for the parameters: L = 1000 mm, X_m = 250 mm (i.e. R_A = 2.0). The ρ_{33} sensitivity error is then calculated over (x, y, L) for various values of R_S, using Eq. (4.16). The result is

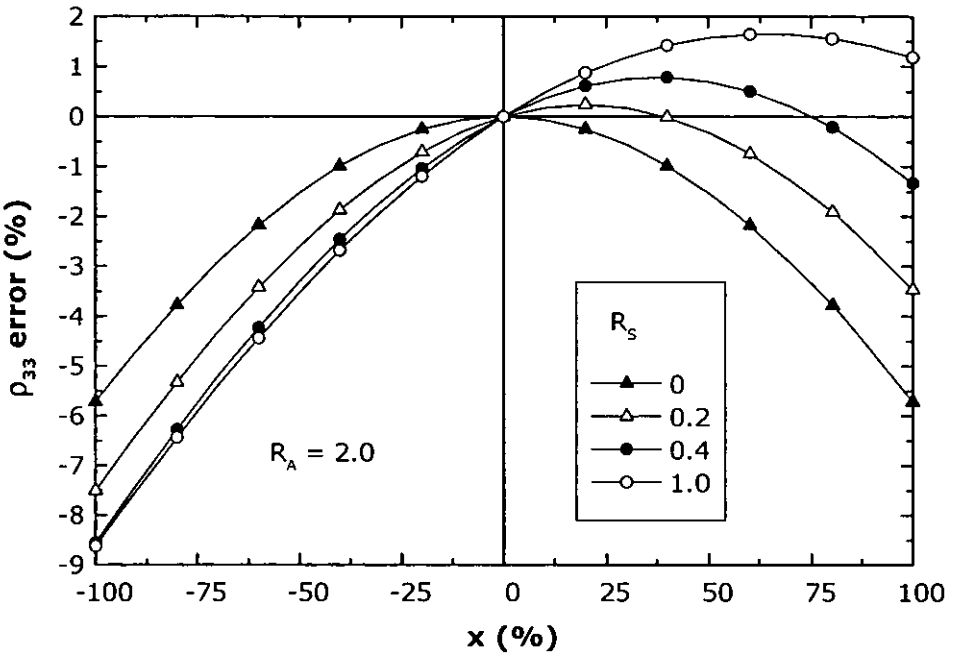

Fig. 4.3: Relative sensitivity error for an OOP system with d_3 displacement and R_A = 2.0, plotted along diagonal of planar object.

plotted in Fig. 4.3 for R_S = 0 to 1.0, along the diagonal of the object (expressed as a percentage of its half-width), where the error usually (but not always) reaches the maxima. As expected, the error is zero at the centre of the object as this equates to the collimated case. It is noted from Fig. 4.3 that the response is nonlinear and that, as R_S increases, the error increases (in this case, by up to nearly -9% for R_S = 1.0) and also becomes asymmetric because $\varphi_1 \neq \varphi_2$ (see Fig. 4.1). The second-order effect of positional errors can be deduced from Fig. 4.3: a source at 400 mm instead of 200 mm gives 1% error difference. For a more comprehensive understanding of the error behaviour, 3D and contour error maps are shown in Fig. 4.4. These are for the same system as Fig. 4.3, plotted over the full extent of the object in x and y (i.e. ±100%), for two different values of R_S.

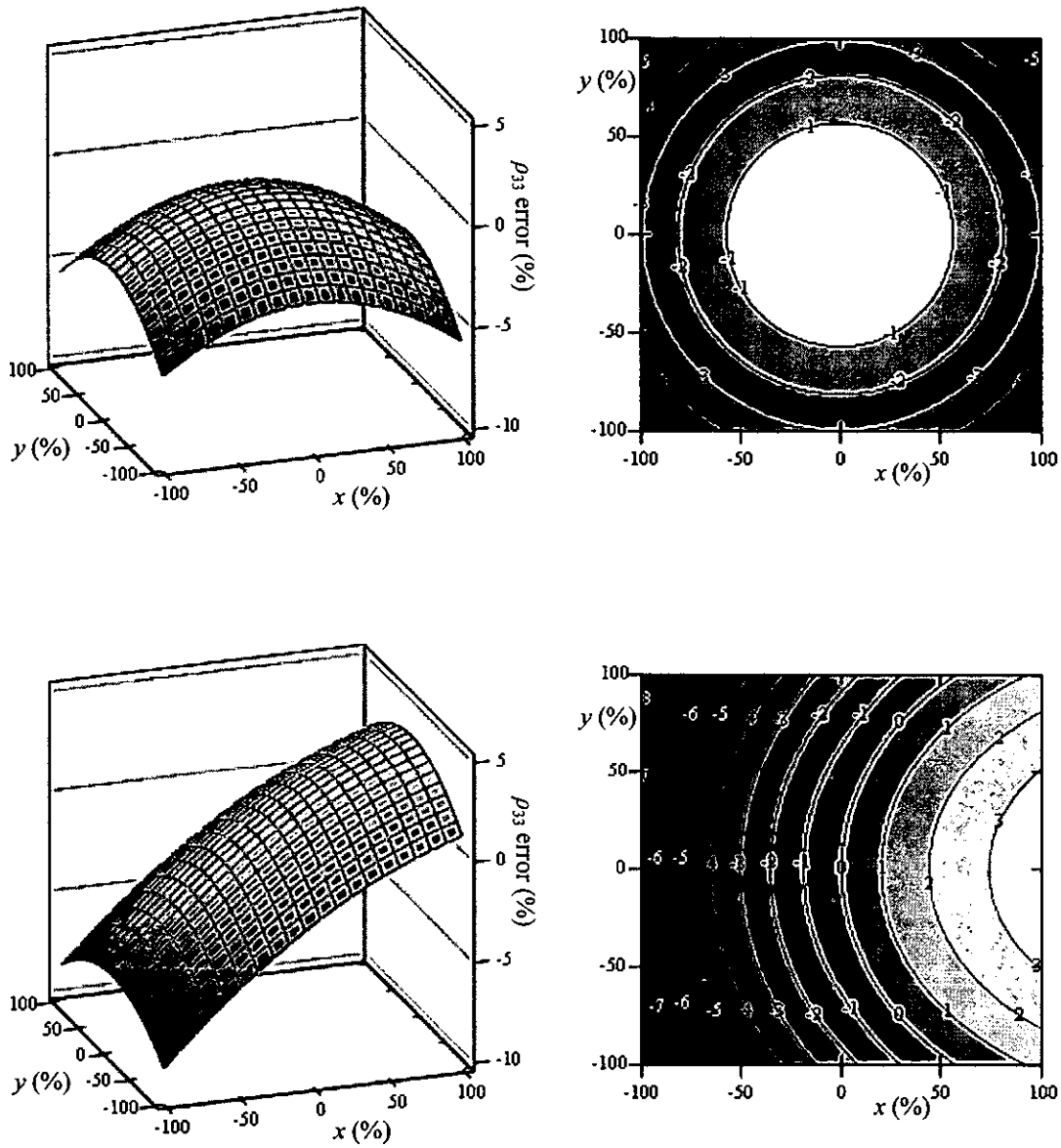

Fig. 4.4: 3D (left) and contour (right) maps of the relative sensitivity error ρ_{33} for an OOP system with d_3 displacement and $R_A = 2.0$, plotted over the full extent of the object in x and y (±100%); Top: $R_S = 0$; Bottom: $R_S = 1.0$.

The converse of the above analysis is to vary L (and hence R_A), while holding R_S constant. Using the same object half-width, X_m = 250 mm, L is varied between 500 mm and 2000 mm (i.e. $R_A = 0.5 - 2.0$). As L increases, R_S is held constant at 1.0 ($\theta = 45°$) by proportionately increasing the source displacement s. The ρ_{33} relative sensitivity error percentage is then calculated over (x, y, L) for the various values of L and s.

The result is plotted in Fig. 4.5, along the diagonal of the object, expressed as a percentage of its half-width. Again, the error is zero at the centre of the object because the error is calculated relative to the collimated case. The error is asymmetrical and increases substantially with decreasing R_A.

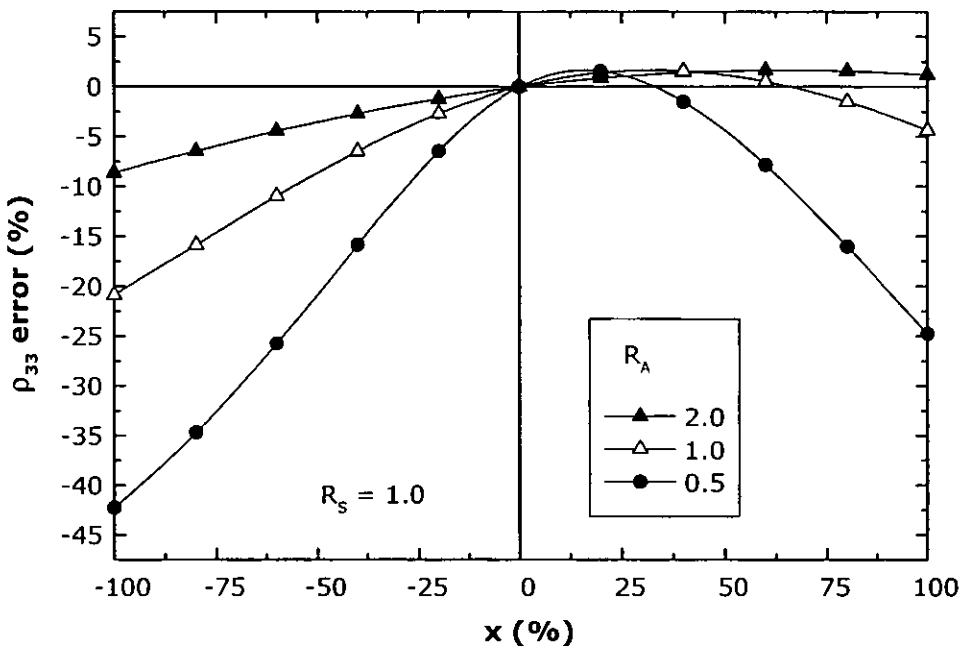

Fig. 4.5: Relative sensitivity error ρ_{33} for an OOP system with d_3 displacement and R_S = 1.0, plotted along diagonal of planar object.

Simulations using various profile ratios R_P, with Z_m from 0 to L, revealed that the error almost invariably increases with Z_m, an effect similar to decreasing L. For this reason, it is preferable to define L as the distance between the camera and maximum object relief (rather than mean object relief), i.e. $L = \langle L \rangle - Z_m$, where $\langle L \rangle$ is the mean distance to the object. Furthermore, because the error will also depend on the profile distribution, parameters such as R_P and the object ratio R_O, cannot be generalised unless they involve generic shapes (e.g. convex cylinder[150], concave sphere, etc.). As an example, an object in the form of a convex circular cylinder is analysed.

Considering a cylinder of radius r = 1000 mm with its curvature in the x direction and measured in a system with $R_S = 0$ and $R_A = 1.0$ (L = 1000 mm, X_m = 500 mm). This yields Z_m = 67 mm, $R_P = 14.9$ and $R_O = 7.5$. If the object is positioned with its mean relief at $z = L$, then the maximum ρ_{33} sensitivity difference from a planar object measured in the same system is only 1.7%. A 3D plot of the difference is shown in Fig. 4.6, where the x and y axes are expressed as a percentage of X_m and Y_m. In this case, the maximum error due to the cylinder (16.6%) is less than that due to a plane (18.3%). This is because the errors normally increase towards the edge of an object (large φ), as evident in Fig. 4.3, but with a convex cylinder, the edges are further away from the source, leading to a reduction in the errors. The situation is reversed with a concave object.

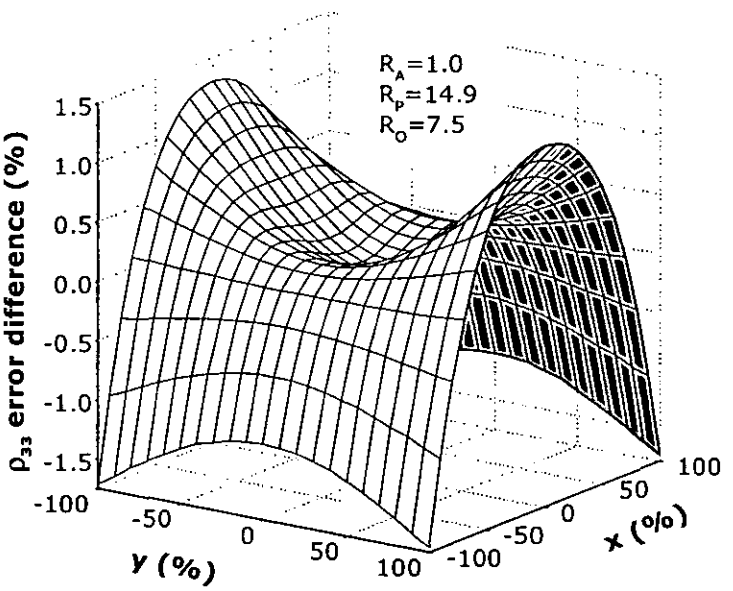

Fig. 4.6: Relative sensitivity error difference between convex-cylindrical and planar objects for an OOP system with d_3 displacement and $R_S = 0$.

Now the errors are examined for a planar object with varying values of R_A. To plot the graphs in Fig. 4.7, each of the sensitivity error functions was calculated over (x, y) using a range of parameters. In each case the maximum absolute value was taken as the error, indicating the maximum sensitivity error that can be expected when using a

particular geometry. Again, typical values were chosen for the parameters: L = 1000 mm, X_m = 500 to 50 mm (i.e. R_A = 1.0 to 10.0), and s = 0 to 1000 mm (i.e. R_S = 0 to 1.0).

In Fig. 4.7 logarithmic plots are shown of the ρ_{31}, ρ_{32} and ρ_{33} sensitivity errors against R_A, for several values of R_S. It is evident from the graphs that all the errors are nonzero and in some cases exhibit values of 70% or more. A common feature of all the graphs is that the errors decrease with increasing R_A. This is attributable to the illumination approximating a collimated source for large L, or equivalently a small X_m. From the OOP auto-sensitivity, Fig. 4.7 (bottom) (OOP displacement, d_3), it can be seen that reasonable error levels (say < 5% for ESPI) are achieved for R_A of more than approximately 3, with the error reducing with the reduction of R_S (i.e. source approaching central axis, $\varphi_1 \rightarrow \varphi_2$).

The cross-sensitivities of Fig. 4.7 (top and centre) (IP displacements, d_1 and d_2, respectively) show much larger errors for the same R_A and approach only a 5% error when R_A = 10 or more. Thus the OOP configuration is quite sensitive to any IP displacements present in the object being measured, particularly so for d_1 displacements as the source moves off-axis (this corresponds to a reduction in OOP sensitivity, which is proportional to $1 + \cos\theta$). For d_2 displacements the error is largely insensitive to R_S, attributable to the fact that d_2 is perpendicular to the source vector $\mathbf{R}_1$. For convenience, the equivalent angles for the various values of R_S are listed in the following table:

Source offset ratio R_S	0	0.2	0.4	0.6	0.8	1.0
Source offset angle θ	0°	11.3°	21.8°	31.0°	38.7°	45.0°

Table 4.1: Equivalent angles for various source offset ratios.

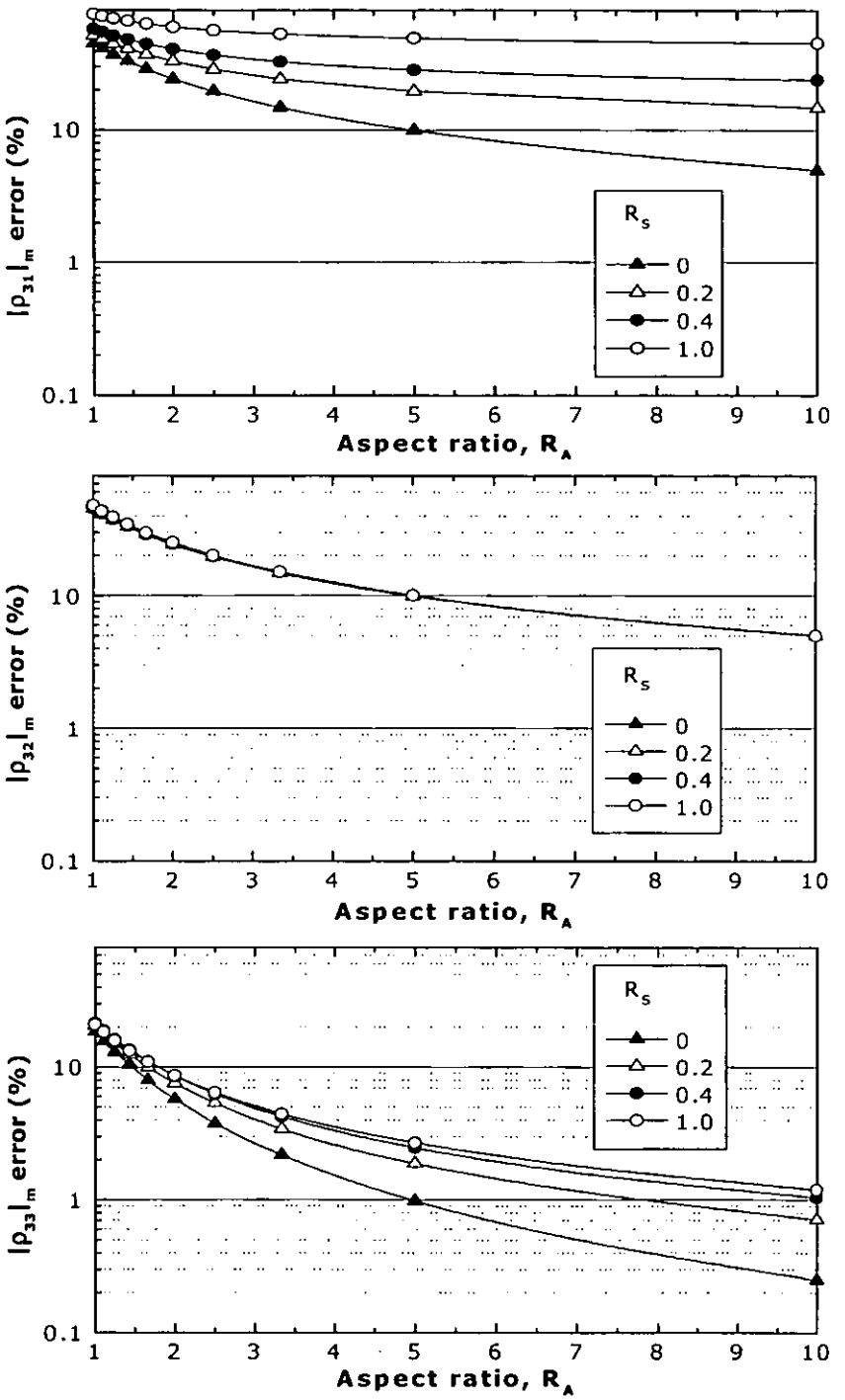

Fig. 4.7: Maximum relative sensitivity errors for an OOP system with planar object; d_1 displacement (top); d_2 displacement (centre); d_3 displacement (bottom).

A geometry similar to Fig. 4.1, but with $|\mathbf{R}_1| = L$ = constant, was derived. This gives a constant wavefront curvature for varying s (for $s \leq L$), allowing the wavefront curvature to be decoupled from other effects. Here it would be expected that larger errors would occur for larger s when compared with the geometry of Fig. 4.1, because the latter offers partial compensation by means of an increasing $|\mathbf{R}_1|$ that flattens the wavefront at the object. Simulations revealed that this was the case, with ρ_{31}, ρ_{32} and ρ_{33} errors higher than the Fig. 4.1 case by 1%, 13% and 26%, respectively, for $R_A = 10$ and $R_S = 0.62$ (equivalent illumination angle to θ_1 in Fig. 4.1 for $R_S = 0.8$, i.e. $\theta_1 = 38.7°$). Graphs of the error functions show very similar behaviour to the graphs of Fig. 4.7 (albeit with higher error levels), so have not been plotted here.

It should be emphasised that the ρ_{31}, ρ_{32} and ρ_{33} errors, or sensitivity *variations*, discussed in this section and in Section 4.3.3 are solely due to divergent illumination *relative* to collimated illumination. They do not include the standard geometry-related sensitivity factors that are present when $\theta > 0$; these are constant for constant θ and can be calculated from Eq. (4.3) [or Eq. (4.18) for the IP configuration]. Alternatively, the complete sensitivity map can be obtained by using the $K_n(x, y, z)$ sensitivity factors of Eq. (4.9) in place of the appropriate sine and cosine factors of Eqs. (4.3) or (2.4). For example, Eq. (2.4) then becomes: $\Delta\phi(x, y) = 2\pi\, K_3(x, y, z)\, d_3(x, y, z)/\lambda$

4.3.3 In-Plane System

For the IP configuration of Fig. 4.2, the ρ_{11}, ρ_{12} and ρ_{13} errors are now investigated. These correspond to the respective d_1, d_2 and d_3 components of displacement. The errors were calculated over (x, y) with the same ratiometric parameters as for the OOP case. Examples of the calculations are shown in Appendix B.

As with the OOP case, the error variation across a planar object for a fixed R_A is examined first. The same parameters are used: $L = 1000$ mm, $X_m = 250$ mm (i.e. $R_A = 2.0$). The ρ_{11} sensitivity error is then calculated over (x, y, L) for various values of R_S, using Eq. (4.27). The result is plotted in Fig. 4.8 for $R_S = 0.2$ to 1.0, along the diagonal of the object (expressed as a percentage of its half-width), where the error reaches the maxima.

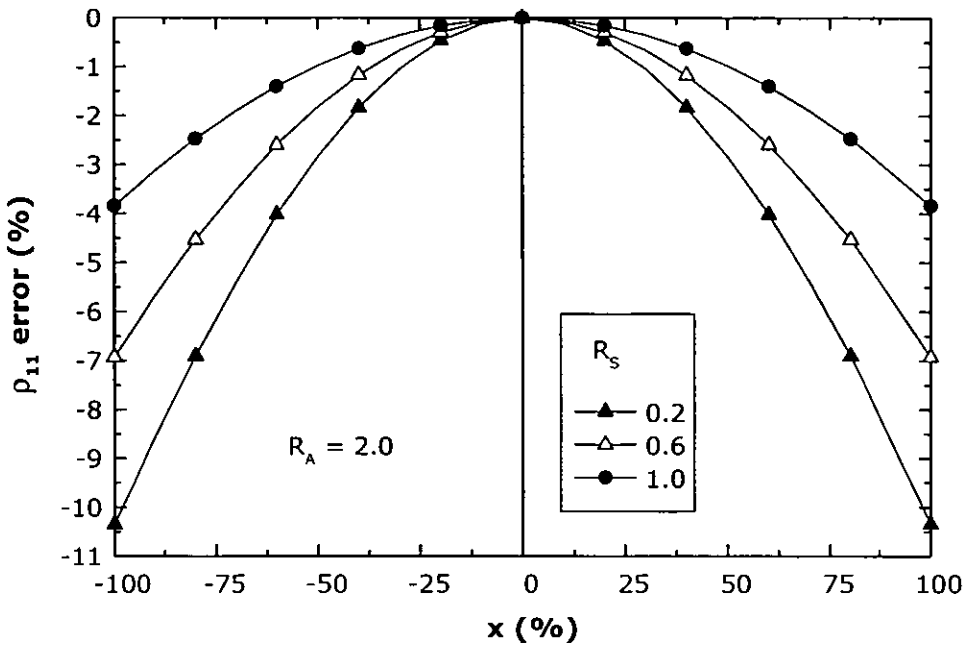

Fig. 4.8: Relative sensitivity error for an IP system with d_1 displacement and $R_A = 2.0$, plotted along diagonal of planar object.

Like the OOP case, the IP case displays zero error at the centre of the object (equating to the collimated case). However, unlike the OOP case, the IP case shows the error is symmetrical about the centre of the object (due to the symmetry of the interferometer, $\theta_1 = \theta_2$), and also that as R_S increases, the error reduces. To illustrate further the error behaviour, 3D and contour plots of the ρ_{11} error are shown in Fig. 4.9. These are for the same system as Fig. 4.8, plotted for two different values of R_S.

The errors are now plotted for varying values of R_A. The graphs in Fig. 4.10 are of the ρ_{11}, ρ_{12} and ρ_{13} sensitivity errors against R_A, for several values of R_S. The graphs reveal the errors as varying between 0.1% and 35%, and, as with the OOP configuration, the errors reduce with increasing R_A. From Fig. 4.10 (top) (IP displacement, d_1), the error drops below 5% for $R_A > 3$, reducing further with increasing R_S (i.e. sources moving off-axis).

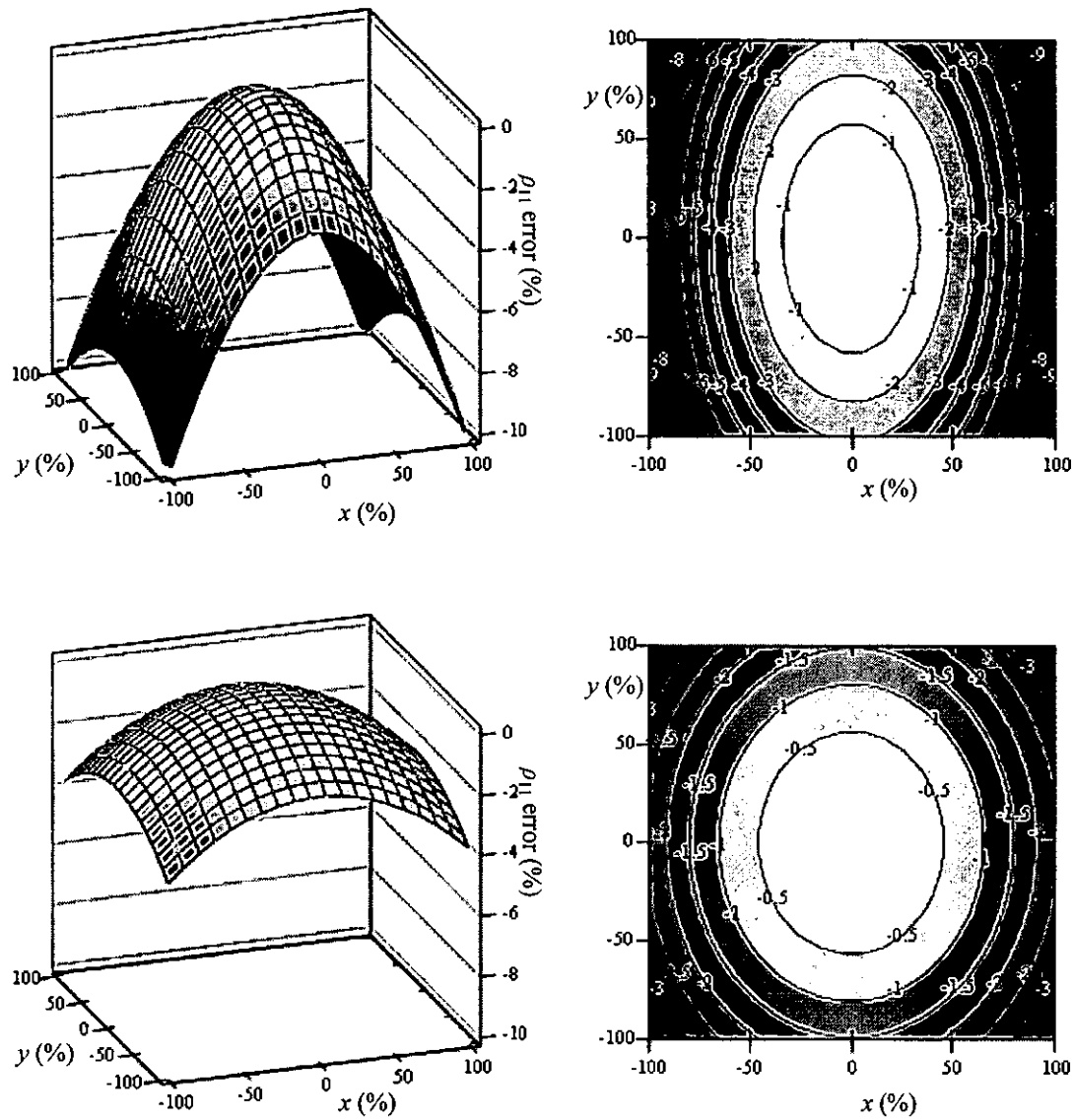

Fig. 4.9: 3D (left) and contour (right) maps of the relative sensitivity error ρ_{11} for an IP system with d_1 displacement and $R_A = 2.0$, plotted over the full extent of the object in x and y (±100%); Top: $R_S = 0.2$; Bottom: $R_S = 1.0$.

For IP displacement d_2 [Fig. 4.10 (centre)], the errors are slightly lower than for the d_1 case. There is also less error variation with respect to R_S than for the d_1 and d_3 cases. Again, this is due to d_2 being perpendicular to $\mathbf{R}_1$. The OOP displacement, d_3, case [Fig. 4.10 (bottom)] reveals larger errors than the d_1 case, showing that it is quite sensitive to OOP displacement, particularly for small R_S where the IP sensitivity ($\propto \sin\theta$) is reduced. These contrast with a collimated IP configuration, which has zero sensitivity to d_2 and d_3 displacements.

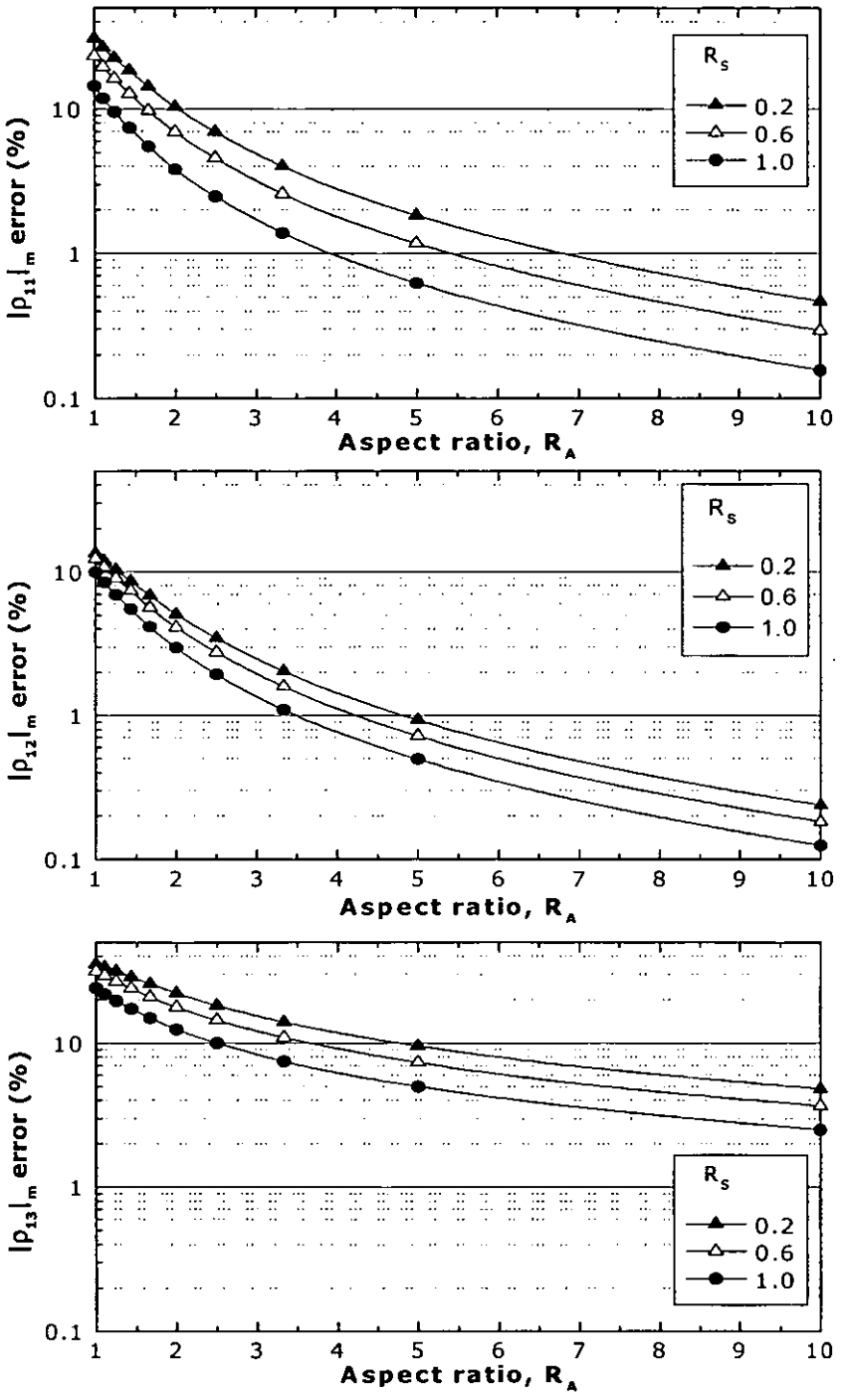

Fig. 4.10: Maximum relative sensitivity errors for an IP system with planar object; d_1 displacement (top); d_2 displacement (centre); d_3 displacement (bottom).

A similar geometry to Fig. 4.2 was derived, except with $|\mathbf{R}_1| = |\mathbf{R}_2| = L$ = constant. This has the feature of constant wavefront curvature when s is varied (for $s \leq L$). As expected, the errors for this geometry are larger, with the ρ_{11}, ρ_{12} and ρ_{13} errors higher than the Fig. 4.2 case by 59%, 64% and 28%, respectively, for $R_A = 10$ and $R_S = 0.62$ (equivalent to θ in Fig. 4.2 for $R_S = 0.8$).

4.4 SUMMARY

The derivation of sensitivity functions for interferometers that use divergent illumination has revealed that considerable errors are manifest in many geometries. The errors comprise three different types: primary, solely due to geometric factors of collimated (and noncollimated) interferometers; secondary, where noncollimated illumination produces sensitivity variations across an object and with the relief of an object; and tertiary, where cross-displacement components also intrude (e.g. IP displacement present when an OOP interferometer is used).

A novel, scalable, dimensionless model was developed, making the analyses applicable to a broad range of systems. The results as presented allow the errors of a particular system to be estimated, or conversely, a system can be designed to fit within a certain error budget. For the former case, if the errors are excessive, then the sensitivity equations herein can be applied to correct the errors of the system.

From the simulations of typical systems, substantial errors are observed for small aspect ratios, R_A (that is, for small object distance or large object diameter), which produce large wavefront curvatures. In addition, errors increase when the sources move on-axis for IP interferometers, or the source moves off-axis for OOP interferometers. The latter also exhibit asymmetric errors as the source moves off-axis. It was observed that measurements of d_2 displacements are generally less sensitive to source position than d_1 and d_3 displacements, when either d_1-sensitive IP or d_3-sensitive OOP interferometers are used. The relief of the object being measured also influences the errors, although for many systems this will be less than the above-mentioned errors. In Chapter 5 a number of experiments using these devices are presented and the results processed using the algorithms above.

5 Carrier Experiments

The novel phase measurement techniques explored in Chapter 3 and the new sensitivity model of Chapter 4 are now brought together and demonstrated in a number of experiments to confirm their practicability and efficacy. When designing a measurement system, it is desirable to use the simplest configuration that will do the job effectively. By minimising the number of optical components, the system cost will be lower, the image quality higher, and the system more reliable and easier to align. This is especially pertinent when conducting measurements in the field, where the environmental conditions can challenge alignment and stability. These factors are taken into account when designing the following systems for measuring harmonic vibrations, transient vibrations and profilometry.

Optical fibres are often used for beam delivery in interferometers.[151] These offer a high degree of flexibility and simplicity in the configuration and alignment of the interferometer, although they can be phase-sensitive to temperature and vibrational disturbances. Methods to overcome this include thermal and vibration insulating coverings on the fibres, or optical-feedback stabilisation schemes.[152] For the experiments herein, free-space beams were used as a means of demonstrating the various techniques, although they are equally applicable to fibre-based systems.

5.1 HARMONIC VIBRATIONS

Harmonic vibrational deformation is characterised by repeatable, periodic oscillatory motion of an object. As mentioned in Section 2.4.1, when the illumination is strobed in synchronisation with the object motion, good contrast fringes can be obtained while at the same time achieving good light efficiency. In these circumstances, and assuming there is little or no rigid-body movement (i.e. the surface is deforming rather than the object tilting or translating), then it is possible to acquire a reference (primary)

interferogram when the object is at rest. This can then be subtracted from the vibration (primary) interferograms, giving good contrast fringes (secondary interferograms), at frame rates if desired. A state diagram of the process is shown in Fig. 5.1, which is equally valid for static deformations. Fig. 5.1 shows a pure carrier phase map ϕ' being calculated, which is then subtracted from the object + carrier phase map ϕ'' to remove the carrier phase. Alternatively, the carrier phase can be removed using a linear least-squares fit, as in Section 5.2.

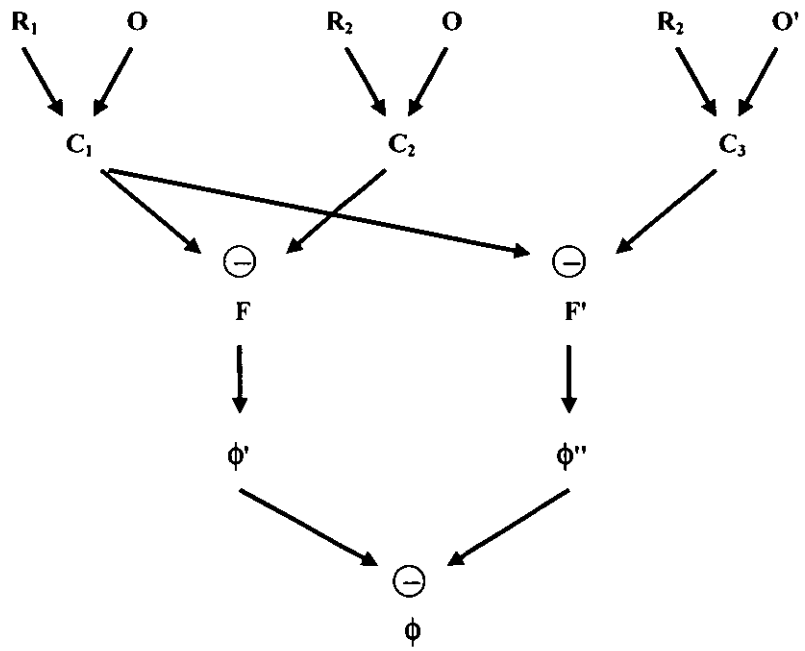

Fig. 5.1: State diagram for generation of ESPI deformation-modulated carrier fringes from static or harmonically-vibrating objects. R: reference wave (1 & 2 – different tilts, for carrier fringes); O: object wave before deformation; O': object wave after deformation; C: correlated speckle (primary interferograms); F: correlation fringes (secondary interferograms); ϕ': carrier phase; ϕ'': carrier + object phase; ϕ: object (deformation) phase.

5.1.1 Cylindrical Object

Experimental Configuration

To commence, carrier fringes were applied to measure the deformation and relief of a deterministic object – a thin-walled steel cylinder. The stroboscopic arrangement of Fig. 5.2 was used to capture the deformation of the object at particular instants in time. The cylinder's mode of vibration produces mostly out-of-plane (OOP) deformation, allowing the in-plane components to be dispensed with, thus simplifying the setup.

The light source consists of a 5 W (20 mW was used in practice) neodymium-vanadate solid-state continuous-wave laser (Coherent Verdi), operating at a wavelength of 532 nm. The object distance was 460 mm and the source offset was 230 mm.

The beam is strobed by an acousto-optic deflector (AOD) and then split into a reference and an object beam by a beamsplitter (BS). The reference beam is spatially filtered (SF) to remove spatially-coherent noise and improve fringe visibility,[50] before passing to the CCD camera via a nonpolarising beamsplitter (NPB). The object beam is reflected by a mirror mounted on a galvanometer[88] (GM), before expansion to irradiate the cylinder. The galvanometer (General Scanning), as discussed in Section 3.2.2, allows the mirror to be rotated through a small angle, in a controllable and repeatable manner, as a means of introducing the linear carrier phase.

The cylinder (diameter 101 mm, height 195 mm, wall thickness 3 mm) was rested on rubber to minimize reflections from the steel table, and set into resonance by means of

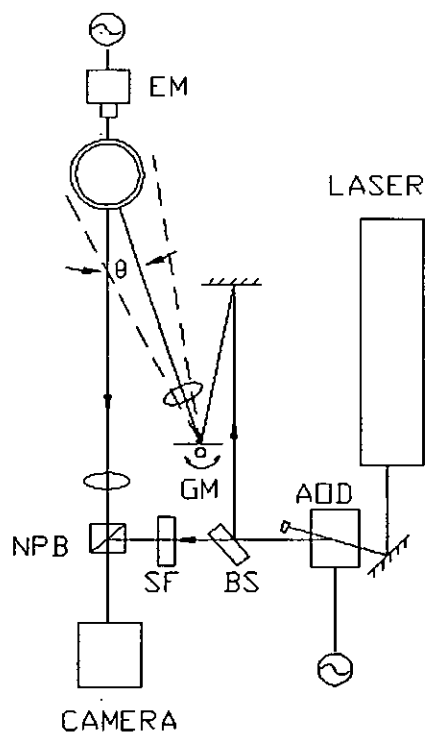

Fig. 5.2: Combined deformation and shape measurement ESPI system. EM: electro-magnetic driver; NPB: nonpolarising beamsplitter; SF: spatial filter; BS: beamsplitter; GM: galvanometer mirror; AOD: acousto-optic deflector.

a sinusoidally-driven moving-coil mechanism (EM). The acousto-optic deflector (AA Electro Optique) was synchronized to the object vibration by triggering a pulse generator at the epoch of the vibration cycle. Varying the phase of the pulse then allows different parts of the vibration cycle to be measured.[49] Choice of the pulse width is a trade-off: if it is too short then more light is required; if it is too long then too much of the motion is integrated, which degrades the fringe visibility. In this experiment there was sufficient light to have a short pulse duration of 4% of the total cycle time.

Results and Discussion

Measurements were first made over the full object height (195 mm) to examine the vibrational mode of the cylinder. The cylinder was set into a resonance at 1.96 kHz. Fig. 5.3 is a composite image showing the subtractive [Eq. (2.1)] deformation fringes (without carriers) at three different time instants during the cycle, each separated by 90°, or 127.5 μs. The modes are elongated in the direction of the cylinder major axis, with a node at approximately ¼ of the distance from the bottom. The outer images are in antiphase and the middle image is close to the equilibrium position.

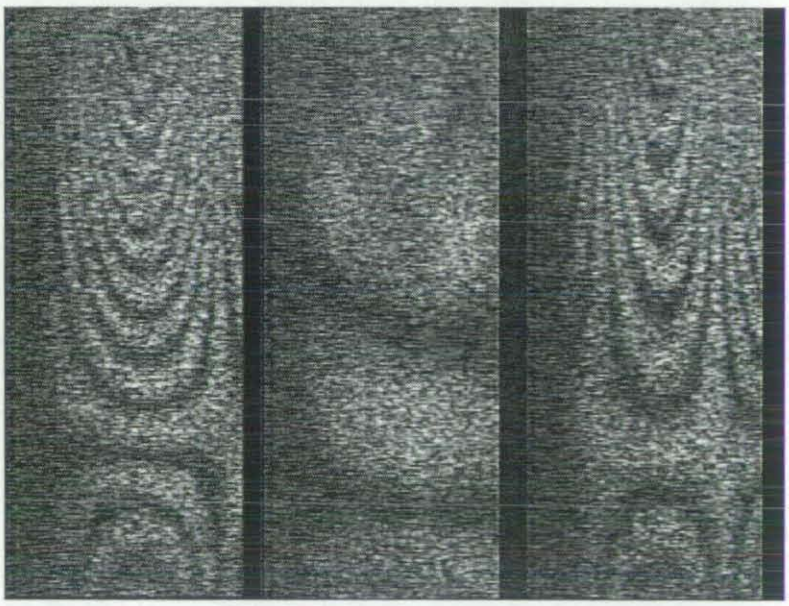

Fig. 5.3: Harmonic vibration of the cylinder at 1.96 kHz; composite of three images having quadrature phase.

The central 100 mm portion of the cylinder was investigated in more detail. For this, carrier fringes were used so that quantitative information could be extracted. After capturing a reference image, a horizontal carrier frequency was introduced and another image captured. Fig. 5.4 (a) shows the correlation between these two images, where approximately 16 vertical fringes are present, and these are modulated by the shape of the cylinder. Next, the cylinder was set into resonance at 1.96 kHz, and two more images captured, with temporal phase differences of 180°. Correlation with the reference image produces the deformation- and shape-modulated carriers of Fig. 5.4 (b) and (c).

(a) (b) (c)

Fig. 5.4: (a) Profiling carriers; (b), (c) Harmonic deformation carriers at 1.96 kHz.

After application of the Fourier phase extraction (Section 3.3.2) to the shape fringes of Fig. 5.4 (a), the phase is unwrapped[128] and the carrier removed. Scaling in the z-direction via Eq. (2.7) yields the relief. A 3-dimensional plot of the relief is shown in Fig. 5.5, along with a section through the center of the relief, showing good agreement with a theoretical cylinder.

The phase of the deformation fringes [Fig. 5.4 (b) and (c)] was then calculated, from which the wrapped phase due to the shape is subtracted. Fig. 5.6 (a) and (b) show the contours of phase due to the deformation, after removal of discontinuities[128] and correction of sensitivity variations. Fig. 5.6 (c) is a horizontal section through Fig. 5.6 (a), at 25 mm from the top of the image.

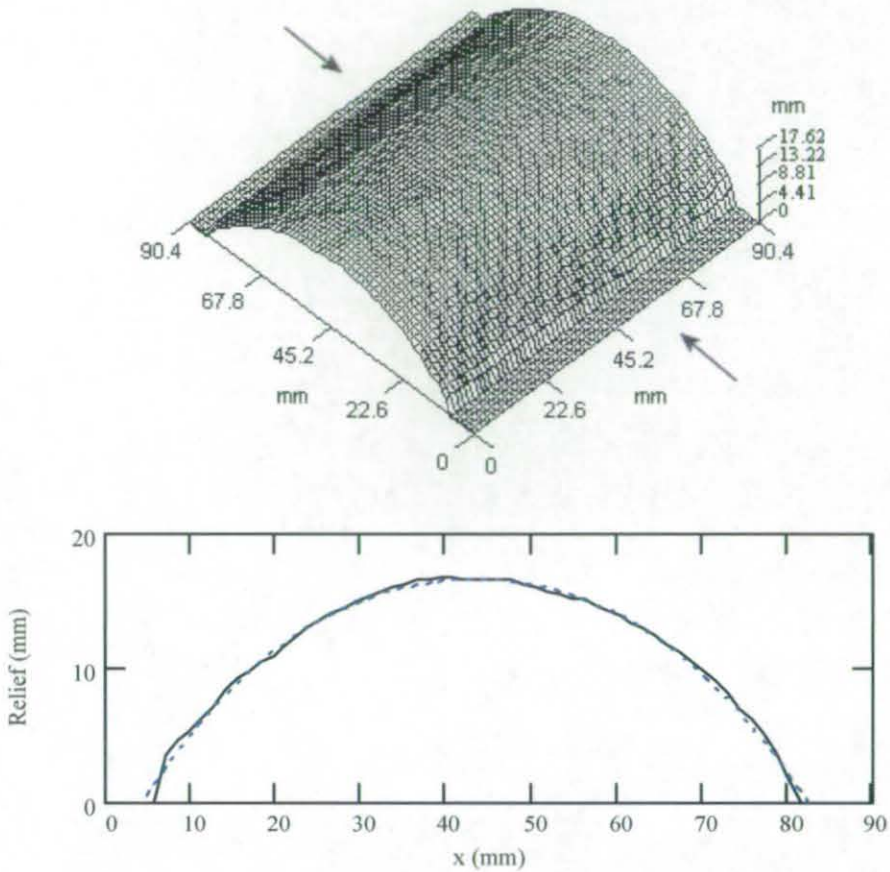

Fig. 5.5: Relief of cylinder surface; Top: 3D map; Bottom: 2D profile from arrowed region (solid trace: measured relief; dotted trace: theoretical cylinder).

The effects of divergent illumination and the object shape were incorporated using the sensitivity analysis of Chapter 4. The sensitivity variation of the deformation (divergent relative to plane-wave illumination) is plotted across the diagonal of the object and shown in Fig. 5.7, where the shape of the object has also been incorporated.

The full 3D sensitivity correction map, which also includes the effect of the object beam angle, is shown in Fig. 5.8. This represents the reciprocal of the $K_3(x, y, z)$ sensitivity factor of Eq. (4.9), and is the factor by which the deformation phase is multiplied in order to calculate the deformation of Fig. 5.6 (along with a $\lambda/2\pi$ factor).

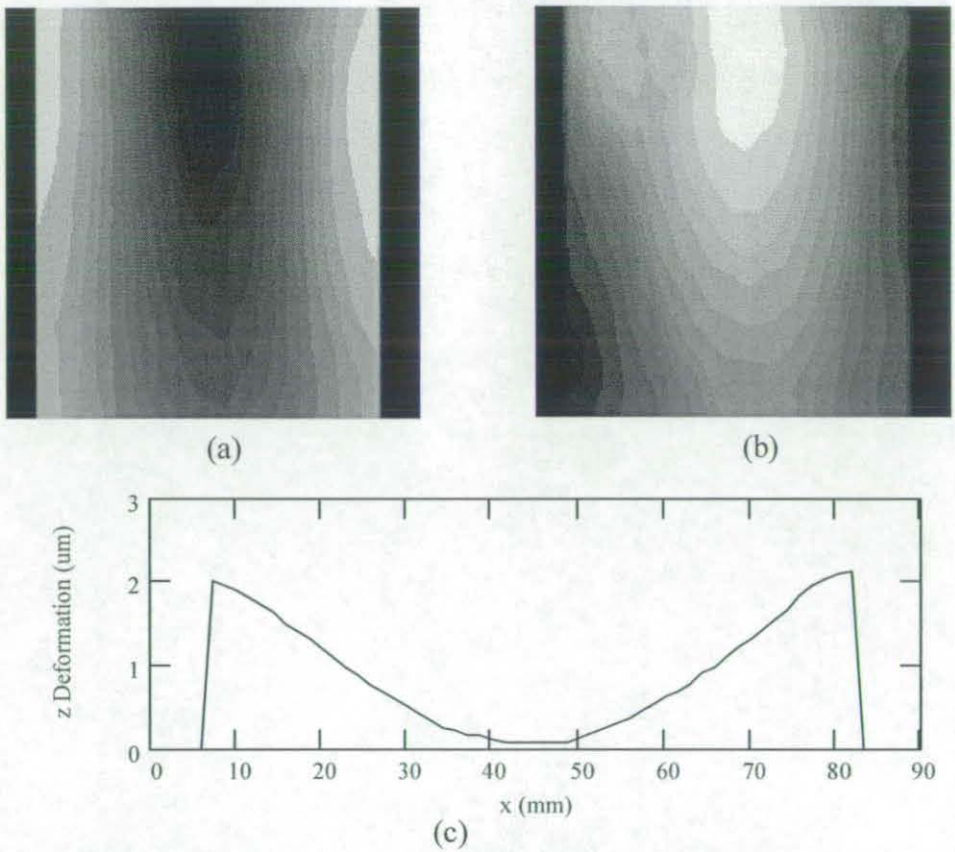

Fig. 5.6: (a), (b) Deformation contours, derived from Fig. 5.4 (b) and (c), respectively; (c) Horizontal profile through (a), showing relative deformation in the *z*-direction.

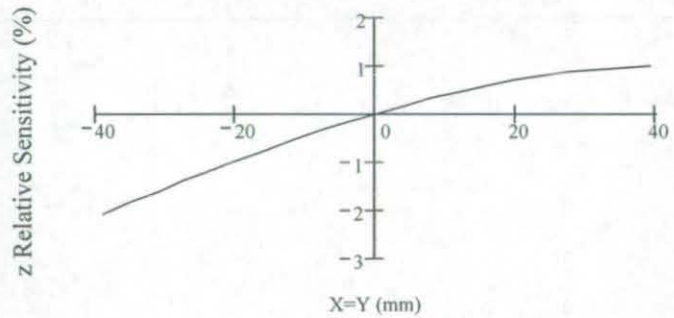

Fig. 5.7: Relative sensitivity across diagonal of object, incorporating curvature of object.

The profile of Fig. 5.6 shows a maximum relative deformation of approximately 2 μm, as projected onto the *z*-axis. The effect of the sensitivity correction is shown in Fig. 5.9, which is the difference between the corrected and uncorrected deformation. Here the maximum deformation error is about 40 nm, and will increase significantly as the object distance is decreased.

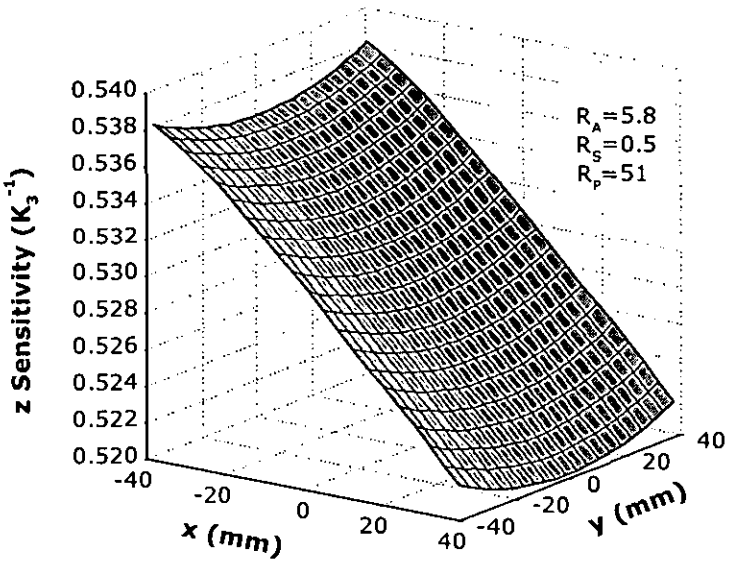

Fig. 5.8: 3D sensitivity correction map for cylinder measurement.

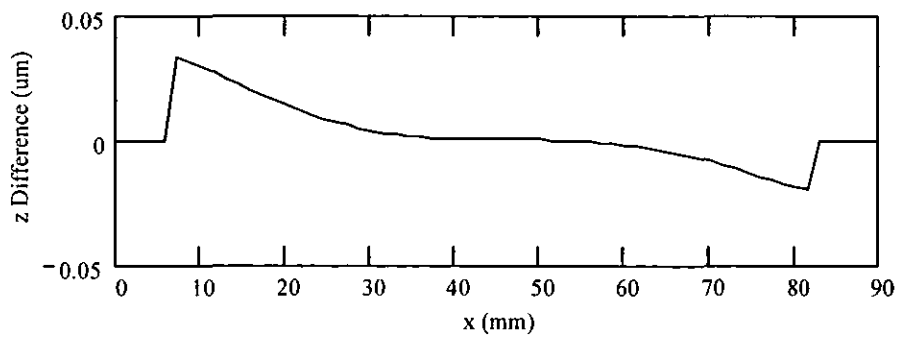

Fig. 5.9: Difference between corrected deformation profile of Fig. 5.6 (c) and corresponding uncorrected deformation profile.

5.1.2 Internal Combustion Engine

A system similar to the aforementioned is now employed to measure a more complex item with irregular shape. The subject in this case is a prototype internal combustion engine. The manufacturer of this diesel engine—the Lister-Petter company—conducted simple acoustic tests with the engine running. These tests revealed higher than acceptable levels of noise and vibration, but with no accurate quantification or localisation of the sources. It was envisaged that ESPI, in conjunction with laser Doppler velocimetry[1-3,152] (LDV), could offer such information.

Previous work[153] has reported a combination of ESPI and LDV, where an LDV was used to phase lock an ESPI system, achieving automatic heterodyning and providing a stable measurement configuration. In the present work, point (LDV) and area (ESPI) measurements were combined to quickly locate and quantify undesirable resonances in the engine, permitting specific changes to be made and the effects of the changes to be rapidly verified. The fringes were stabilised using a strobed illumination system, synchronised to the engine vibration. Furthermore, because of the irregular nature of the engine's shape, measurement of the surface shape was completed and used to qualify the deformation measurements.

Optical System

A diagram of the OOP deformation stroboscopic ESPI configuration used in the experiments is shown in Fig. 5.10. A laser passes through an AOD before being split

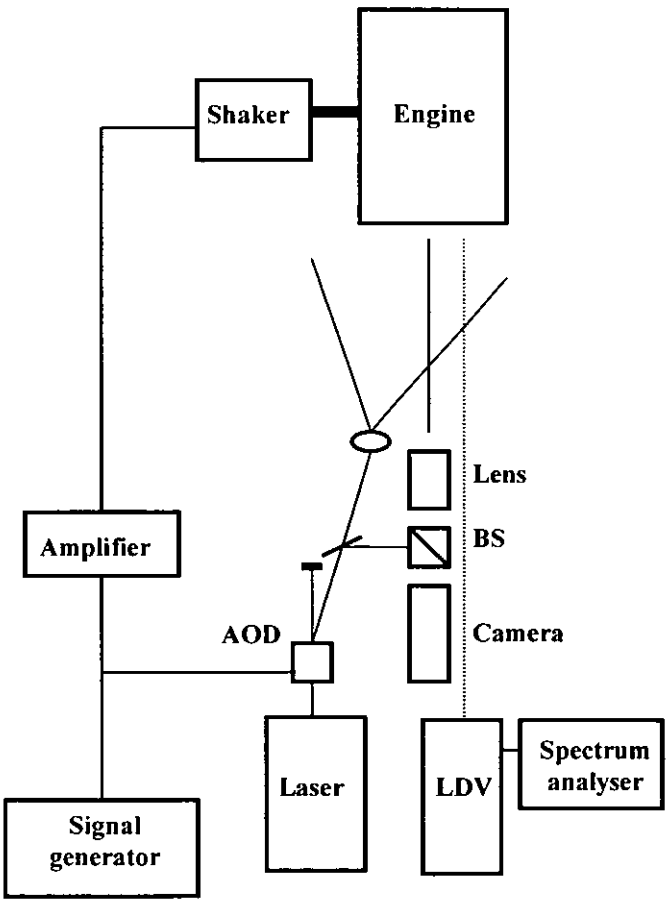

Fig. 5.10: Out-of-plane ESPI system for measuring engine vibration. BS, beamsplitter; AOD, acousto-optic deflector; LDV: laser Doppler velocimeter.

into a reference and an object beam. The object beam is expanded to illuminate the object while the reference beam is spatially filtered and directed into the camera by a beamsplitter. A camera views the object, also through the beamsplitter. A 200 N electro-mechanical shaker attached to the engine simulates the vibration experienced when the engine is normally running. A signal generator drives the shaker via a power amplifier. The signal generator also provides a synchronisation signal for the AOD, to ensure the laser illumination occurs at a pre-determined instance of the object's vibration cycle. The object distance was 900 mm and the source offset 350 mm.

A separate Polytec Model 302 LDV is used to probe the engine, to determine the areas of most significant velocity amplitude and the dominant frequencies of such. The principle of operation is that of the detection of the Doppler shift in the frequency of light scattered from the vibrating surface, as described by[154]

$$E_T(t) = E_T \cos[\omega t + \varphi_T - 2ka_v \sin \omega_v t] \tag{5.1}$$

where ω is the laser light frequency, E_T and φ_T are the respective amplitude and phase of the light incident at the detector with the target in its central position. a_v and ω_v are the respective amplitude and frequency of the target vibration, and $k = 2\pi/\lambda$. The signal processing electronics (Polytec Model 3000) then outputs an analogue voltage proportional to the velocity of the vibrating surface, which can be integrated to a time-varying displacement signal.

To correct for potential changes in sensitivity due to the nonplanar object surface, the surface relief was also measured. Careful consideration must be given to the quality of the relief data, since excessive errors or noise may reduce the accuracy and/or certainty of the deformation data, rather than improving it.

The profiling of the surface relief was achieved through the ESPI configuration, in a similar manner to the previous experiment in Section 5.1.1. By tilting the object beam appropriately (in this case manually), carrier fringes with spatial wavelength λ_S are obtained, which allow determination of both the amplitude and sign of the relief phase. These fringes are recorded separately, without vibration present. When the fringe

direction is non-parallel to the plane-of-incidence (illumination–viewing plane), the fringe spacing is sensitive to surface relief. For the case where the fringes are perpendicular to the plane-of-incidence, the measured phase is related to the surface relief through Eq. (2.7).

Experiments

Fig. 5.11 shows a photograph of the engine used in this investigation, a four-cylinder prototype diesel engine. To provide control over the experiment, engine running frequencies were simulated by attaching a large magnetic shaker (200 N Ling Dynamic Systems) to one of the cylinder head studs (top of Fig. 5.11). By driving the shaker with a mono-frequency sinusoidal signal through an amplifier, the engine could be excited into resonance over a range of frequencies. In this particular configuration, the shaker was driving in a vertical direction, parallel to the motion of the pistons.

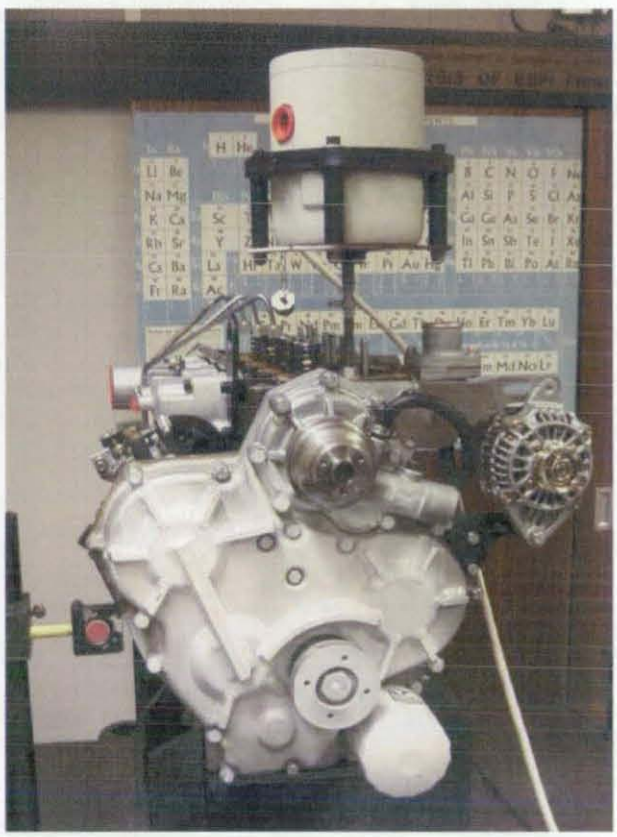

Fig. 5.11: Engine with the shaker attached. Timing chain cover is in foreground, showing prototype stiffening ribs.

Changing the position of the shaker to a different cylinder head stud did not significantly affect the results, but was necessary to compensate for the fixed positions of the stationary pistons inside the engine cylinders.

Initially, the LDV was used to probe points on the engine suspected of high amplitudes of vibration. The shaker was driven with a white-noise (uniform frequency spectrum) signal to approximate the normal running mode of the engine, and the output of the LDV was fed to a spectrum analyser (Scientific Atlanta SD380), set for 6.25 Hz spectral resolution.

A typical spectrum plot is shown in Fig. 5.12, where it is seen that most of the energy is concentrated in the 1.8 kHz to 4.0 kHz range, a band where the human auditory system is very sensitive to noise. There are a number of peaks in this range, with the maxima centred at 2.8 kHz. This plot is for point number seven (on the front of the timing chain cover), and showed the highest energy of the nine points measured. The locations of the excitation points on the cylinder head bolts (A–E) and the measurement points (1–9) are given in Fig. 5.13.

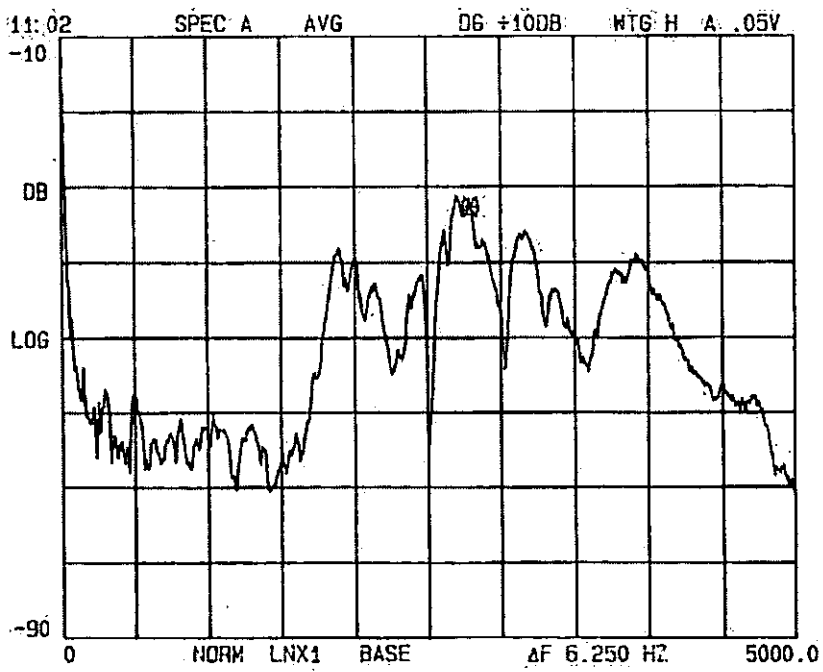

Fig. 5.12: LDV spectrum for location seven on the timing chain cover of the engine (linear 0–5000 Hz frequency range with 6.25 Hz resolution and logarithmic power scale).

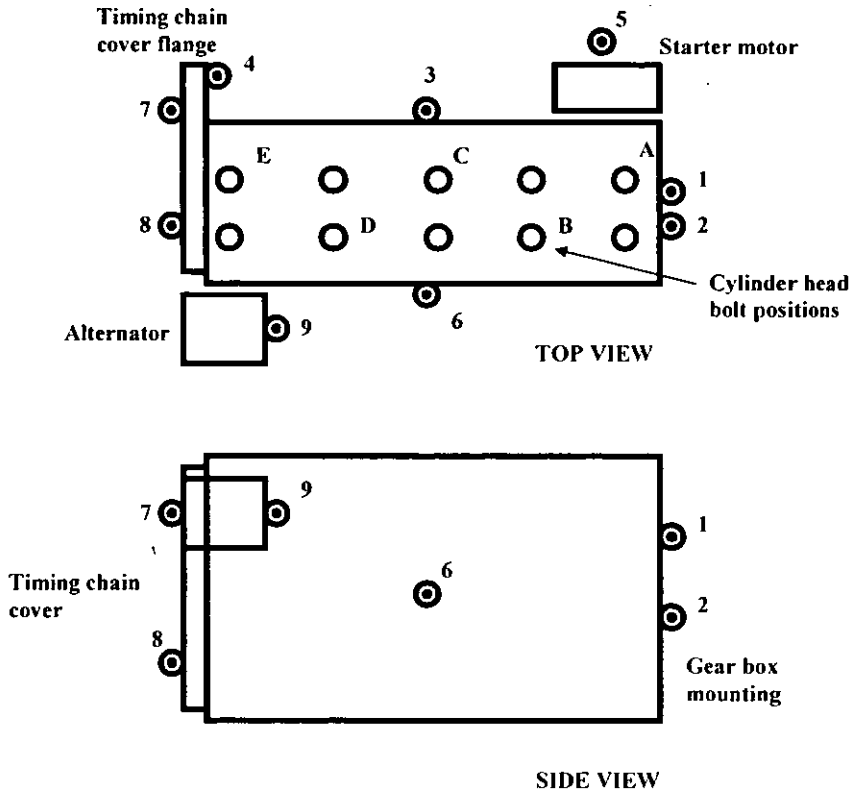

Fig. 5.13: Measurement (1-9) and excitation (A-E) points on the engine.

After using the LDV to identify the dominant frequencies of vibration at different points of interest on the engine, EPSI was used to perform area measurements, at discrete frequencies, about the locations showing the largest movements. The OOP deformation ESPI system featured in Fig. 5.10 was used in stroboscopic mode, allowing the motion to be captured at any instant in time. A Coherent DPSS 532 nm laser was used as the illumination source, with an AOD (AA Electro Optique) to strobe the laser beam at the vibration frequency. Carrier fringes were introduced by manually translating the object beam lens to induce a phase gradient in the object beam.

Results

The major area of undesirable vibration on the engine was centred on the left-hand side of the timing chain cover, shown in Fig. 5.14 (top). The shaker was driven with a sinusoidal signal of frequency 2.78 kHz, corresponding to the major peak in the LDV plot of Fig. 5.12. The resultant ESPI vibrational deformation fringes are shown in Fig. 5.14 (bottom) at one extrema of the deformation.

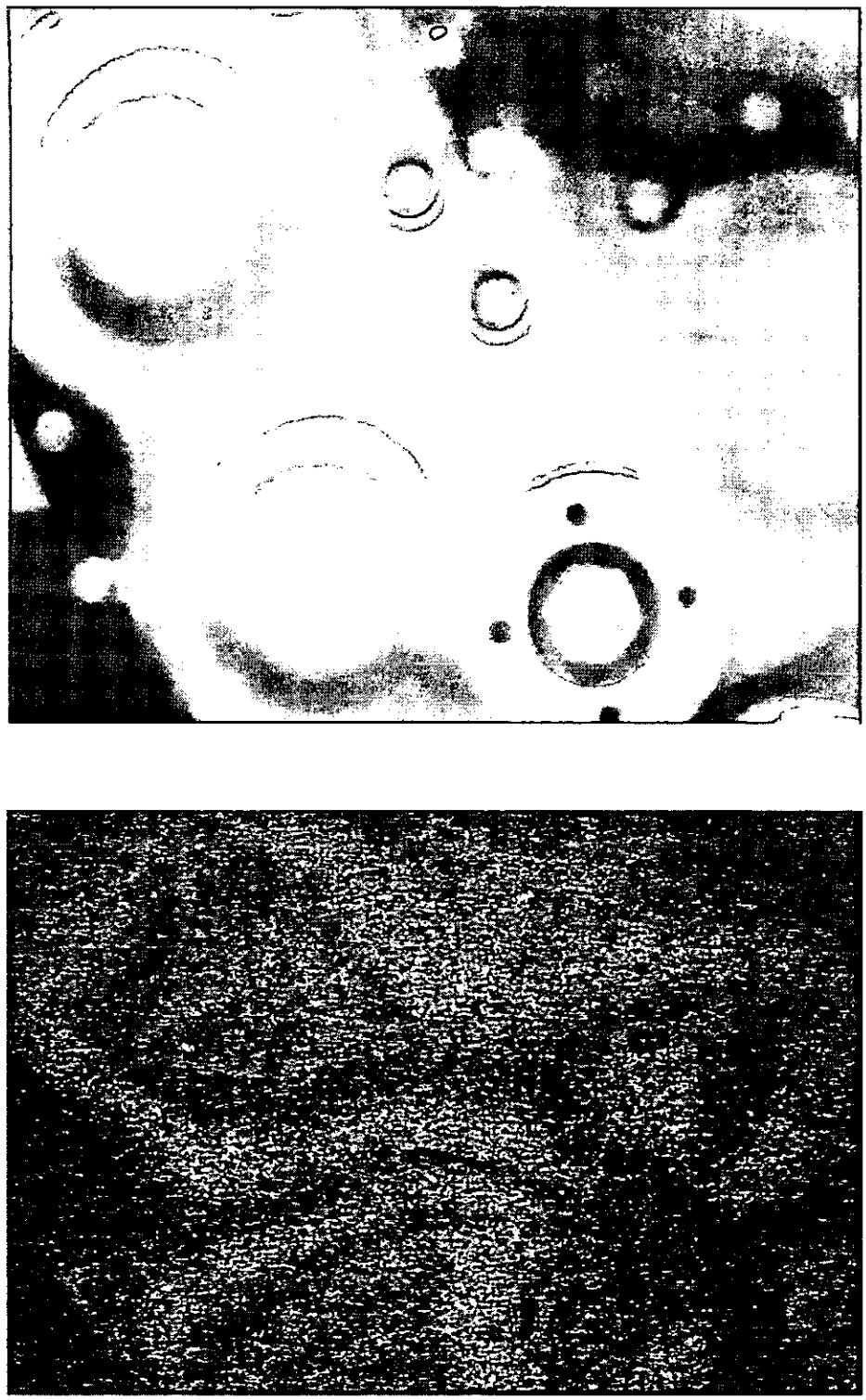

Fig. 5.14: Timing chain cover (intensity image) (top); Deformation interferogram at 2.78 kHz (bottom).

The same deformation combined with carrier fringes is shown Fig. 5.15. The deformation phase was extracted from Fig. 5.15 using the FTM of Section 3.3.2. The object relief was measured using the method described in Section 2.3, and the phase of relief extracted, again using the FTM. A 3D surface relief map of the timing chain cover is shown in Fig. 5.16, with width 180 mm and peak-to-valley relief of 27 mm.

Fig. 5.15: Deformation plus carrier interferogram at 2.78 kHz.

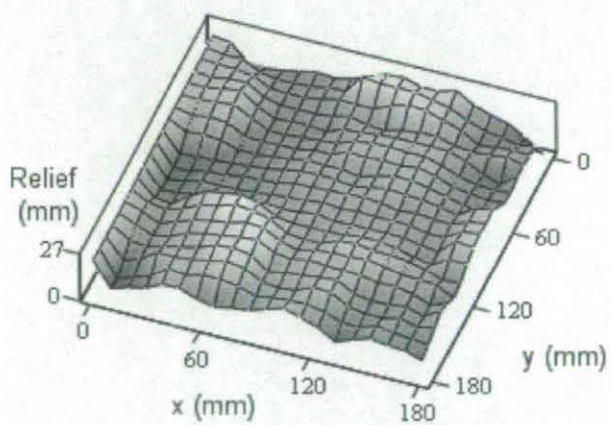

Fig. 5.16: Surface relief of timing chain cover.

The 3D sensitivity correction map for the engine data is shown in Fig. 5.17. This represents the sensitivity factor by which the deformation phase is multiplied in order to calculate the deformation. The sensitivity-corrected vibrational deformation is shown in Fig. 5.18 (top), with a width of 180 mm, and showing a peak-to-valley deformation of 680 nm.

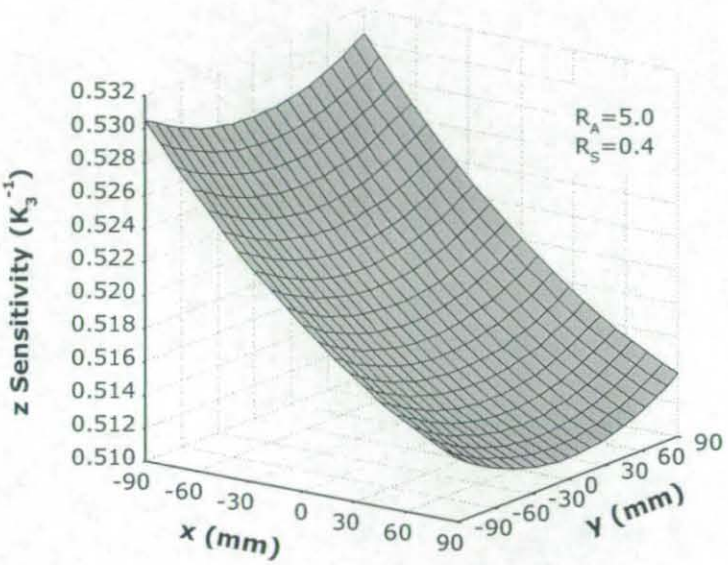

Fig. 5.17: 3D sensitivity correction map for engine measurement.

Based on information from the LDV and ESPI measurements, the engine manufacturer modified the design of the timing chain cover to incorporate stiffening ribs. Prototype ribbing is seen welded to the timing chain cover in Fig. 5.11, compared with the original cover in Fig. 5.14 (top). Repeating the ESPI measurements on the modified timing chain cover, with the same input conditions for the magnetic shaker, revealed a peak-to-valley deformation of 422 nm, which is plotted in Fig. 5.18 (bottom). This represents a reduction of 38% in the vibration amplitude.

It should be noted that controlled experimentation of this nature with levels of excitation less than operational levels can lead to possible inadequate understanding of true engine behaviour at normal operating amplitude levels. Consequently, the manufacturer obtained engine test-bed data, which confirmed that the modifications had reduced the noise of the engine to more acceptable levels.[155]

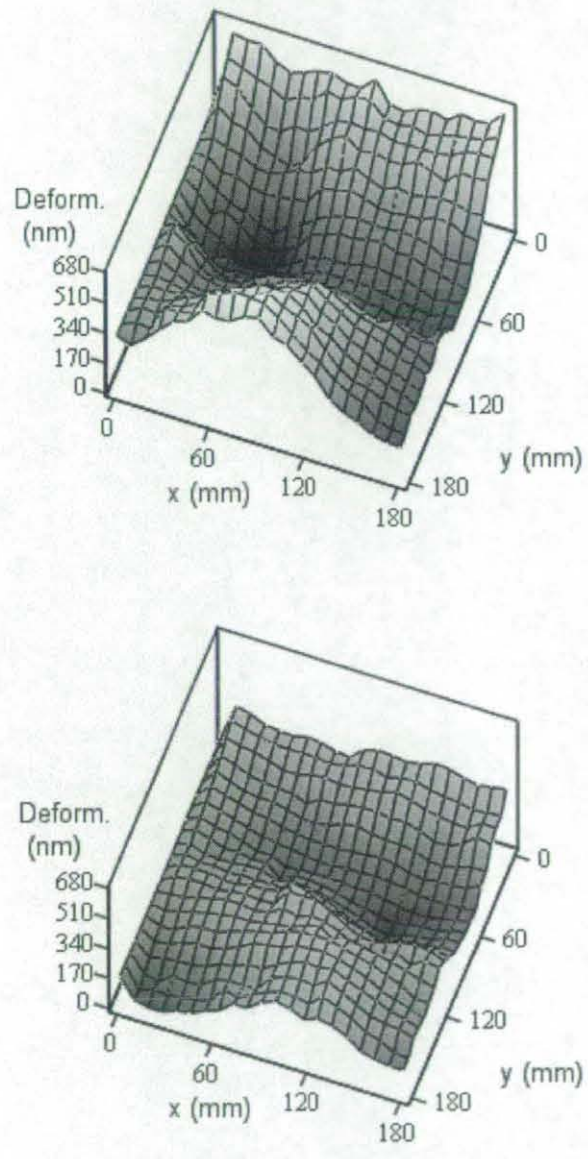

Fig. 5.18: Deformation of timing chain cover; unmodified (top) and modified (stiffened) (bottom).

5.2 TRANSIENT VIBRATIONS

Transient vibration of an object is characterised by temporary aperiodic and/or damped deformation. The aperiodicity precludes the use of a stroboscopic system, where periodicity is essential to ensure that each illumination pulse occurs at the same point in the object's deformation cycle to prevent 'smearing' of the interference fringes. For this reason it is necessary to acquire transient deformations using a single interferogram. This usually requires a pulsed laser in order to deliver sufficient light to the object in the short time intervals during deformation, typically in the order of 100 ns to 1 ms. Although transient deformations are aperiodic, they are repeatable if the driving stimulus is repeatable and the object and environment are invariant. This fact allows particular measurements to be repeated multiple times while aligning the measurement system and when capturing data.

As a result of the short time intervals, two speckle interferograms usually cannot be recorded in separate TV frames of a CCD camera. Thus the interferograms are incoherently added on the CCD, generating addition fringes. A state diagram of the process is shown in Fig. 5.19.

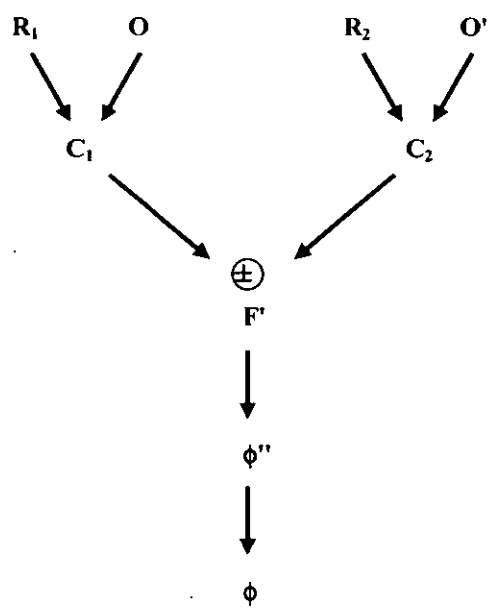

Fig. 5.19: State diagram for generation of ESPI deformation-modulated carrier fringes from transiently-vibrating objects. R: reference wave (1 & 2 – different tilts, for carrier fringes); O: object wave before deformation; O': object wave after deformation; C: correlated speckle (primary interferograms); F': correlation fringes (secondary interferogram); ϕ'': carrier + object phase; ϕ: object (deformation) phase.

5.2.1 Metal Plate

A dual-pulsed laser, as described in Section 3.2.4, and a galvanometer, as described in Section 3.2.2, are used for a set of experiments involving the application of real-time carrier fringes to the measurement of transient deformations of a metal plate.

Experimental Configuration

With reference to the experimental setup of Fig. 5.20, the frequency-doubled light (532 nm) from the laser is divided into an object beam I_o and a reference beam I_r by a variable beamsplitter. This allows the fringe visibility to be optimised by varying the I_r/I_o ratio.[50] Fringe visibility in addition ESPI is very low at best, so its optimisation is important. The laser, a Spectron SL800 (see Fig. 3.4), delivers pulses of ~10 ns temporal width and maximum energy of ~75 mJ per pulse. Approximately 10 mJ per pulse was used for the experiments here. The laser consists of two cavities, allowing two pulses to be generated in quick succession, for capturing two deformation states of the object. The two cavities are mutually seeded by a diode laser for mutual coherence, to prevent decorrelation and preserve fringe visibility.[16] Before collimation, the reference beam passes through a spatial filter to improve spatial uniformity and hence fringe visibility.[50] After reflection from a mirror mounted on a

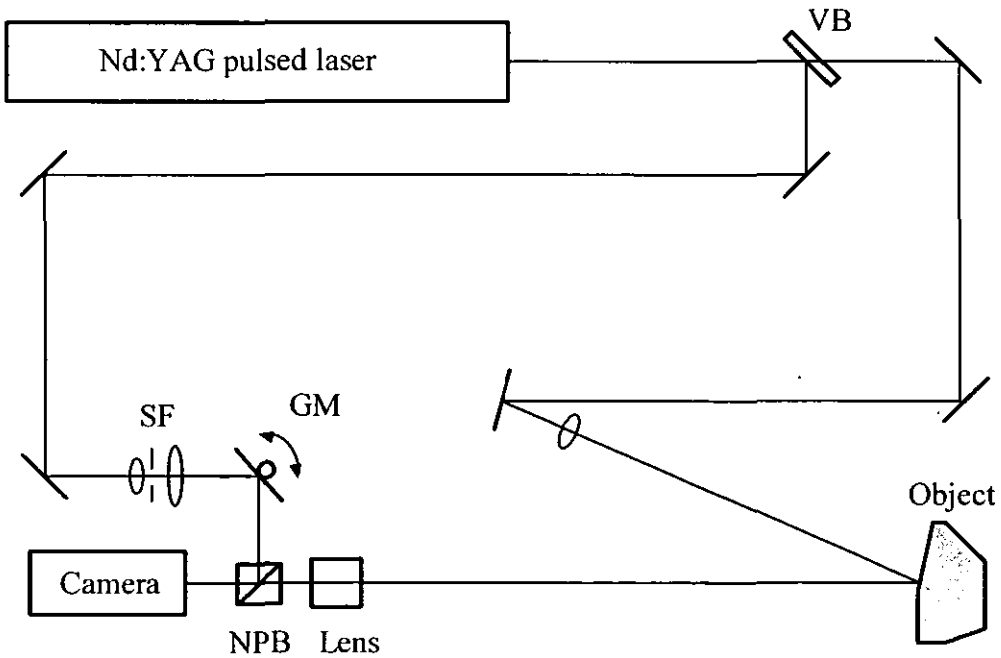

Fig. 5.20: Diagram of dual-pulse real-time carrier system. VB: variable beamsplitter; SF: spatial filter; GM: galvanometer mirror; NPB: nonpolarising beamsplitter.

galvanometer (GM), the beam enters the CCD field-transfer camera (Pulnix TM500) via a nonpolarising beamsplitter. Note that a frame-transfer camera could also be used.

The galvanometer is used to tilt the reference beam to produce a linear phase term and hence carrier fringes in the interferogram. It rotates through a small angle θ (maximum 5°) that depends upon the voltage applied to it. A rotation of θ produces a tilt of 2θ in the reflected beam, independent of the angle of incidence, with the number of carrier fringes proportional to θ (for small θ). Tilting the beam in the reference arm also translates it, but this is not of concern since the wavefront is planar and spatially filtered, and is close to the camera so that beam 'walk-off' is small.

The object beam is expanded and used to illuminate the object at a narrow angle (5.7°) for low sensitivity to in-plane deformation. The object distance was 1500 mm. The light scattered from the object is imaged by the lens onto the camera array, where it combines with the reference beam to form a primary interferogram I_1. After the second laser pulse, a second primary interferogram I_2 incoherently adds on the CCD with the first to produce a secondary interferogram I_A, which contains the deformation fringes.

The timing configuration is shown in Fig. 5.21. The TV camera running at 50 Hz is used as the master timing source. The camera's frame signal is isolated by means of a frame synchronisation (FS) device (the FS can also enhance the contrast of the video

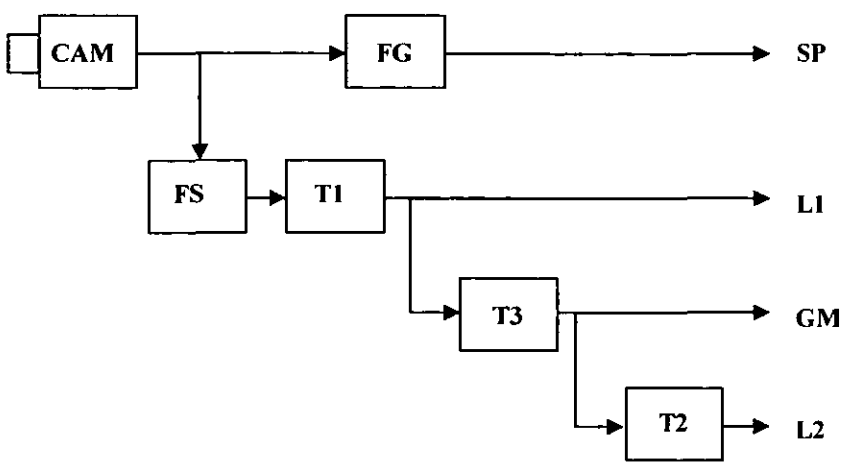

Fig. 5.21: Timing configuration for galvanometer mirror system; T1,2,3: time delays; L1,2: laser triggers; GM: galvanometer trigger; SP: speaker trigger (acoustic impulse to initiate object deformation); CAM: video camera; FS: frame synchronisation; FG: frame grabber.

signal, which worked well with subtraction fringes, but behaved erratically with the very-low contrast of addition fringes). The FS drives the laser flash lamps, as well as a pulse generator. The pulse generator fires the first laser cavity (L1) as well as a second pulse generator, the output of which fires the second laser (L2). The first pulse generator also drives the galvanometer mirror (GM), which is tilted between the two pulses. In this manner, the laser pulses can be positioned anywhere within the 20 ms field time of the camera. This arrangement also allows the laser to run continuously, thus avoiding thermal-lensing effects and loss of seeding.[48] Fig. 5.22 shows the sequence of events during a measurement.

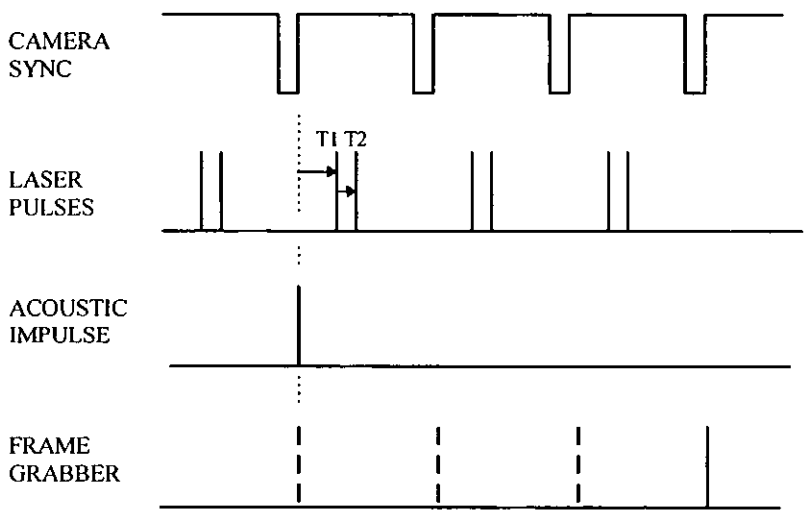

Fig. 5.22: Timing diagram for galvanometer mirror system.

To synchronise to the object's movement, the frame grabber (FG), after being armed by the user, waits for the start of a camera field and then triggers a loudspeaker (SP) directed at the object, providing the acoustical stimulus to initiate the object deformation. The frame grabber then waits for a user-specified number of fields before grabbing an image. This allows different intervals of the deformation to be captured reliably. The images were acquired at 512 × 512 × 8-bit resolution.

The frequency response of galvanometers is usually limited to the low-kilohertz region (as discussed in Chapter 3), making them suitable for slow transients. For medium-speed events, a PT could be used to tilt the mirror. PT's can have frequency responses in the region of tens-of-kilohertz, offering an order-of-magnitude improvement. For

faster events, an acousto-optic device could be used (Section 3.2.8), or a continuously-rotating mirror could be employed, the short laser pulses (10 ns) effectively freezing its motion. In this case the rotating mirror would be the master timing source instead of the camera, as illustrated in Fig. 5.23 and the associated timing diagram of Fig. 5.24. For a time interval of 2 μs, the mirror would need to rotate at approximately 7000 rev/min, which is readily achievable with small motors.

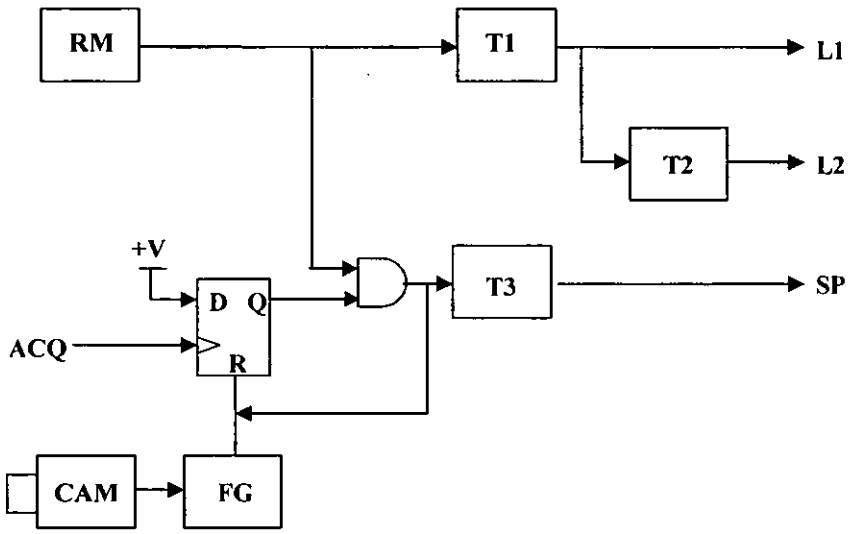

Fig. 5.23: Timing configuration for rotating mirror system; T1,2,3: time delays; L1,2: laser triggers; SP: speaker trigger (acoustic impulse to initiate object deformation); ACQ: start acquisition trigger, driving D-type flip-flop; CAM: video camera; FG: frame grabber.

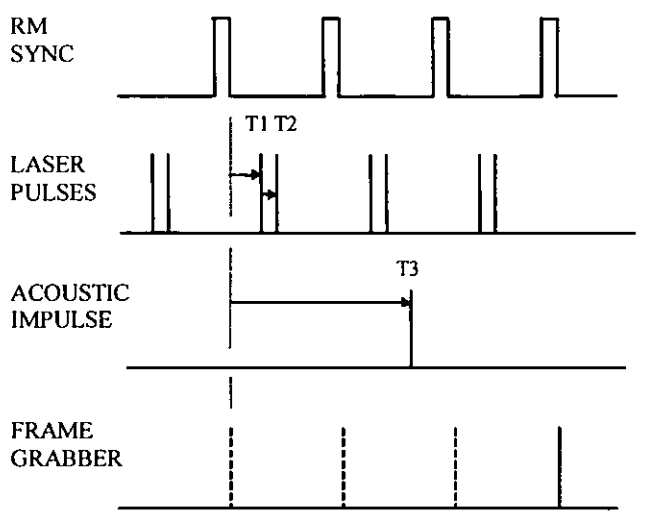

Fig. 5.24: Timing diagram for rotating mirror system.

Results and Discussion

The system described above was used to study the deformation of a thin plate under the influence of an acoustic shock. The plate was 1 mm thick stainless steel, 150 mm square, clamped around its edge by 20 mm square steel bars. The acoustical stimulus was provided by a 150 mm diameter loudspeaker, 30 mm from the plate and directed towards the centre of the plate.

To begin, the system was used without carrier fringes to study the nature of the deformation of the plate. With the frame grabber synchronised to the stimulus, an addition interferogram was acquired at time t_1 after the commencement of the stimulus at t_0, using the laser in dual-pulse mode with 2.5 ms pulse separation. This is shown in Fig. 5.25 (left), where the low contrast makes the fringes practically invisible, and substantial variations in irradiance are evident across the object. The result after enhancement by the novel absolute-deviation filter of Eq. (3.26) using a 3×3 window is shown in Fig. 5.25 (right). Here the fringe visibility is substantially improved, approaching that of subtraction fringes, and the uniformity of irradiance is markedly enhanced. Larger windows of 5×5 and 7×7 improved the visibility slightly, but at the expense of spatial resolution. It is apparent from Fig. 5.25 (right) that the plate is vibrating in its fundamental mode. This was verified by the use of a LDV (Polytec, Model 302), which also revealed a period of oscillation of approximately 4 ms.

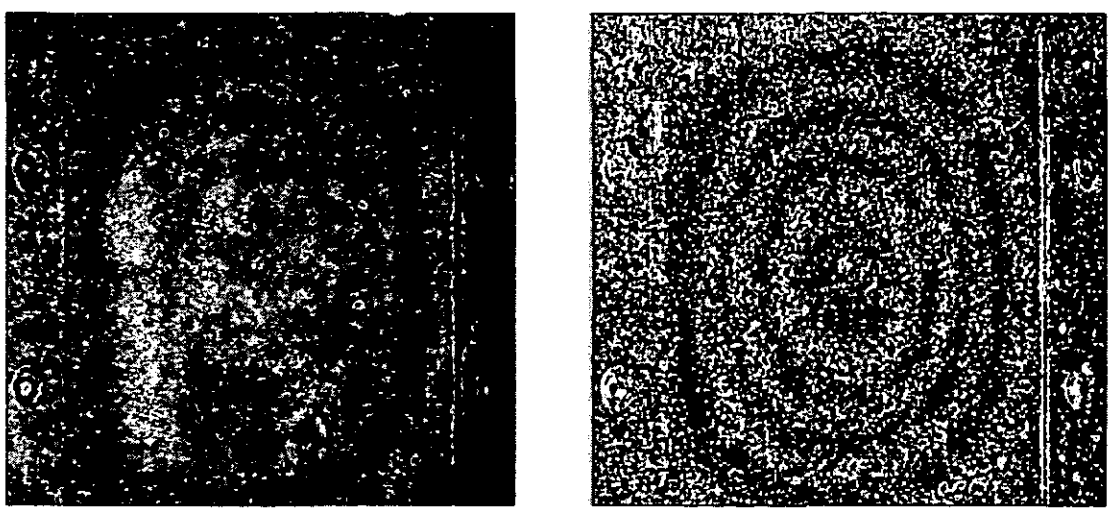

Fig. 5.25: Pulsed addition fringes of metal plate showing OOP deformation due to acoustic impulse; unfiltered (left) and filtered (right).

Several ESPI measurements at the same time t_1 qualitatively showed very good repeatability. Also evident from Fig. 5.25 (right) is the disadvantage of this type of noncarrier measurement—the phase (sign) of the deformation is not resolved.

To resolve the phase ambiguity, carrier fringes were then introduced. The carrier measurements were performed by use of addition with the laser in dual-pulse mode. The carrier was introduced by rotating the galvanometer mirror during the interval t_S between the two laser pulses, that is between t_1 and $t_2 = t_1 + t_S$. A measurement with a continuous light source and photodetector showed a mirror response time of approximately 500 μs. It was found that the number of carrier fringes could be easily varied between zero and more than 50 by changing the drive voltage.

The galvanometer was set to give approximately 15 fringes across the field of view, equating to a rotation of 1.5 mrad. The separation of the laser pulses was set to 2.5 ms, with the galvanometer triggered straight after the first pulse, to allow the mirror time to settle before arrival of the second pulse. With the same conditions as before, a deformation-modulated carrier image was acquired. The measurements were repeated, increasing the time delay $t_d = t_1 - t_0$ each time, to build a picture of the deformation. The enhanced interferograms of Fig. 5.26 show the deformation decaying with increasing delay times.

From one of the enhanced images, Fig. 5.26 (top-left), the deformation was calculated using the Fourier technique described in Section 3.3.2. Fig. 5.27 (top-left) shows the Fourier transform, where the deformation-modulated carrier terms, the zero-order term and the speckle halo can be easily discerned.

The width of the bandpass filter mask in the Fourier domain is critical for good results. The filter should be broad so as to preserve as much of the deformation term as possible, but not broad enough to include significant portions of other major terms in the frequency plane.[81] Also, the carrier frequency should be sufficiently high such that the deformation term does not overlap the zero-order term.[66] If these conditions are not met, then inconsistencies are likely to appear in the phase map.

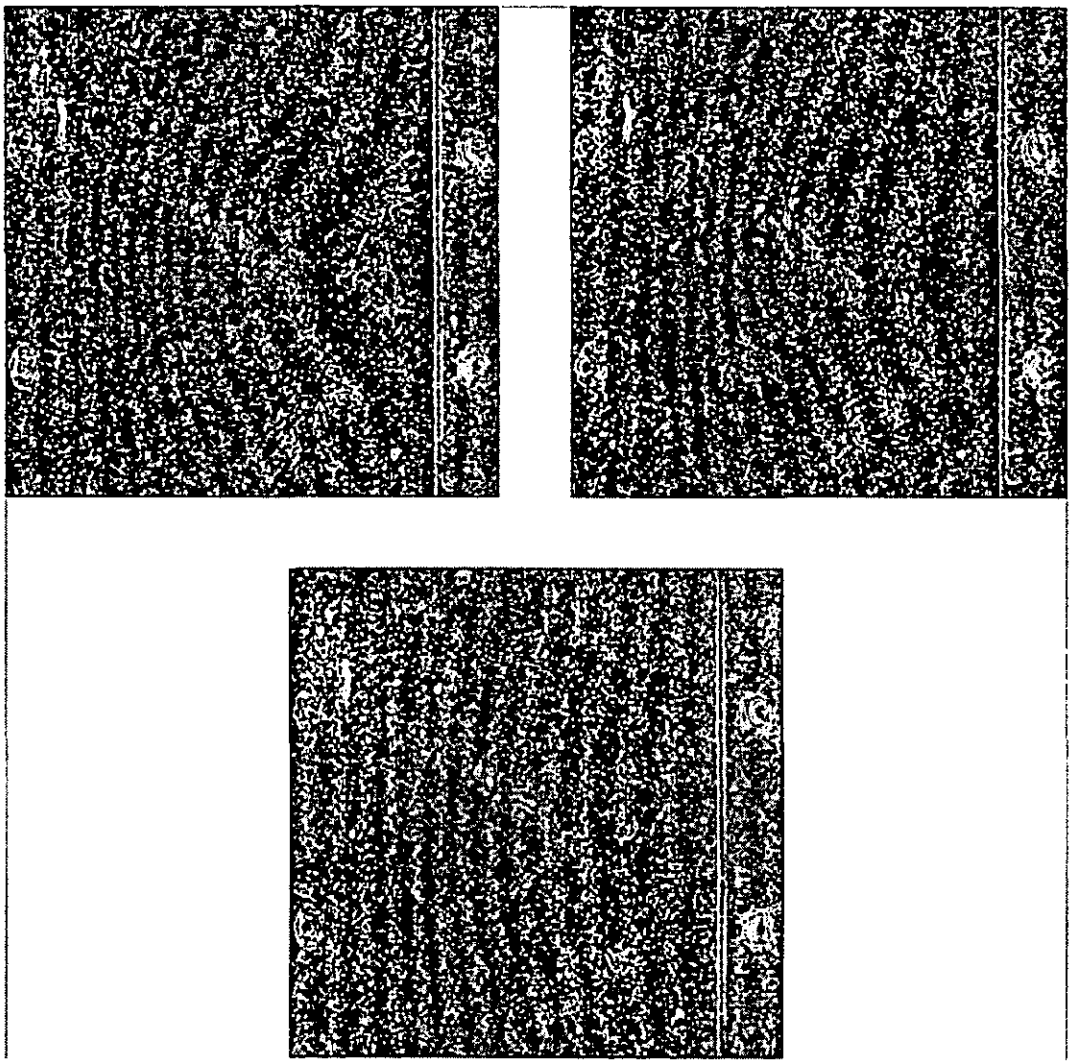

Fig. 5.26: Pulsed addition deformation-modulated carrier fringes of metal plate showing OOP deformation due to acoustic impulse; (clockwise from top-left) increasing delay times after initiation of the impulse.

From the phase calculated by means of the FTM, it is seen from Fig. 5.27 (top-right) that the FTM, with judicious use of mask, also acts as a filter that removes almost all of the speckle noise, thus obviating the need to apply a separate noise-reduction filter. In this instance a binary filter mask of 11-pixel radius was used.

The wrapped phase of Fig. 5.27 (top-right) is then made continuous using the iterative least-squares unwrapping algorithm of Section 3.3.4. The weighting matrix used in conditioning the algorithm is shown in Fig. 5.27 (bottom-left), where black indicates zero weighting and grey is unity weighting. This matrix is derived from the

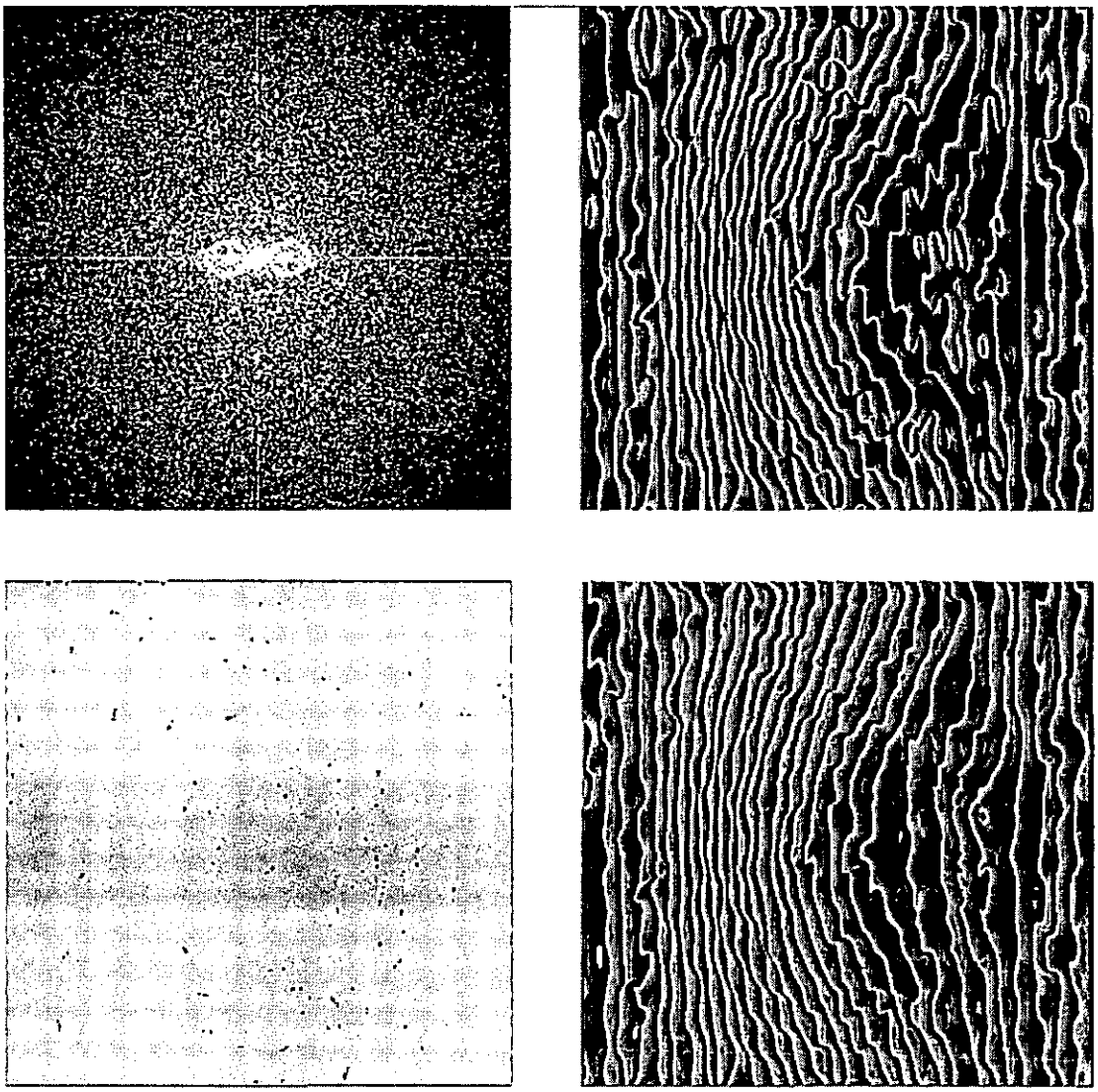

Fig. 5.27: Processing of ESPI carrier fringes; Top-left: Fourier transform of deformation fringes of Fig. 5.26 (top-left); Top-right: wrapped phase map of deformation, calculated by FTM; Bottom-left: phase inconsistency map, calculated from wrapped phase; Bottom-right: rewrapped phase map of LS-unwrapped deformation phase map, showing improvement over original wrapped phase (top-right).

inconsistencies in Fig. 5.27 (top-right). The number of inconsistencies[156] around a closed path is defined by

$$n = \sum_{i=1} \left\{ \frac{\phi(i) - \phi(i-1)}{2\pi} \right\} \tag{5.2}$$

where $\phi(i)$ are the modulo-2π wrapped phase values at adjacent points along a closed path, and the braces $\{\ldots\}$ indicate rounding to the nearest integer. Thus the individual differences inside the braces will take on values of either 0, +1, or −1, where the

nonzero values signify either a modulo-2π phase wrap, or an inconsistency due to noise or object features. This process is equivalent to locally unwrapping the phase map along a closed path. By unwrapping around a square of 2×2 pixels, then if that part of the phase map is consistent, the unwrapped phase gradient is less than π and n will be zero. If there are inconsistencies, then $n = \pm 1$. These inconsistencies, or phase residues, are the ones shown in Fig. 5.27 (bottom-left), as the zero-weighted (black) pixels.

The final unwrapped phase map after ten iterations shown in Fig. 5.27 (bottom-right). This has been rewrapped by applying a carrier of similar frequency to Fig. 5.27 (top-right) to better show the effects near the inconsistencies. In comparison, Fig. 5.27 (bottom-right) is more regular and has none of the phase inconsistencies of the original wrapped data.

The unwrapping algorithm was applied a number of times using an increasing number of iterations, from zero to twenty. The convergence of the algorithm is shown in

Fig. 5.28. The vertical axis is the rms difference between each consecutive pair of iterations and is expressed as a percentage of the 8-bit quantisation of the data. No significant improvement is noted beyond around 15 iterations, for this image.

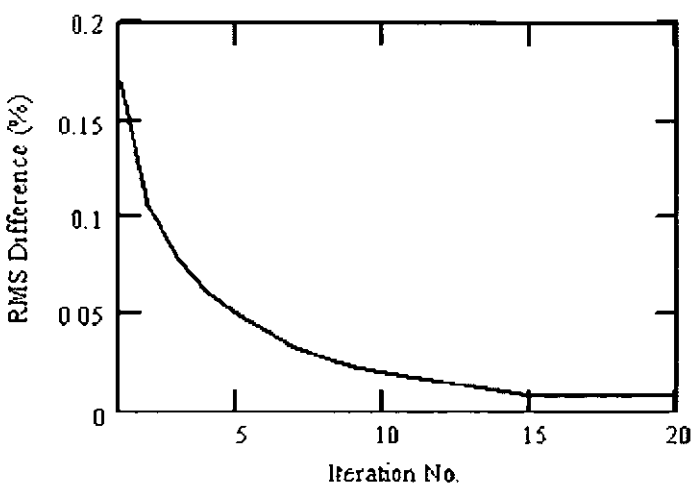

Fig. 5.28: Convergence of the LS-unwrapping algorithm; rms difference of unwrapped phase between consecutive pairs of iterations, expressed as a percentage of the 8-bit quantisation of the data.

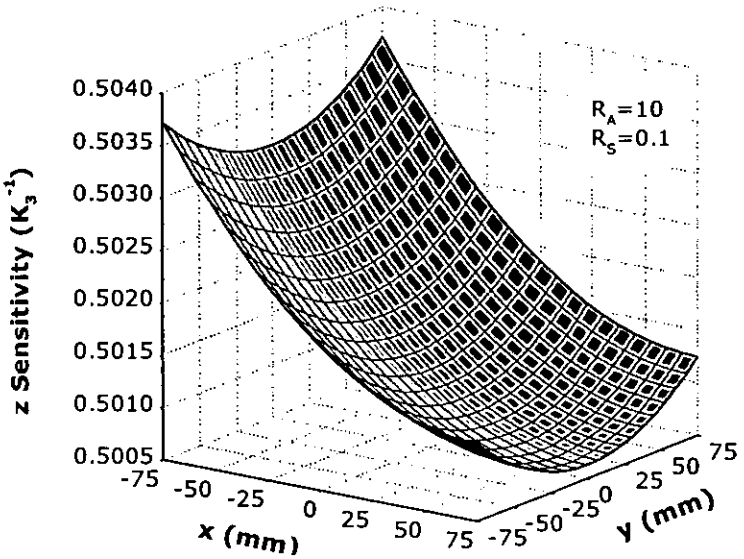

Fig. 5.29: 3D sensitivity correction map for metal plate.

The 3D sensitivity correction map for the plate deformation is shown in Fig. 5.29. This represents the sensitivity factor by which the deformation phase is multiplied in order to calculate the deformation.

The linear phase term was removed from the deformation phase using a linear least-squares fit, after which the sensitivity correction of Fig. 5.29 was applied, producing the final deformation map illustrated in Fig. 5.30. The maximum deformation of the object in this image is 0.82 μm.

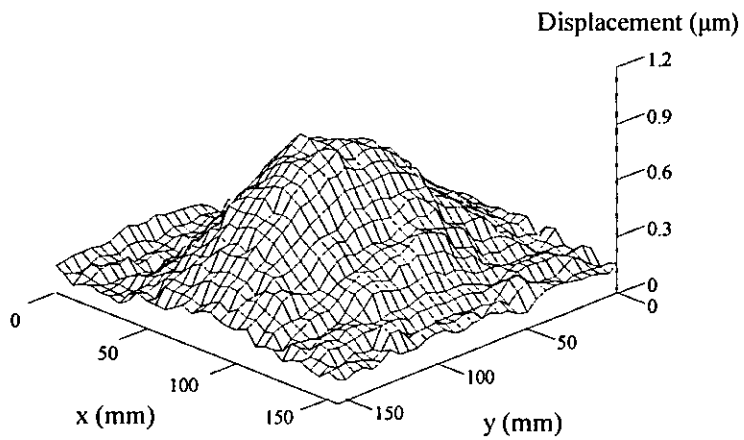

Fig. 5.30: .Deformation map with carrier frequency removed.

Finally, the calculation of derivative (deformation slope) data from the deformation data is demonstrated using the Fourier derivative theorem (FDT) of Section 3.3.3 and Appendix B. An x-profile through the centre of the deformation map is shown in Fig. 5.31 (dotted trace), where it can be seen that the original data has a small amount of noise present. While in the frequency domain for the FDT, a mask of radius $u_r = 6$ was applied to illustrate the noise filtering that can be achieved, to wit the smooth curve of Fig. 5.31 (solid trace).

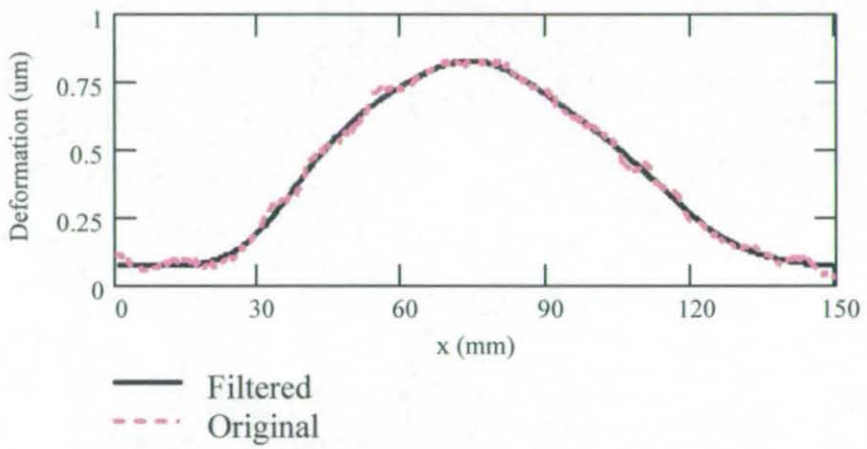

Fig. 5.31: Profile through centre of deformation map; Original (dotted trace); Fourier filtered (solid trace).

Proceeding then with derivative filter of Eq. (3.34), the slope data is calculated from the deformation data and plotted in Fig. 5.32. This is equivalent to the out-of-plane surface rotation about the y-axis, $\omega_y = \partial w / \partial x$, assuming the in-plane deformation ∂u is small. The derivative shows a maximum slope of $\omega_y = 21$ μradians, plus very good noise rejection, signifying the efficacy of the FDT.

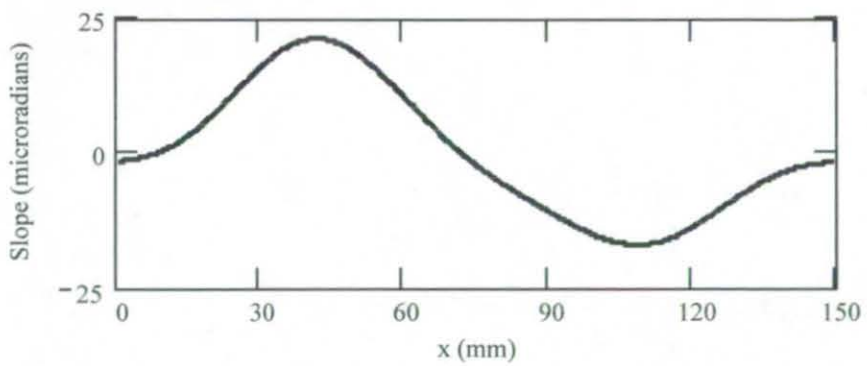

Fig. 5.32: Surface slope profile through centre of object, as calculated by FDT.

5.3 SUMMARY

This chapter has demonstrated the practical and successful application of many of the unique techniques and algorithms that were developed in the preceding chapters. ESPI systems were implemented for both harmonic and transient vibration measurement. These systems were also used to measure the relief of objects. The relief data was then combined with the system geometry to correct the deformation sensitivities in an effort to produce more accurate data.

Among the harmonically vibrating objects, a cylinder (regular shape) and an internal combustion engine (irregular shape) were measured. Stroboscopic ESPI was used, where the laser was pulsed by an AOD. The AOD was synchronised to the object vibration, which was driven by electro-magnetic shakers. Carrier fringes were introduced for both deformation and shape measurement.

For the transient deformation tests, a flat plate was studied, which was driven by an acoustic impulse. Addition fringes were used in this case due to the speed of acquisition. A novel enhancement algorithm produced fringes with quality approaching that of subtractive fringes.

For both types of vibration measurement, carrier fringes were formed by means of a galvanometer mirror, offering stable and repeatable fringes. The carrier fringes were processed using the FTM and a least-squares phase unwrapper, yielding quantitative deformation and slope data from single fringe maps.

6 Conclusions

This research has investigated the combination of shape and deformation measurement for improving the accuracy, speed and utility of ESPI. The objectives have been to advance the understanding of the nature of sensitivity variations within different types of interferometer and with different shapes of object, and then to develop novel carrier fringe schemes and use these to effect the measurement of deformation and shape, where the latter is used to correct the sensitivity variations of the former. The outcomes of this work include:

- Novel methods for generating carrier fringes
- A new algorithm for enhancing fringe visibility
- Unique combination of Fourier methods for simultaneous deformation and strain calculation, including apodisation filter
- A novel and exhaustive model of interferometer sensitivity variations
- Experimental verification of the above techniques

On the subject of sensitivity variations, examination of the conventional, or 'primary', models of deformation measurement established that they adequately describe the sensitivity of interferometers with collimated illumination, based on the angles of illumination and observation. However, such models are insufficient when using noncollimated illumination, because of the directional variation of the sensitivity vector across the surface of, and with the relief of, the object. Proceeding then, with a comprehensive 3D deconstruction of the systematic sensitivity variations ('secondary' and 'tertiary') for both IP and OOP interferometers, sensitivity equations were derived, along with error functions for the components of object displacement. Then, a novel,

scalable approach to system parameters was developed to make the models generic and consequently applicable to a broad range of geometries.

Plots of the error functions revealed that the 'secondary', or auto-sensitivity, variations can be considerable for many practical systems. In particular, substantial errors are observed for large object dimensions or small object distances. Additionally, errors increase when the sources move on-axis for IP systems and off-axis for OOP systems, the latter also showing increasing asymmetry across an object's surface.

Analysis of the 'tertiary', or cross-sensitivity, terms showed that these sensitivities are sometimes higher than the 'secondary' sensitivities, making noncollimated interferometers particularly susceptible to errors from the two orthogonal components of object displacement. Such cross-sensitivities also manifest themselves in some collimated interferometers, i.e. OOP interferometers are sensitive to the IP components of displacement that are parallel to the plane of incidence.

It was found that as the relief of an object increases, the sensitivity errors almost invariably increase. This is not overly unexpected, as it is akin to reducing the object distance. However, the errors also depend on the relief distribution of the object, and as such are difficult to generalise. Nonetheless, the error magnitudes are usually small when the relief variations are small compared with the object distance.

It is envisaged that the above results will lead to a better understanding of the nature and magnitude of sensitivity variations, allowing errors to be identified and then corrected numerically, or for errors to be minimised through improved interferometer designs.

A review of phase measurement techniques found that carrier fringes and the Fourier-transform method are a preferred method for phase modulation and demodulation when a system is restricted to the capture of a single interferogram. Such restrictions can occur due to noisy environments, or for the capture of transient deformations.

For producing dynamic carriers, several novel techniques were designed and analysed. For low-to-medium speed events, an electro-mechanical device such as a galvanometer

mirror, or an electro-optical modulator such as a wedged liquid crystal device allow repeatable generation of carrier fringes using simple configurations—something that is valuable in terms of ease of setup and alignment, and also in terms of preserving the beam quality.

For capturing high-speed events using carriers, acousto-optic modulators offer several options. The inherent, unwanted temporal phase modulation of these devices was surmounted by two novel schemes: firstly using two modulators with even-odd first-order beam asymmetry; secondly using a single first-order beam combined with countertilts (which also cancel the phase modulation). The theory presented herein opens-up the use of acousto-optic modulators for a wide range of coherent optical applications, where high-speed, repeatable carrier-frequency modulation, beam tilting, or phase shifting is required.

The demodulation of carrier fringes from single interferograms can be problematic due to the low visibility and high noise level of the resultant addition fringes. Several processes were combined to surmount this. Firstly a novel, linear visibility-enhancement algorithm was proposed to substantially increase the visibility, to a level approaching that of subtractive fringes, while at the same time improving spatial uniformity. Secondly, the speckle noise was mitigated by narrow-bandpass filtering in the Fourier domain during the application of the Fourier-transform method of phase demodulation. Finally, an iterative phase-unwrapping algorithm was employed, with the incorporation of a weighting mask that removes inconsistent data from the solution.

As an adjunct to the carrier fringe techniques, the Fourier-transform method was adapted in a novel manner to furnish simultaneous deformation and derivative data, directly from the carrier fringes. The method was demonstrated for differentiation and integration, using both theoretical and experimental data. This method also has applications beyond interferometry—it can be used to differentiate or integrate a variety of data.

For experimental confirmation of the phase measurement and sensitivity correction theory presented herein, the techniques were combined in a series of experiments to demonstrate their validity and efficacy.

To begin, harmonically-vibrating objects were measured. As a form of deterministic object, a cylindrical tube was measured, using a stroboscopic system comprising an acousto-optic deflector for strobing and a galvanometer mirror for carrier fringe generation. Here the relief data was utilised to correct the raw deformation data, to furnish the true out-of-plane deformation with respect to the surface normal.

An irregularly-shaped object—an internal combustion engine—was then measured, as an example of a practical vibration-minimisation problem. A laser Doppler velocimeter formed a high-speed point-measurement probe to rapidly identify the vibration spectra at various locations on the engine. The stroboscopic ESPI system was then used to quantify the amplitude and mode shape of the resonances. Based on the velocimeter and ESPI results, the engine manufacturer effected modifications to the design of the timing chain cover to stiffen it. After repeating the measurements using the same conditions, the vibration amplitude had reduced by nearly 40%. Subsequent tests by the manufacturer confirmed that the noise had indeed reduced, to a more acceptable level.

Finally a transiently-vibrating object was measured. An additive ESPI system using a dual-pulsed laser was used to successfully measure out-of-plane deformation and the derivative of deformation in a metal plate driven with an impulse, with results close in quality to a subtractive system. The introduction of carrier fringes into the measurements by use of a synchronised galvanometer-mounted mirror produced a simple and stable configuration that is suitable for in-field use, can be easily extended to more than one dimension, and can be used for in-plane configurations. The mirror technique helps to preserve the precious quality of addition fringes by introducing a minimal number of optical components into the reference beam path. Combined with an absolute-deviation filter to enhance the visibility of the addition fringes, and a robust iterative weighted least-squares phase unwrapper, quantitative evaluation of both the phase and amplitude of object deformation and slope was achieved. The

galvanometer's response time of 500 μs was adequate for the measurements reported here. For faster events, a continuously-rotating mirror synchronised with the laser pulses, or an acousto-optic modulator, could be used for tilting the reference wavefront.

6.1 FURTHER WORK

Aligned with the work in this thesis, there are several areas that may benefit from further investigation.

One of these is the acousto-optical deflector schemes of Section 3.2.8 for producing carrier fringes and phase shifting. The experiments reported herein were of a proof-of-principle nature. Further experiments could be conducted, on dynamically deforming objects, to demonstrate the fast nature of the schemes. For example, rapid measurement of large deformations by means of temporal phase unwrapping (Section 3.3.4). Conversely, high-resolution measurement of relief (including discontinuous relief) by the multiple wavelength techniques of Section 2.3.2. Other experiments could also be devised to measure the repeatability, resolution and speed of the schemes.

The liquid crystal device phase modulator of Section 3.2.6 could be fabricated and tested. Such a device would be of value for straightforward generation of carrier fringes, offering a speed somewhere between that of a galvanometer mirror and an acousto-optic device.

In terms of the phase demodulation methods, the Fourier-transform method could be automated to improve its speed and repeatability. Without this, it cannot approach the utility of phase-shifting algorithms that calculate phase without user intervention, and is the major impediment to more widespread use. The main issue is masking of the modulated carrier term in the frequency domain. The modulation can produce moderately complicated shapes, which must be accurately masked to preserve the deformation information while rejecting as much of the surrounding speckle noise as possible. This is essentially an image processing cum mathematical minimisation

problem. Drawing from these fields, techniques such as a Laplacian-of-Gaussian[157] filter, or active contours[158] ('snakes') may prove useful. An iterative approach could be envisaged, whereby a merit factor is optimised with each iteration.

The Fourier derivative/integral method was presented using one-dimensional signals. Preliminary results of two-dimensional calculations reveal that the method is equally powerful, with an added advantage that strains in multiple directions can be easily calculated. As with the Fourier-transform method, the nature of the filtering in the frequency domain is important for minimising noise and aliasing. Investigation of automated filter optimisation techniques would benefit the accuracy of the method, as would further application to measured data, including comparison between the results of optical and numerical strain calculations.

Finally, the interferometer sensitivity-variation models derived herein, although comprehensive, are for only one class of systematic error. There are other systematic errors, plus random errors that should be considered when using interferometry. Additionally, a similar sensitivity analysis could be applied to the study of stain and relief measurement configurations, and the models could be validated against accurate measurement data. It would be instructive to examine these errors in more detail, with a view towards understanding the fundamental accuracy limitations of interferometry.

Appendix A: Fourier Strain Calculation

The Fourier derivative theorem (FDT) can be used to calculate strain or bending moments from deformation data, and vice versa using the Fourier integral theorem (FIT). The theory behind both theorems is presented in Section 3.3.3. In this appendix, simulations of both the FDT and FIT are carried out to demonstrate their practical implementation and accuracy, along with a few subtleties. The simulations were performed using Mathcad software.

The discrete Fourier transform (DFT) is used for the simulations, of the form:

$$F(u) = \frac{1}{N}\sum_{x=0}^{N-1} f(x)\exp(-2\pi iux/N) \tag{A.1}$$

where $f(x)$ is the signal in the spatial domain, u is the spatial frequency in the frequency domain and N is the number of samples in the signal. The inverse DFT is then

$$f(x) = \sum_{u=0}^{N-1} F(u)\exp(2\pi iux/N) \tag{A.2}$$

Note that there is an amplitude scaling asymmetry (N) between the forward and inverse transforms, but they are otherwise orthogonal. The scaling of Eq. (A.1) is such that the amplitude of the zero-frequency term equals the average of the signal:

$$F(0) = \frac{1}{N}\sum_{u=0}^{N-1} f(x) \tag{A.3}$$

A.1 DIFFERENTIATION

To commence, an analytic differentiable function is used to verify the fundamental FDT. A parabolic-amplitude signal of the form:

$$q(x) = a[x-(N-1)/2]^2 + bx + n(x) \tag{A.4}$$

is used, where $x = 0...N-1$ and the parabola is centred about the centre of the x-range. The constant b is a linear gradient and the variable $n(x)$ is an additive noise term. The derivative of this function is a straight line:

$$g(x) = q'(x) = 2a[x-(N-1)] + b + n'(x) \tag{A.5}$$

The parabola is plotted in Fig. A.1 for N=128, a = 0.03, b = 0 and $n(x)$ = 0.

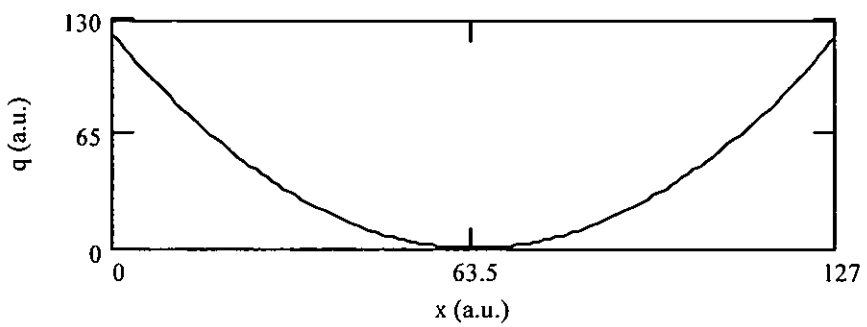

Fig. A.1: Parabolic-amplitude signal in spatial domain.

The magnitude of the frequency domain spectrum is shown in Fig. A.2 (solid trace), along with a window function (dotted trace). The DFT assumes the spatial-domain signal is periodic with an integer number of periods within the aperture. If this is not the case, the apparent discontinuities at the aperture edges give rise to additional spectral components.[159] Window functions are often used with the DFT to reduce the effects of non-periodicity of signals, by multiplying the signal by a window that tapers towards zero at each end.

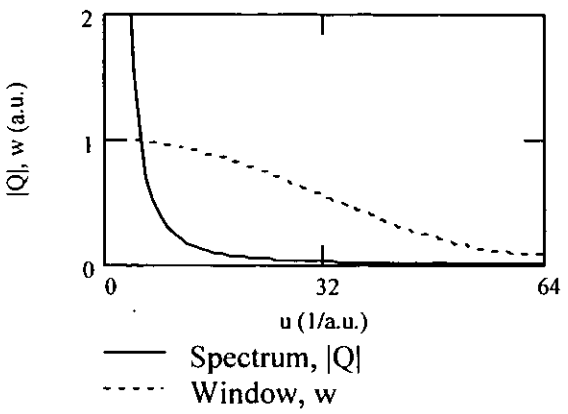

Fig. A.2: Magnitude of frequency spectrum of parabolic signal (solid trace); Amplitude of Hamming window function in frequency domain (dotted trace).

Although windows are usually employed in the spatial domain, when applying the FDT the signal derivative then also contains the derivative of the inverse transform of the window function, making separation difficult. Instead, a window can be applied in the frequency domain, effectively acting as a low-pass filter to remove the higher frequency terms that can cause ringing of the signal. For use in the spatial domain, the Hamming window[159] is a common choice for its narrow frequency bandwidth. Applied in the frequency domain, the Hamming window was found to offer good suppression of noise and ringing effects. The Hamming window is plotted in Fig. A.2 (dotted trace) and is described by (for this case in the frequency domain):

$$w(u) = 0.54 - 0.46\cos\frac{2\pi(u + N/2)}{N} \tag{A.6}$$

The result of applying the FDT (without window) to the parabolic signal is shown in Fig. A.3 as the real component of the derivative signal—a linear function of positive slope, as expected.

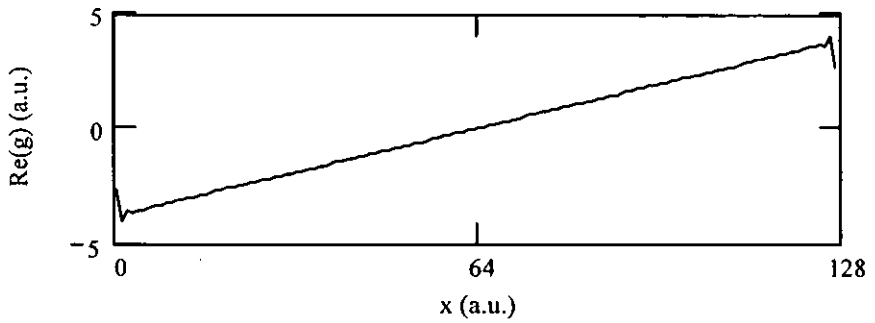

Fig. A.3: Real component of the derivative of parabolic signal, by means of the FDT.

The error difference between the FDT and the analytic derivative is shown in Fig. A.4, both without (top), and with (bottom), frequency-domain Hamming window. Here the values at the edges (x = 0, 127) have been set to zero. Both graphs have small errors, showing a good match to a straight line. The non-windowed case has noticeable ringing at each end, resulting in a standard deviation σ = 0.043, while the windowed case has less ringing, with the standard deviation marginally lower at σ = 0.017. The effect of the window here is relatively minor because the parabola is an even function, thus meeting the periodicity criterion of the FFT.

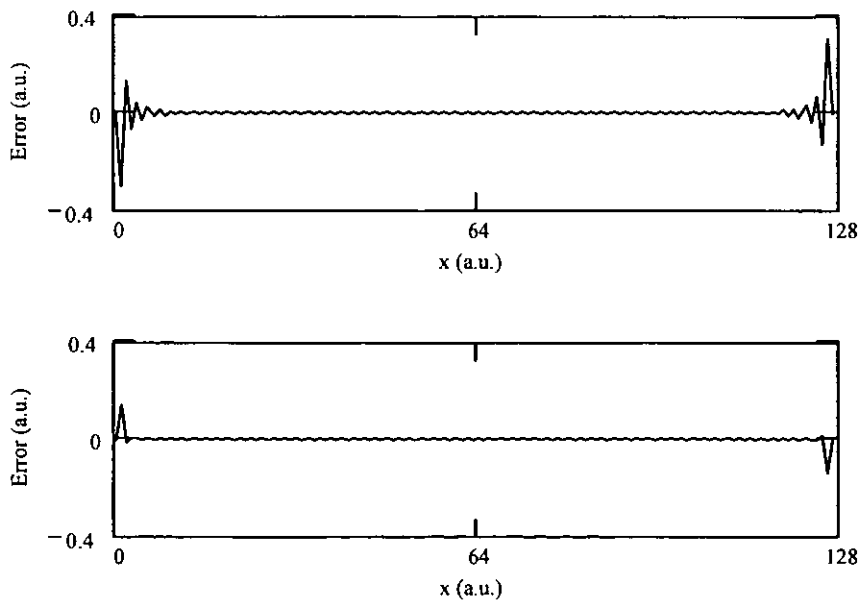

Fig. A.4: Difference (error) between FDT calculation and analytic derivative of parabola; no window (top), Hamming window (bottom).

Now, to violate the periodicity condition of the DFT, a linear gradient is introduced in the spatial domain, using $b = 0.5$. The resulting signal is shown in Fig. A.5.

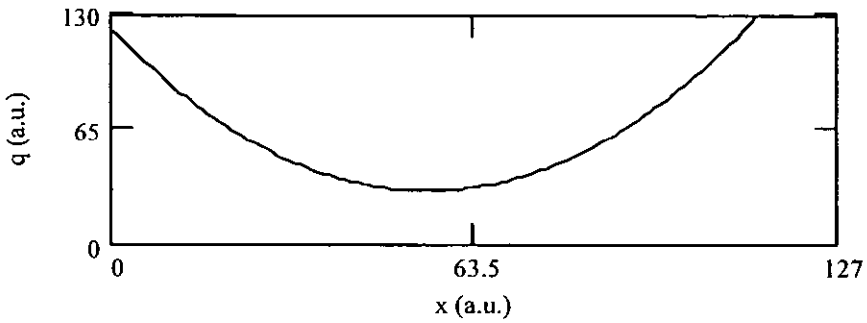

Fig. A.5: Aperiodic parabolic signal (gradient added).

Applying the FDT to the above signal, the ringing at each end of the derivative is much more pronounced, as witnessed in the error graphs of Fig. A.6, where the vertical scale is nearly 40× larger than the previous case. The top graph is for the non-windowed case, with $\sigma = 3.60$, while the bottom graph is with the window applied, showing an order-of-magnitude less ringing, with $\sigma = 0.33$.

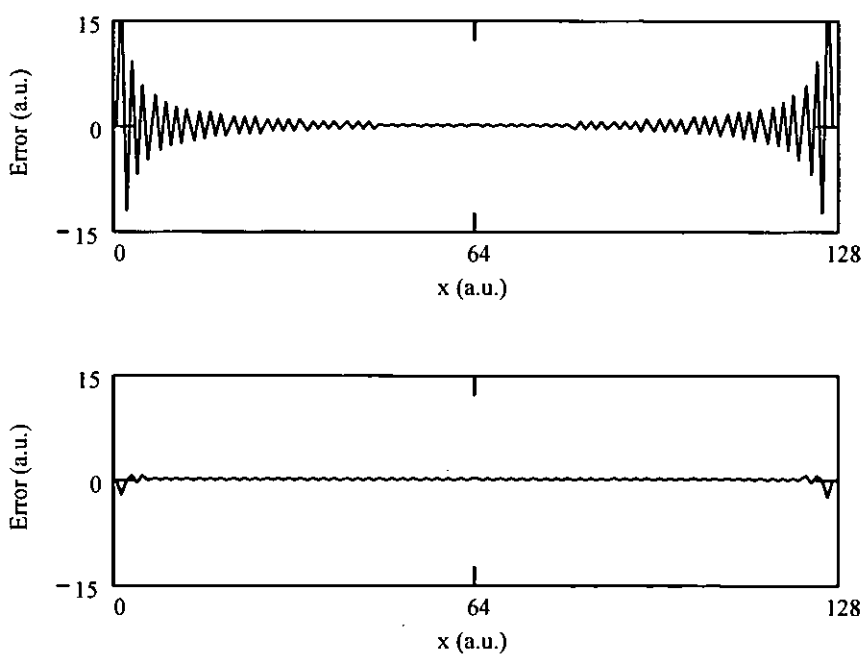

Fig. A.6: Difference between FDT and analytic derivative of aperiodic parabolic signal; no window (top), Hamming window (bottom).

Now the noise performance is examined. Returning to the original signal ($b = 0$), additive, random noise uniformly distributed within the range 0—5 is introduced. The resulting signal is shown in Fig. A.7

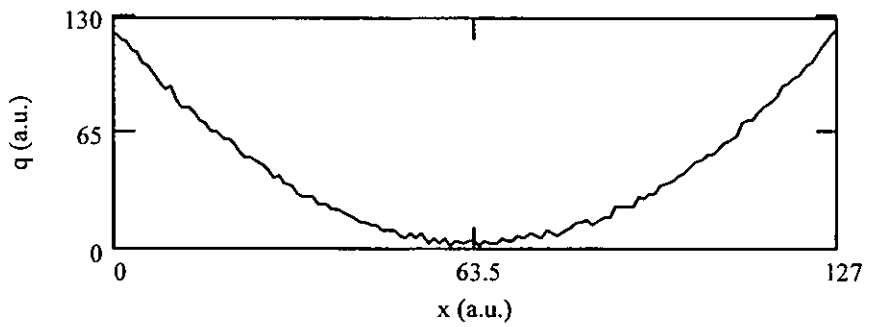

Fig. A.7: Parabolic signal with noise added.

The derivative of the above signal is shown in Fig. A.8, where the vertical scale is the same as for the previous case. The top graph is the non-windowed instance, having $\sigma = 2.59$, while the bottom graph shows markedly less noise at $\sigma = 0.78$.

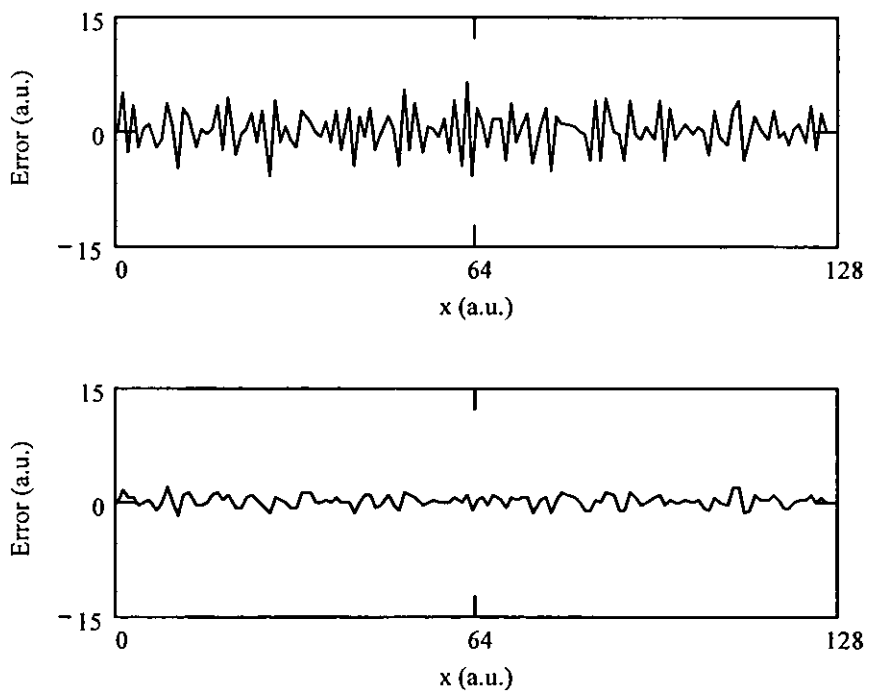

Fig. A.8: Differences between FDT and analytic derivative of noisy parabolic signal; no window (top), Hamming window (bottom).

A.2 INTEGRATION

For the integration, a simple analytical function is chosen for demonstrating the FIT. A linear function of the form $q(x) = (a/N)x$ is used, the integral of which is $g(x) = \frac{1}{2}(a/N)x^2 + b$, where b is an unknown constant. For $a = 128$ and $N = 128$, then the signal is shown in Fig. A.9, centred about zero on the vertical axis.

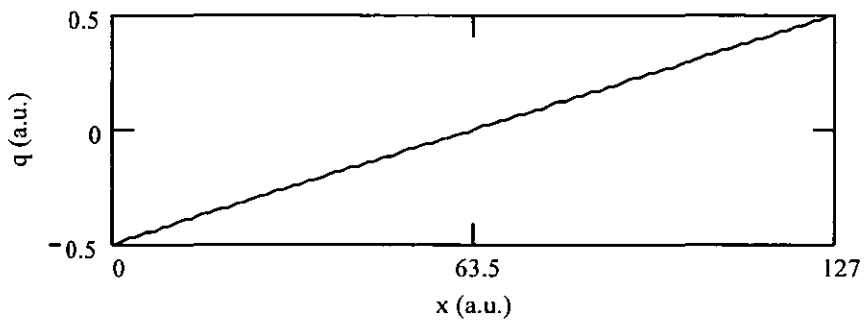

Fig. A.9: Linear signal for demonstrating the FIT.

The integral of the above signal, using the FIT (without window), is then shown by the real component of the integral, in Fig. A.10.

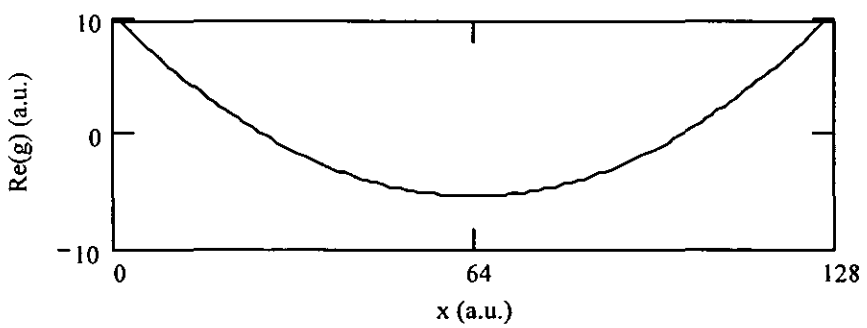

Fig. A.10: Integral of the linear signal.

To confirm the validity of this result, the difference with respect to the analytic quadratic is shown in Fig. A.11. The top graph is with no window function, giving $\sigma = 5.6 \times 10^{-3}$, and the bottom graph is with a frequency-domain Hamming window, showing an order-of-magnitude less error at $\sigma = 3.9 \times 10^{-4}$. The effect of the window

is relatively large here because the original signal is an odd function, thus not meeting the periodicity criterion of the FFT.

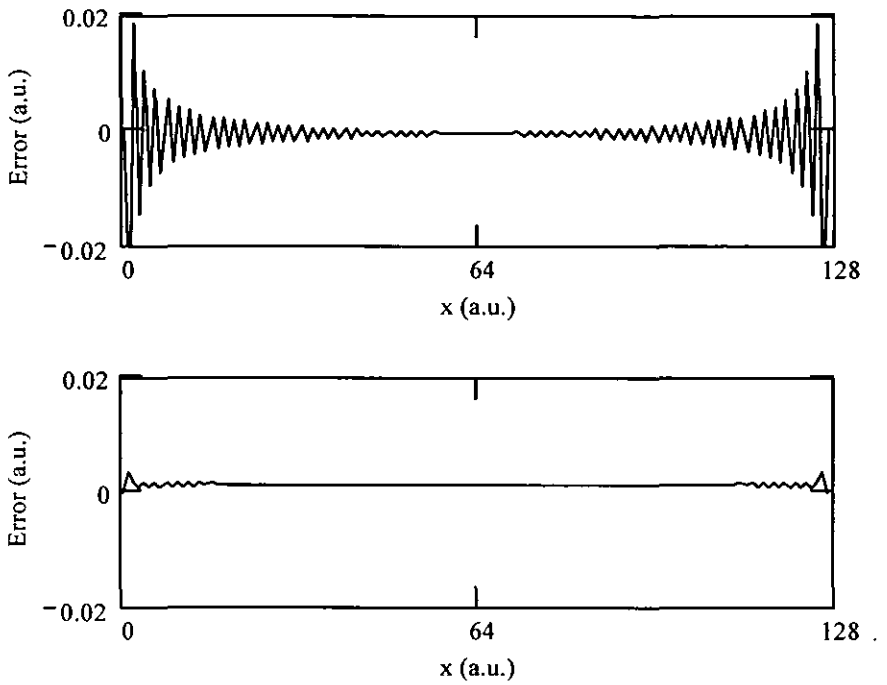

Fig. A.11: Differences between FIT and analytic integral of linear signal; no window (top), Hamming window (bottom).

A.3 CARRIER DEMODULATION

The FDT is now amalgamated with the Fourier transform method, FTM (see Sections 2.5.4 and 3.3.2), to confirm the premise of calculating the phase derivative directly from interferometric carrier fringes.

A carrier of frequency f is phase-modulated with a parabolic signal bx^2:

$$q(x) = \sin\left(\frac{2\pi fx}{N} + \frac{bx^2}{N}\right) \tag{A.7}$$

The derivative is then of the form:

$$g(x) = q'(x) = \left(\frac{2\pi f}{N} + \frac{2bx}{N}\right)\cos\left(\frac{2\pi fx}{N} + \frac{bx^2}{N}\right) \tag{A.8}$$

The function of Eq. (A.7) is plotted in Fig. A.12, for $f = 6.5$, $N = 256$ and $b = 0.128$, where it is noted that the ends of the function do not meet the periodicity condition.

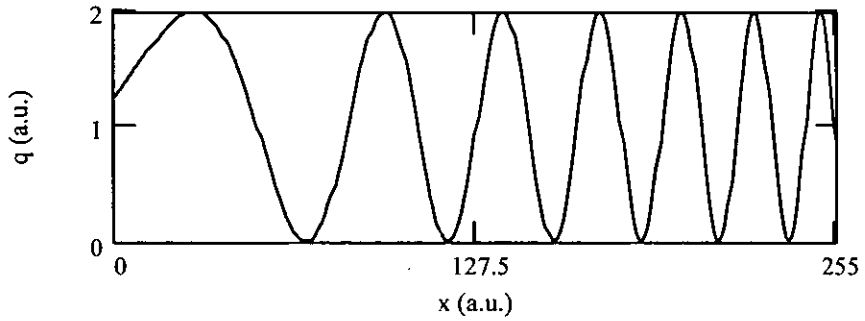

Fig. A.12: Phase-modulated carrier signal.

In the Fourier domain, the FTM is implemented by masking the negative frequency components (setting them to zero), then multiplying by the window function. While in the Fourier domain, the spectrum is also multiplied by the FDT factor. Inverse Fourier transforming then furnishes the derivatives plotted in Fig. A.13: the real component (dotted trace) is the derivative of the entire modulated carrier signal [that is, it equals Eq. (A.8)], while the magnitude of the derivative (solid trace) is the derivative of the carrier phase-modulation term (representing, for example, object strain). The phase derivative is (approximately) a straight line—as expected since the phase modulation is parabolic. The fact that the phase derivative matches the modulation envelope of the carrier derivative is not surprising since the amplitude-modulation term of the cosine in Eq. (A.8) is the derivative of the input signal, according to the chain rule.

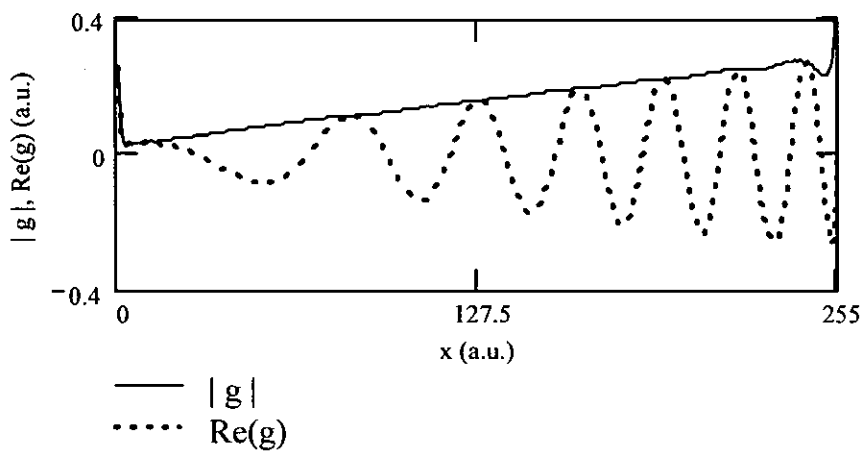

Fig. A.13: Result of combined FTM and FDT—derivative of the carrier signal, magnitude (solid) and real component (dotted).

The FTM-FDT phase derivative is now compared with the analytic result—the differences are shown in Fig. A.14, for no-window case (top) and Hamming window (bottom). Both plots show similar shape, but with more ringing when no window is used. The respective standard deviations are $\sigma = 0.024$ and $\sigma = 0.0089$, a difference by a factor of approximately three.

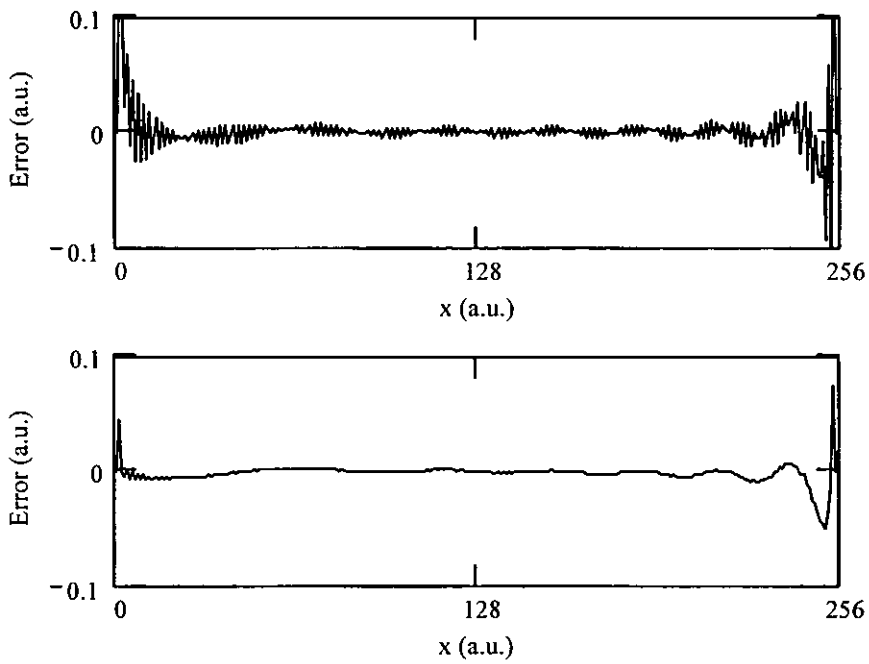

Fig. A.14: Differences between FTM-FDT and analytic derivative of phase-modulation signal; no window (top), Hamming window (bottom).

For completeness, the phase of the derivative function $g(x)$ is now examined. The phase of the FTM-FDT function (with Hamming window) is calculated from the arctangent operator of Eq. (3.30). Unwrapping the phase to remove 2π phase-wraps, and then subtracting the carrier frequency term, the solid trace of Fig. A.15 is arrived at, where it is apparent that this represents the original parabolic phase modulation term of the carrier fringes. To confirm this, the theoretical phase modulation term from Eq. (A.7) is plotted alongside (dotted trace). The two curves match to within a small tilt term.

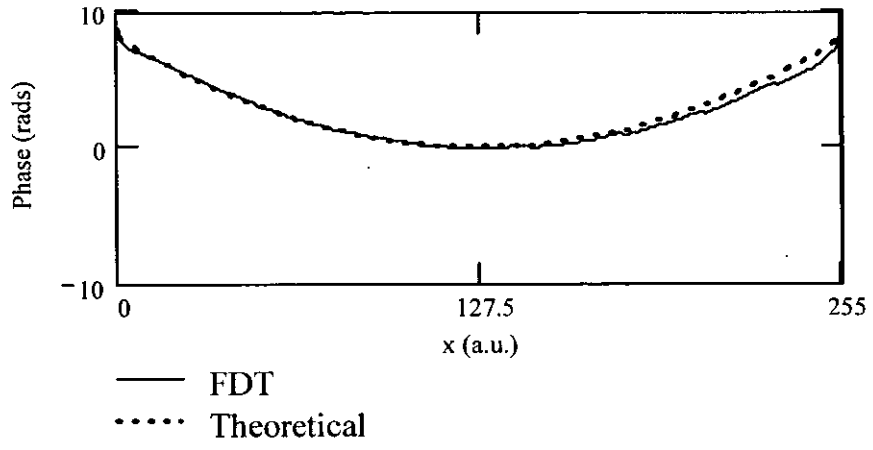

Fig. A.15: Phase of the FTM-FDT operation on the modulated carrier signal, after unwrapping and carrier term removal (solid trace); original phase-modulation term (dotted trace).

Appendix B: Sensitivity Calculation

ESPI OOP Sensitivity Analysis **ESPI-OOPsens.mcd**

D. Farrant 6/03

No. calculation points $N_{points} := 20$ $i := 0..N_{points}$ $j := 0..N_{points}$

Centre $c := 0.5 \cdot N_{points}$ $c = 10$

Object parameters $x_M := 500$ $y_M := x_M$ $z_M := 0$

System paramters $s := 200$ $L := 1000$ $\lambda := 0.532\mu \cdot m$ $\mu \equiv 10^{-3}$

$t := 0$ $z := -L + z_M$

Object coordinates $X_i := \frac{x_M \cdot (i - c)}{c}$ $Y_j := \frac{y_M \cdot (j - c)}{c}$

Illumination vector $R_1(x1, y1, z1, s1) := \sqrt{(x1 - s1)^2 + y1^2 + z1^2}$

Observation vector $R_2(x1, y1, z1) := \sqrt{(t - x1)^2 + y1^2 + z1^2}$

Sensitivity eqns

$$K_1(x0, y0, z0, s0) := \frac{t - x0}{R_2(x0, y0, z0)} - \frac{x0 - s0}{R_1(x0, y0, z0, s0)}$$

$$K_2(x0, y0, z0, s0) := \frac{-y0}{R_2(x0, y0, z0)} - \frac{y0}{R_1(x0, y0, z0, s0)}$$

$$K_3(x0, y0, z0, s0) := \frac{-z0}{R_2(x0, y0, z0)} - \frac{z0}{R_1(x0, y0, z0, s0)}$$

Parametric eqns $R_A := \frac{L}{2x_M}$ $R_P := \frac{L}{z_M}$ $R_S := \frac{s}{L}$ $\theta := \operatorname{atan}(R_S)$

$R_A = 1$ $R_P =$ ∎ $R_S = 0.2$ $\theta = 11.31\,\text{deg}$

Object deformation components $d_1 := 0\mu \cdot m$ $d_2 := 0\mu \cdot m$ $d_3 := 1\mu \cdot m$

$em := \text{if}(d_3 = 0, 0, 1)$ $em = 1$

3D sensitivity eqn

$$OPD(x,y,z,s) := K_1(x,y,z,s)\cdot d_1 + K_2(x,y,z,s)\cdot d_2 + K_3(x,y,z,s)\cdot d_3$$

Relative sensitivity error

$$\phi 1(x,y,z,\alpha) := OPD(x,y,z,\alpha) \qquad \phi 2(x,y,z,\alpha) := K_3(0,0,z,\alpha)\cdot 1\mu\cdot m$$

$$e(x,y,z,\alpha) := \frac{\phi 1(x,y,z,\alpha) - \phi 2(x,y,z,\alpha)\cdot em}{\phi 2(x,y,z,\alpha)} \qquad \phi 2(0,0,z,s) = 1.981\mu\cdot m$$

Calculate matrix $E(i,j,\alpha) := e(X_i, Y_j, z, \alpha)\cdot 100$ $A_{i,j} := E(i,j,s)$

Statistics $Mx := \max(A)$ $Mn := \min(A)$ $PV := Mx - Mn$

$Mx = 0.479$ $Mn = -20.498$ $PV = 20.978$

Calculate stats on submatrices (smaller object dimensions)

$$a := 0..9 \qquad B_a := \max\left(\overrightarrow{|submatrix(A, 1\cdot a, 20 - 1\cdot a, 1\cdot a, 20 - 1\cdot a)|}\right)$$

$$R(s) := \frac{K_1(0,0,z,s)}{K_3(0,0,z,s)} \qquad R(s) = 0.099 \qquad RA_a := \frac{-L}{2\cdot X_a}$$

Relative sens err (%):

$$B^T = (20.498\ 17.796\ 15.101\ 12.453\ 9.903\ 7.506\ 5.325\ 3.424\ 1.867\ 0.71)$$

Aspect Ratios

$$RA^T = (1.000\ 1.111\ 1.250\ 1.429\ 1.667\ 2.000\ 2.500\ 3.333\ 5.000\ 10.000)$$

Sens err along diagonal for various s [use E(i,c,0) for horizontal]

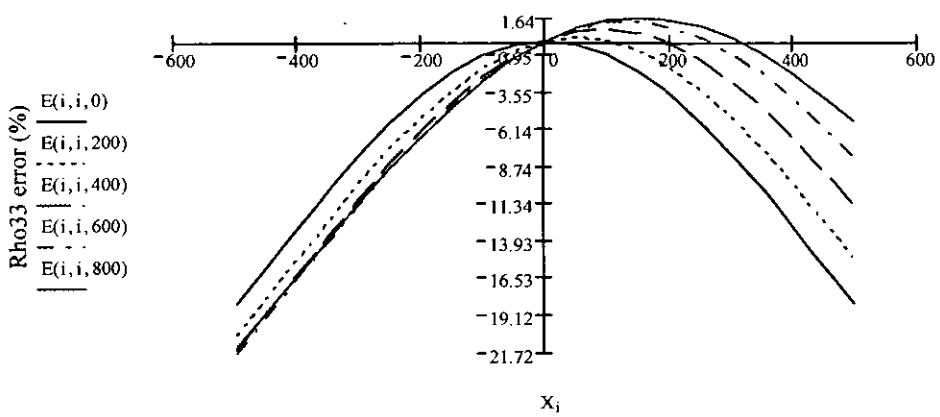

Write data to file

WRITEPRN("ESPI-OOP-Rs-E33.txt") := RA^T

APPENDPRN("ESPI-OOP-Rs-E33.txt") := B^T

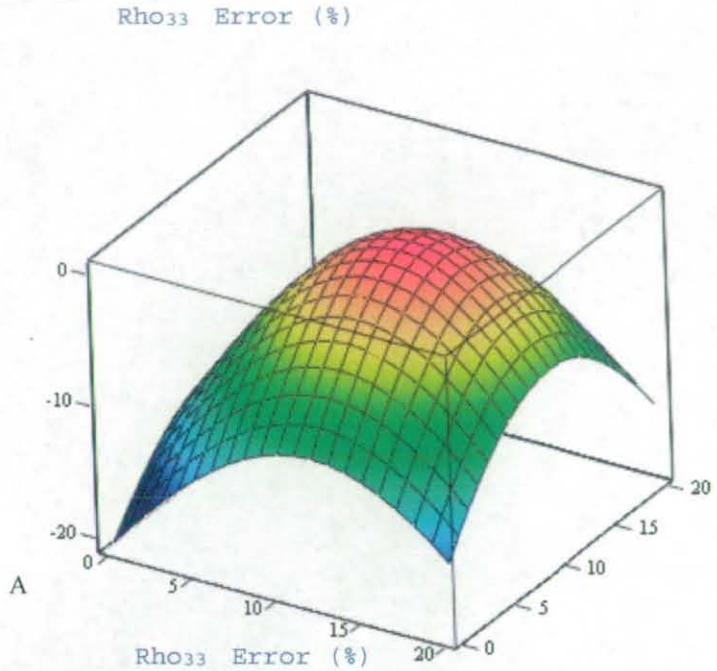

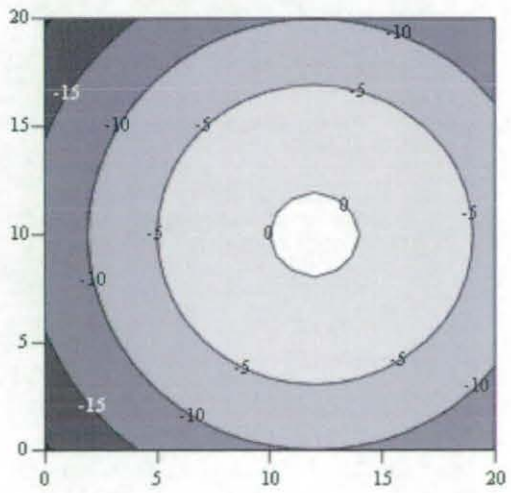

A

1/K3 sensitivity factor

$$K_{i,j} := -K_3(X_i, Y_j, L, s)^{-1}$$

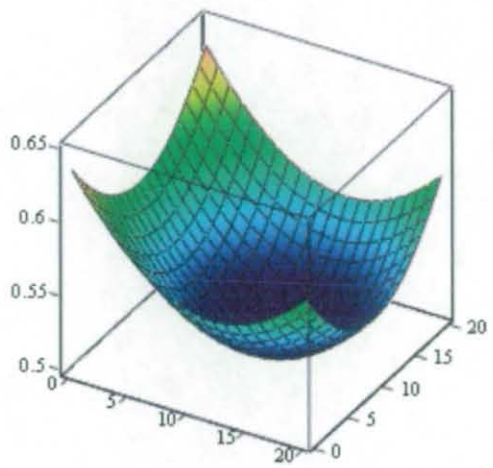

K

ESPI IP Sensitivity Analysis **ESPI-IPsens.mcd**

D. Farrant 6/03

No. calculation points $N_{points} := 20$ $i := 0..N_{points}$ $j := 0..N_{points}$

Centre $c := 0.5 \cdot N_{points}$ $c = 10$

Object parameters $x_M := 500$ $y_M := x_M$ $z_M := 0$

System paramters $s := 200$ $L := 1000$ $\lambda := 0.532\mu \cdot m$ $\mu \equiv 10^{-3}$

$z := -L + z_M$

Object coordinates $X_i := \frac{x_M \cdot (i - c)}{c}$ $Y_j := \frac{y_M \cdot (j - c)}{c}$

Illumination vector $R_1(x1, y1, s1) := \sqrt{(x1 - s1)^2 + y1^2 + z^2}$

Observation vector $R_2(x1, y1, s2) := \sqrt{(x1 - s2)^2 + y1^2 + z^2}$

Sensitivity eqns $K_1(x0, y0, s0) := \frac{x0 + s0}{R_1(x0, y0, -s0)} - \frac{x0 - s0}{R_2(x0, y0, s0)}$

$K_2(x0, y0, s0) := \frac{y0}{R_1(x0, y0, -s0)} - \frac{y0}{R_2(x0, y0, s0)}$

$K_3(x0, y0, s0) := \frac{z}{R_1(x0, y0, -s0)} - \frac{z}{R_2(x0, y0, s0)}$

Parametric eqns $R_A := \frac{L}{2x_M}$ $R_P := \frac{L}{z_M}$ $R_S := \frac{s}{L}$ $\theta := \operatorname{atan}(R_S)$

$R_A = 1$ $R_P =$ ∎ $R_S = 0.2$ $\theta = 11.31\text{deg}$

Object deformation components $d_1 := 1\mu \cdot m$ $d_2 := 0\mu \cdot m$ $d_3 := 0\mu \cdot m$

$em := if(d_1 = 0, 0, 1)$ $em = 1$

3D sensitivity eqn

$$OPD(x,y,s) := K_1(x,y,s)\cdot d_1 + K_2(x,y,s)\cdot d_2 + K_3(x,y,s)\cdot d_3$$

Relative sensitivity error

$$\phi 1(x,y,\alpha) := OPD(x,y,\alpha) \qquad \phi 2(x,y,\alpha) := K_1(0,0,\alpha)\cdot 1\cdot\mu\cdot m$$

$$e(x,y,\alpha) := \frac{\phi 1(x,y,\alpha) - \phi 2(x,y,\alpha)\cdot em}{\phi 2(x,y,\alpha)} \qquad \phi 2(0,0,s) = 0.392\mu\cdot m$$

Calculate matrix $E(i,j,\alpha) := e(X_i, Y_j, \alpha)\cdot 100$ $A_{i,j} := E(i,j,s)$

Statistics $Mx := max(A)$ $Mn := min(A)$ $PV := Mx - Mn$

$Mx = 0$ $Mn = -30.779$ $PV = 30.779$

Calculate stats on submatrices (smaller object dimensions)

$$a := 0..9 \qquad B_a := \max\left(\overrightarrow{|submatrix(A, 1\cdot a, 20 - 1\cdot a, 1\cdot a, 20 - 1\cdot a)|}\right)$$

$$R(s) := \frac{K_3(0,0,s)}{K_1(0,0,s)} \qquad R(s) = 0 \qquad RA_a := \frac{-L}{2\cdot X_a}$$

Relative sens err (%):

$$B^T = (30.779\ 26.67\ 22.472\ 18.273\ 14.187\ 10.347\ 6.905\ 4.017\ 1.83\ 0.465)$$

Aspect Ratios

$$RA^T = (1.000\ 1.111\ 1.250\ 1.429\ 1.667\ 2.000\ 2.500\ 3.333\ 5.000\ 10.000)$$

Sens err along diagonal for various s [use E(i,c,0) for horizontal]

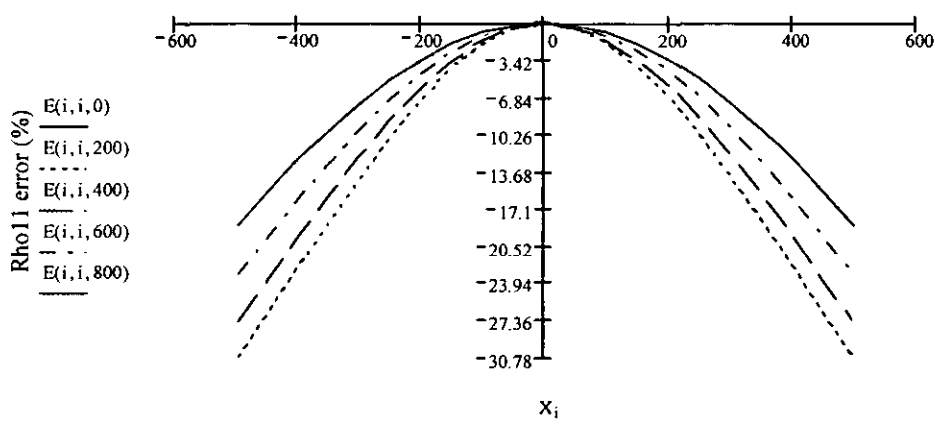

Write data to file

$$\text{WRITEPRN}(\text{"ESPI-OOP-Rs-E11.txt"}) := RA^{T}$$

$$\text{APPENDPRN}(\text{"ESPI-OOP-Rs-E11.txt"}) := B^{T}$$

Rho_{11} Error (%)

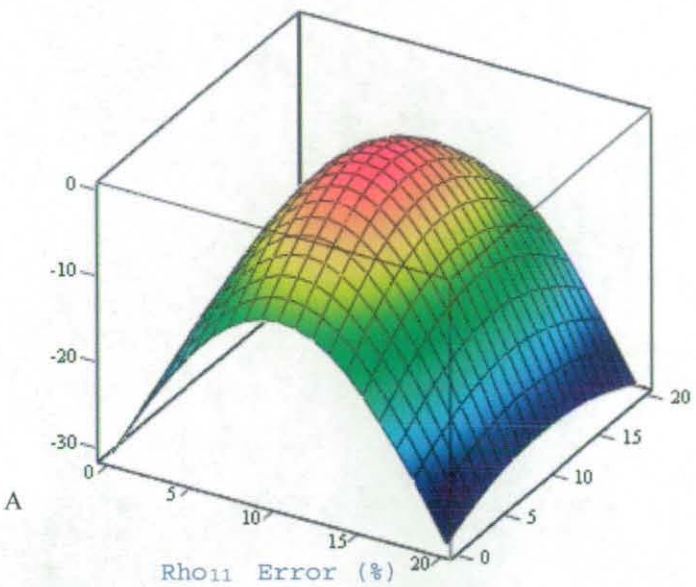

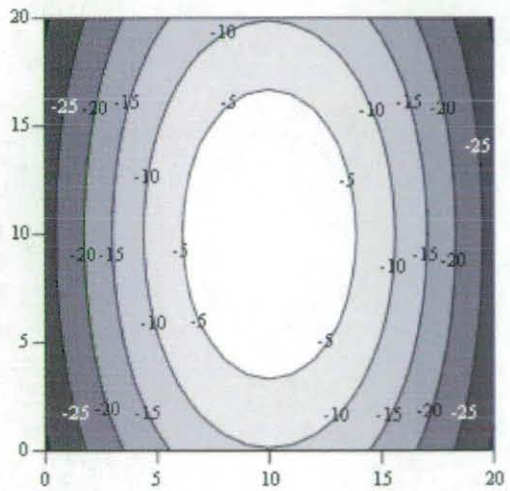

1/K1 sensitivity factor

$$K_{i,j} := K_1(X_i, Y_j, s)^{-1}$$

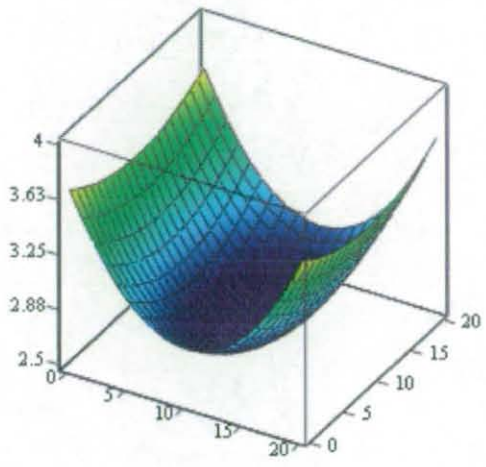

K

Publications

The publications related to the thesis work are listed below:

1. K. Hibino, D.I. Farrant, B.K. Ward, B.F. Oreb, "Dynamic range of Ronchi test with a phase-shifted sinusoidal grating," Appl. Opt. 36, 6178-6189 (1997).
2. D.I. Farrant, G.H. Kaufmann, J.N. Petzing, J.R. Tyrer, B.F. Oreb, and D. Kerr, "Transient deformation measurement using dual-pulse addition ESPI," Proc. SPIE 3173, 132-140, San Diego (Jul. 1997).
3. D.I. Farrant, Y. Nakano and B.F. Oreb, "Continuous deformation measurement using speckle," National Institute for Theoretical Physics; Propagation and Imaging Science Workshop, Adelaide (Dec. 1997).
4. J.N. Petzing, D. Kerr, J.R. Tyrer, D.I. Farrant, B.F. Oreb and G.H. Kaufmann, "Development of speckle pattern interferometry for transient vibration analysis," Proc. 11th Intnl. Conf. on Experim. Mech., 691-696, Oxford U.K. (Aug. 1998).
5. D.I. Farrant, G.H. Kaufmann, J.N. Petzing, J.R. Tyrer, B.F. Oreb, and D. Kerr, "Measurement of transient deformations with dual-pulse addition Electronic Speckle Pattern Interferometry," Appl. Opt. 37, 7259-7267 (1998).
6. D.I. Farrant, J.N. Petzing, J.R. Tyrer, and B.F. Oreb, "Combined deformation and shape measurement with ESPI," Proc. SPIE 3744, 474-481, Poland (Sep. 1999).
7. D.I. Farrant, J.N. Petzing, and J.R. Tyrer, "Shape-corrected ESPI vibration analysis applied within the design process of an engine," Proc. FASIG (U.K., Sep. 1999).
8. D.I. Farrant and J.N. Petzing, "Sensitivity errors in interferometric deformation metrology," Appl. Opt. 42, 5634-5641 (2003).
9. D.I. Farrant, J.N. Petzing, and J.R. Tyrer, "Geometrically-qualified ESPI vibration analysis of an engine," Opt. Lasers Eng. 42, 659-671 (2004).

Bibliography

1. N. Halliwell, *Laser Vibrometry* (Chapman and Hall, London 1993).

2. J. M. Coupland, "Laser Doppler and Pulsed Laser Velocimetry in Fluid Mechanics" in *Photo-Mechanics*, P. K. Rastogi, ed. (Springer-Verlag, Berlin, Germany, 2000), Vol. 77, pp. 373-412.

3. J. Coupland, "Coherent Detection in Doppler Global Velocimetry: a Simplified Method to Measure Subsonic Fluid Flow Fields," Appl. Opt. 39, 1505-1510 (2000).

4. D. C. Williams (ed.), *Optical Methods in Engineering Metrology* (Chapman & Hall, London; New York, 1993).

5. P. K. Rastogi (ed.), *Optical Measurement Techniques and Applications* (Artech House, Boston, Mass., 1997).

6. F. Gascon and F. Salazar, "Minimum Diameter of the Read-Out Laser Beam in Double-Exposure Speckle Photography," Opt. Commun. 172, 77-84 (1999).

7. M. Sjodahl, "Some Recent Advances in Electronic Speckle Photography," Opt. Las. Eng. 29, 125-144 (1998).

8. P. K. Rastogi (ed.), *Holographic Interferometry* (Springer, Berlin ; New York, 1994).

9. R. S. Sirohi (ed.) , *Speckle Metrology* (Marcel Dekker, New York, 1993).

10. R. Jones and C. Wykes, *Holographic and Speckle Interferometry : A discussion of the theory, practice and application of the techniques* (Cambridge U.P., Cambridge, 1983).

11. D. W. Robinson and G. T. Reid (eds.), *Interferogram Analysis* (Institute of Physics, Bristol, U.K., 1993).

12. J. C. Dainty (ed.), *Laser Speckle and Related Phenomena* (Springer-Verlag, Berlin, 1984).

13. J. N. Butters and J. A. Leendertz, "Holographic and video techniques applied to engineering measurement," J. Meas. Control 4, 349-354 (1971).

14. A. Macovski, S. D. Ramsey, and L. F. Schaefer, "Time-lapse interferometry and contouring using television systems," Appl. Opt. 10, 2722-2727 (1971).

15. S. Nakadate, T. Yatagai, and H. Saito, "Electronic speckle pattern interferometry using digital image processing techniques," Appl. Opt. 19, 1879-1883 (1980).

16. A. E. Ennos, "Speckle Interferometry" in *Laser Speckle and Related Phenomena*, J. C. Dainty, ed. (Springer Verlag, Berlin, 1984), pp. 203-253.

17. D. R. Schmitt and R. W. Hunt, "Optimization of Fringe Pattern Calculation With Direct Correlations in Speckle Interferometry," Appl. Opt. 36, 8848-8857 (1997).

18. B. F. Oreb, K. G. Larkin, P. S. Fairman, and M. Ghaffari, "Moire based optical surface profiler for the minting industry," Proc. SPIE 1776, (1992).

19. D. I. Farrant, J. N. Petzing, J. R. Tyrer, and B. F. Oreb, "Combined deformation and shape measurement with ESPI," Proc. SPIE 3744, 474-481 (1999).

20. R. P. Tatam, J. C. Davies, C. H. Buckberry, and J. D. C. Jones, "Holographic Surface Contouring Using Wavelength Modulation of Laser-Diodes," Opt. Laser Technol. 22, 317-321 (1990).

21. D. M. Meadows, W. O. Johnson, and J. B. Allen, "Generation of surface contours by moiré patterns," Appl. Opt. 9, 942-947 (1970).

22. H. Takasaki, "Moiré topography," Appl. Opt. 9, 1467-1472 (1970).

23. M. Halioua, R. S. Krishnamuthy, H. Liu, and F. P. Chiang, "Projection moire with moving gratings for automated 3-D topography," Appl. Opt. 22, 850-855 (1983).

24. Y. Morimoto and M. Fujigaki, "Automated-Analysis of 3-D Shape and Surface Strain Distributions of a Moving Object Using Stereo Vision," Opt. Las. Eng. 18, 195-212 (1993).

25. B. S. Lee and T. C. Strand, "Profilometry With a Coherence Scanning Microscope," Appl. Opt. 29, 3784-3788 (1990).

26. T. Dresel, G. Hausler, and H. Venzke, "3-Dimensional Sensing of Rough Surfaces by Coherence Radar," Appl. Opt. 31, 919-925 (1992).

27. K. G. Larkin, "Efficient Nonlinear Algorithm for Envelope Detection in White Light Interferometry," J. Opt. Soc. Am. A 13, 832-843 (1996).

28. M. Halioua and H. C. Liu, "Optical Three-Dimensional Sensing by Phase Measuring Profilometry," Opt. Las. Eng. 11, 185-215 (1989).

29. F. Bremand, "Phase Unwrapping Technique for Object Relief Determination," Opt. Las. Eng. 21, 49-60 (1994).

30. D. I. Farrant, "CSIRO Laboratory Notebook," (1997).

31. H. O. Saldner and J. M. Huntley, "Profilometry Using Temporal Phase Unwrapping and a Spatial Light Modulator-Based Fringe Projector," Opt. Eng. 36, 610-615 (1997).

32. H. O. Saldner and J. M. Huntley, "Temporal Phase Unwrapping: Application to Surface Profiling of Discontinuous Objects," Appl. Opt. 36, 2770-2775 (1997).

33. M. Takeda, Q. Gu, M. Kinoshita, H. Takai, and Y. Takahashi, "Frequency-Multiplex Fourier-Transform Profilometry: a Single-Shot Three-Dimensional Shape Measurement of Objects With Large Height Discontinuities and/or Surface Isolations," Appl. Opt. 36, 5347-5354 (1997).

34. K. L. Boyer and A. C. Kak, "Color-Encoded Structured Light for Rapid Active Ranging," Ieee Transactions on Pattern Analysis and Machine Intelligence 9, 14-28 (1987).

35. M. Takeda and H. Yamamoto, "Fourier-Transform Speckle Profilometry - 3-Dimensional Shape Measurements of Diffuse Objects With Large Height Steps and/or Spatially Isolated Surfaces," Appl. Opt. 33, 7829-7837 (1994).

36. R. Rodriguez-Vera, D. Kerr, and F. Mendoza-Santoyo, "Electronic Speckle Contouring," J. Opt. Soc. Am. A 9, 2000-2008 (1992).

37. A. R. Ganesan and R. S. Sirohi, "New method of contouring using Digital Speckle Pattern Interferometry (DSPI)," in *Optical testing and metrology II : 27-30 June, 1988, Dearborn, Michigan*, Grover, C. P, Proc. SPIE 954, 327-332 (1988).

38. S. Winther and G. A. Slettemoen, "An ESPI contouring technique in strain analysis," Proc. SPIE 473, 44-47 (1984).

39. C. Joenathan, B. Pfister, and H. J. Tiziani, "Contouring by Electronic Speckle Pattern Interferometry Employing Dual Beam Illumination," Appl. Opt. 29, 1905-1911 (1990).

40. J. H. Blatt, H. C. C. Ho, and E. H. Young, "Generation of Moire Contours With Acoustooptic Cells," Opt. Eng. 28, 996-998 (1989).

41. L. S. Wang, K. Jambunathan, B. N. Dobbins, and S. P. He, "Measurement of Three-Dimensional Surface Shape and Deformations Using Phase Stepping Speckle Interferometry," Opt. Eng. 35, 2333-2340 (1996).

42. L. S. Wang and S. Krishnaswamy, "Shape Measurement Using Additive-Subtractive Phase Shifting Speckle Interferometry," Meas. Sci. Technol. 7, 1748-1754 (1996).

43. M. Reeves, N. Taylor, C. Edwards, D. Williams, and C. H. Buckberry, "A Study of Brake Disc Modal Behaviour During Squeal Generation Using High-Speed Electronic Speckle Pattern Interferometry and Near-Field Sound Pressure Measurements," Proc. Inst. Mech. Eng. Part D-J. Automob. Eng. 214, 285-296 (2000).

44. M. A. Beeck and W. Hentschel, "Laser Metrology - a Diagnostic Tool in Automotive Development Processes," Opt. Las. Eng. 34, 101-120 (2000).

45. G. Graham, J. Petzing, M. Lucas, and J. Tyrer, "Quantitative Modal Analysis Using Electronic Speckle Pattern Interferometry," Opt. Las. Eng. 31, 147-161 (1999).

46. T. Etoh and K. Takehara, "Specifications of high-speed image sensors based on requirements of multi-scientific fields," Proc. SPIE 3173, 57-66 (1997).

47. G. K. Bhat, "Measurement of strains in turbine blades vibrating at resonance using electo-optic holography," J. Mod. Opt. 42, 667-677 (1995).

48. A. J. Moore and C. Perezlopez, "Low-Frequency Harmonic Vibration Analysis With Double-Pulsed Addition Electronic Speckle Pattern Interferometry," Opt. Eng. 35, 2641-2650 (1996).

49. P. Hariharan, B. F. Oreb, and C. H. Freund, "Stroboscopic Holographic-Interferometry - Measurements of Vector Components of a Vibration," Appl. Opt. 26, 3899-3903 (1987).

50. R. Spooren, "Double-Pulse Subtraction Tv Holography," Opt. Eng. 31, 1000-1007 (1992).

51. G. Pedrini, B. Pfister, and H. Tiziani, "Double Pulse-Electronic Speckle Interferometry," J. Mod. Opt. 40, 89-96 (1993).

52. J. B. Schemm and C. M. Vest, "Fringe Pattern Recognition and Interpolation Using Nonlinear Regression Analysis.," Appl. Opt. 22, 2850-2853 (1983).

53. J. S. Slepicka and S. S. Cha, "Stabilized Nonlinear-Regression for Interferogram Analysis," Appl. Opt. 34, 5039-5044 (1995).

54. K. Creath, "Phase-measurement interferometry techniques" in *Progress in Optics*, E. Wolf , ed. (Elsevier, Amsterdam, 1988), Vol. 26, pp. 349-394.

55. D. I. Farrant, A. J. Leistner, B. F. Oreb, M. A. Suchting, and C. J. Walsh, "Metrology of Ligo Pathfinder Optics," Proc. SPIE 3134, 79-85 (1997).

56. K. Hibino, B. F. Oreb, D. I. Farrant, and K. G. Larkin, "Phase-Shifting Algorithms for Nonlinear and Spatially Nonuniform Phase Shifts," J. Opt. Soc. Am. A 14, 918-930 (1997).

57. S. Nakadate and H. Saito, "Fringe scanning speckle-pattern interferometry," Appl. Opt. 24, 2172-2180 (1985).

58. K. Creath, "Phase-shifting speckle interferometry," Appl. Opt. 24, 3053-3058 (1985).

59. A. J. P. van Haasteren and H. J. Frankena, "Real-Time Displacement Measurement Using a Multicamera Phase-Stepping Speckle Interferometer," Appl. Opt. 33, 4137-4142 (1994).

60. J. Burke, H. Helmers, C. Kunze, and V. Wilkens, "Speckle Intensity and Phase Gradients: Influence on Fringe Quality in Spatial Phase Shifting Espi-Systems," Opt. Commun. 152, 144-152 (1998).

61. D. M. Shough, O. Y. Kwon, and D. F. Leary, "High-Speed Interferometric Measurement of Aerodynamic Phenomena," Proc. SPIE 1221, 394-403 (1990).

62. Malgorzata Kujawinska and Joanna Wojciak, "Spatial-carrier phase-shifting technique of fringe pattern analysis," in *Proceedings of SPIE - The International Society for Optical Engineering*, 1508, (1991).

63. L. Mertz, "Real-Time Fringe-Pattern Analysis.," Appl. Opt. 22, 1535-1539 (1983).

64. W. W. J. Macy, "Two-Dimensional Fringe-Pattern Analysis.," Appl. Opt. 22, 3898-3901 (1983).

65. P. L. Ransom and J. V. Kokal, "Interferogram Analysis by a Modified Sinusoid Fitting Technique," Appl. Opt. 25, 4199-4204 (1986).

66. A. Davila, D. Kerr, and G. H. Kaufmann, "Fast Electro-Optical System for Pulsed Espi Carrier Fringe Generation," Opt. Commun. 123, 457-464 (1996).

67. K. H. Womack, "Interferometric Phase Measurement Using Spatial Synchronous Detection.," Opt. Eng. 23, 391-395 (1984).

68. Y. Ichioka and M. Inuiya, "Direct phase detecting system," Appl. Opt. 11, 1507-1514 (1972).

69. C. Roddier and F. Roddier, "Interferogram Analysis Using Fourier-Transform Techniques," Appl. Opt. 26, 1668-1673 (1987).

70. M. Takeda, H. Ina, and S. Kobayashi, "Fourier-transform method of fringe pattern analysis for computer-based topography and interferometry," J. Opt. Soc. Am. 72, 156-160 (1982).

71. M. Kujawinska and J. Wojciak, "High accuracy Fourier transform fringe pattern analysis," Opt. Las. Eng. 14, 325-339 (1991).

72. D. J. Bone, H. A. Bachor, and R. J. Sandeman, "Fringe-Pattern Analysis Using a 2-D Fourier-Transform," Appl. Opt. 25, 1653-1660 (1986).

73. R. W. Gerchberg, "Super-resolution through error energy reduction," Optica Acta 21, 709-704 (1974).

74. L. M. Kani and J. C. Dainty, "Super-Resolution Using the Gerchberg Algorithm," Opt. Commun. 68, 11-17 (1988).

75. F. Roddier and C. Roddier, "Wave-Front Reconstruction Using Iterative Fourier-Transforms," Appl. Opt. 30, 1325-1327 (1991).

76. M. Kujawinska, "Spatial Phase Measurement Methods" in *Interferogram Analysis*, D. W. Robinson and G. T. Reid, eds. (Institute of Physics, Bristol, U.K., 1993), pp. 141-193.

77. G. H. Kaufmann and G. E. Galizzi, "Phase Measurement in Temporal Speckle Pattern Interferometry: Comparison Between the Phase-Shifting and the Fourier Transform Methods," Appl. Opt. 41, 7254-7263 (2002).

78. Malgorzata Kujawinska, A. Spik, and J. Wojciak, "Fringe pattern analysis using Fourier transform techniques," Proc. SPIE 1121, 130-135 (1989).

79. K. E. Perry and J. Mckelvie, "A Comparison of Phase-Shifting and Fourier Methods in the Analysis of Discontinuous Fringe Patterns," Opt. Las. Eng. 19, 269-284 (1993).

80. G. Pedrini, Y. L. Zou, and H. J. Tiziani, "Simultaneous Quantitative Evaluation of in-Plane and Out-of- Plane Deformations by Use of a Multidirectional Spatial Carrier," Appl. Opt. 36, 786-792 (1997).

81. T. Takatsuji, B. F. Oreb, D. I. Farrant, and J. R. Tyrer, "Simultaneous Measurement of Three Orthogonal Components of Displacement by Electronic Speckle-Pattern Interferometry and the Fourier Transform Method," Appl. Opt. 36, 1438-1445 (1997).

82. A. J. Moore and J. R. Tyrer, "An Electronic Speckle Pattern Interferometer for Complete Inplane Displacement Measurement," Meas. Sci. Technol. 1, 1024-1030 (1990).

83. T. Kreis, "Digital Holographic Interference-Phase Measurement Using the Fourier-Transform Method," J. Opt. Soc. Am. A 3, 847-855 (1986).

84. K. G. Larkin, D. J. Bone, and M. A. Oldfield, "Natural Demodulation of Two-Dimensional Fringe Patterns. I. General Background of the Spiral Phase Quadrature Transform," J. Opt. Soc. Am. A 18, 1862-1870 (2001).

85. Ronald N. Bracewell, *The Fourier Transform and its Applications* (McGraw-Hill, New York, 1978).

86. A. J. Moore and C. Perezlopez, "Fringe Carrier Methods in Double-Pulsed Addition Espi," Opt. Commun. 141, 203-212 (1997).

87. General Scanning, "G-Series Open-Loop Galvanometers," Http://Www.Genscan.Com/Product/Ospd/g_Open.Html (1998).

88. D. I. Farrant, G. H. Kaufmann, J. N. Petzing, J. R. Tyrer, B. F. Oreb, and D. Kerr, "Measurement of Transient Deformations With Dual-Pulse Addition Electronic Speckle-Pattern Interferometry," Appl. Opt. 37, 7259-7267 (1998).

89. Picart, P., Mercier, R., Lamare, M., and Breteau, J.-M. A simple method for measuring the random variation of an interferometer. Meas. Sci. Technol. 12[8], 1311-1317. August 2001.

90. D. Farrant, *Hybrid Image Processor Design* (Master's Thesis, University of Technology, Sydney, 1992).

91. Warren J. Smith, *Modern Optical Engineering : The Design of Optical Systems* (McGraw Hill, New York; Sydney, 2000).

92. R. A. Soref and M. J. Rafuse, "Electrically controlled birefringence of thin nematic films," J. Appl. Phys. 43, 2029 (1972).

93. S. T. Wu, "Nematic Liquid Crystals for Active Optics" in *Optical Materials*, S. Musikant, ed. (Marcel Dekker, New York, 1990).

94. D. Mayden, "Acousto-optical pulse modulators," J. Quant. Elec. 6, 15-24 (1970).

95. Andersen Laboratories, "OEM Acousto-Optic Modulators," Brochure (1985).

96. Robert G. Hunsperger, *Integrated Optics Theory and Technology* (Springer, Berlin; New York, 1995).

97. H. Matsumoto and A. Hirai, "A White-Light Interferometer Using a Lamp Source and Heterodyne Detection With Acousto-Optic Modulators," Opt. Commun. 170, 217-220 (1999).

98. T. B. Carlson, S. M. Denzer, T. R. Greenlee, R. P. Groschen, R. W. Peterson, and G. M. Robinson, "Vibration-Resistant Direct-Phase-Detecting Optical Interferometers," Appl. Opt. 36, 7162-7171 (1997).

99. Adrian Korpel, *Acousto-Optics* (Marcel Dekker, New York, 1988).

100. Joseph W. Goodman, *Introduction to Fourier Optics* (McGraw-Hill, New York, 1996).

101. M. S. Mermelstein, D. L. Feldkhun, and L. G. Shirley, "Video-Rate Surface Profiling With Acousto-Optic Accordion Fringe Interferometry," Opt. Eng. 39, 106-113 (2000).

102. More models than a Paris catwalk.

103. I. C. Chang, "Acousto-optic devices and applications" in *Handbook of Optics*, M. Bass, ed. (Optical Society of America/McGraw-Hill, New York, 1995).

104. M. King, "Fourier optics and radar signal processing" in *Applications of Optical Fourier Transforms*, Henry Stark, ed. (Academic, N.Y., 1982).

105. N. Friedman, A. Kaplan, and N. Davidson, "Acousto-Optic Scanning System With Very Fast Nonlinear Scans," Opt. Lett. 25, 1762-1764 (2000).

106. A. Sliwinski, "Selected aspects of polarization of light in ultrasonic light diffraction," J. Opt. A: Pure Appl. Opt. 3, 93-101 (2001).

107. F. M. Santoyo, A. J. Moore, J. R. Tyrer, and N. A. Ochoa, "Noise-Reduction in Twin-Pulsed Addition Electronic Speckle Pattern Interferometry Fringe Patterns ," Opt. Eng. 33, 1712-1716 (1994).

108. G. H. Kaufmann, D. Kerr, and N. A. Halliwell, "Contrast Enhancement of Pulsed Espi Addition Fringes," Opt. Las. Eng. 20, 25-34 (1994).

109. A. J. Moore and C. Perezlopez, "Fringe Visibility Enhancement and Phase Calculation in Double-Pulsed Addition Espi," J. Mod. Opt. 43, 1829-1844 (1996).

110. D. I. Farrant, G. H. Kaufmann, J. N. Petzing, J. R. Tyrer, B. F. Oreb, and D. Kerr, "Transient Deformation Measurement Using Dual-Pulse Addition Espi," Proc. SPIE 3173, 132-140 (1997).

111. N. A. Ochoa, F. M. Santoyo, A. J. Moore, and C. P. Lopez, "Contrast Enhancement of Electronic Speckle Pattern Interferometry Addition Fringes," Appl. Opt. 36, 2783-2787 (1997).

112. K. Hibino, B. F. Oreb, D. I. Farrant, and K. G. Larkin, "Phase-Shifting for Nonsinusoidal Wave-Forms With Phase-Shift Errors," J. Opt. Soc. Am. A 12, 761-768 (1995).

113. C. Y. Poon, M. Kujawinska, and C. Ruiz, "Spatial-carrier phase shifting method of fringe analysis for Moire interferometry," Journal of Strain Analysis for Engineering Design 28, 79-88 (1993).

114. A. Fernandez, G. H. Kaufmann, A. F. Doval, J. Blanco-Garcia, and J. L. Fernandez, "Comparison of Carrier Removal Methods in the Analysis of TV Holography Fringes by the Fourier Transform Method," Opt. Eng. 37, 2899-2905 (1998).

115. Charles M. Vest, *Holographic Interferometry* (Wiley, New York, 1979).

116. H. A. Vrooman and A. A. M. Maas, "Image-Processing Algorithms for the Analysis of Phase-Shifted Speckle Interference Patterns," Appl. Opt. 30, 1636-1641 (1991).

117. A. J. Moore and J. R. Tyrer, "Two-dimensional strain measurement with ESPI," Opt. Las. Eng. 24, 381-402 (1996).

118. M. Facchini and P. Zanetta, "Derivatives of Displacement Obtained by Direct Manipulation of Phase-Shifted Interferograms," Appl. Opt. 34, 7202-7206 (1995).

119. G. H. Kaufmann and G. E. Galizzi, "Evaluation of a Method to Determine Interferometric Phase Derivatives," Opt. Las. Eng. 27, 451-465 (1997).

120. Y. Y. Hung, J. D. Hovanesian, and J. Takezaki, "A Fringe Carrier Technique for Unambiguous Determination of Fringe Orders in Shearography," Opt. Las. Eng. 8, 73-81 (1988).

121. A. Davila, G. H. Kaufmann, and C. Perez-Lopez, "Transient Deformation Analysis by a Carrier Method of Pulsed Electronic Speckle-Shearing Pattern Interferometry," Appl. Opt. 37, 4116-4122 (1998).

122. G. K. Bhat, "A Hybrid Fringe Analysis Technique for the Elimination of Random Noise in Interferometric Wrapped Phase Maps," Opt. Commun. 111, 214-218 (1994).

123. F. Roddier and C. Roddier, "Wave-Front Reconstruction Using Iterative Fourier-Transforms," Appl. Opt. 30, 1325-1327 (1991).

124. K. R. Freischlad and C. L. Koliopoulos, "Modal Estimation of a Wave-Front From Difference Measurements Using the Discrete Fourier-Transform," J. Opt. Soc. Am. A 3, 1852-1861 (1986).

125. A. Dubra, C. Paterson, and C. Dainty, "Wave-Front Reconstruction From Shear Phase Maps by Use of the Discrete Fourier Transform," Appl. Opt. 43, 1108-1113 (2004).

126. J. Campos, L. P. Yaroslavsky, A. Moreno, and M. J. Yzuel, "Integration in the Fourier Domain for Restoration of a Function From Its Slope: Comparison of Four Methods," Opt. Lett. 27, 1986-1988 (2002).

127. S. Loheide and I. Weingartner, "New Procedure for Wavefront Reconstruction," Optik 108, 53-62 (1998).

128. K. Itoh, "Analysis of the phase unwrapping algorithm," Appl. Opt. 21, 2470 (1982).

129. Dennis C. Ghiglia and Mark D. Pritt, *Two-Dimensional Phase Unwrapping : Theory, Algorithms, and Software* (Wiley, New York ; Brisbane, 1998).

130. T. R. Judge and P. J. Bryanstoncross, "A Review of Phase Unwrapping Techniques in Fringe Analysis," Opt. Las. Eng. 21, 199-239 (1994).

131. G. Fornaro, G. Franceschetti, R. Lanari, E. Sansosti, and M. Tesauro, "Global and Local Phase-Unwrapping Techniques: a Comparison," J. Opt. Soc. Am. A 14, 2702-2708 (1997).

132. J. Strand and T. Taxt, "Performance Evaluation of Two-Dimensional Phase Unwrapping Algorithms," Appl. Opt. 38, 4333-4344 (1999).

133. P. Ettl and K. Creath, "Comparison of Phase-Unwrapping Algorithms by Using Gradient of First Failure," Appl. Opt. 35, 5108-5114 (1996).

134. J. M. Huntley and H. Saldner, "Temporal Phase-Unwrapping Algorithm for Automated Interferogram Analysis," Appl. Opt. 32, 3047-3052 (1993).

135. D. C. Ghiglia and L. A. Romero, "Robust 2-Dimensional Weighted and Unweighted Phase Unwrapping That Uses Fast Transforms and Iterative Methods," J. Opt. Soc. Am. A 11, 107-117 (1994).

136. D. Kerr, G. H. Kaufmann, and G. E. Galizzi, "Unwrapping of Interferometric Phase-Fringe Maps by the Discrete Cosine Transform," Appl. Opt. 35, 810-816 (1996).

137. Y. Surrel, "Phase stepping: a new self-calibrating algorithm," Appl. Opt. 32, 3598-3600 (1993).

138. P. Picart, J. C. Pascal, and J. M. Breteau, "Systematic Errors of Phase-Shifting Speckle Interferometry," Appl. Opt. 40, 2107-2116 (2001).

139. J. H. Massig and J. Heppner, "Fringe-Pattern Analysis With High Accuracy by Use of the Fourier-Transform Method: Theory and Experimental Tests," Appl. Opt. 40, 2081-2088 (2001).

140. B. Kemper, D. Dirksen, J. Kandulla, and G. von Bally, "Quantitative Determination of Out-of-Plane Displacements by Endoscopic Electronic-Speckle-Pattern Interferometry," Opt. Commun. 194, 75-82 (2001).

141. D. I. Farrant, J. N. Petzing, and J. R. Tyrer, "Geometrically qualified ESPI vibration analysis of an engine," Opt. Las. Eng. 42, 659-671 (2004).

142. C. Joenathan, "Speckle Photography, Shearography, and ESPI" in *Optical Measurement Techniques and Applications*, P. K. Rastogi, ed. (Artech House, Boston, 1997).

143. W. Osten, "Application of Optical Shape Measurement for the Nondestructive Evaluation of Complex Objects," Opt. Eng. 39, 232-243 (2000).

144. D. I. Farrant and J. N. Petzing, "Sensitivity errors in interferometric deformation metrology," Appl. Opt. 42, 5634-5641 (2003).

145. Ch. De Veuster, P. Slangen, Y. Renotte, L. Berwart, and Y. Lion, "Influence of the geometry of illumination and viewing beams on displacement measurement errors in interferometric metrology," Opt. Commun. 143, 95-101 (1997).

146. D. Albrecht, "Estimation of the 2d Measurement Error Introduced by in-Plane and Out-of-Plane Electronic Speckle Pattern Interferometry Instruments," Opt. Las. Eng. 31, 63-81 (1999).

147. W. S. W. Abdullah, J. N. Petzing, and J. R. Tyrer, "Wavefront Divergence: a Source of Error in Quantified Speckle Shearing Data," J. Mod. Opt. 48, 757-772 (2001).

148. H. J. Puga, R. Rodriguez-Vera, and A. Martinez, "General Model to Predict and Correct Errors in Phase Map Interpretation and Measurement for Out-of-Plane Espi Interferometers," Opt. Laser Technol. 34, 81-92 (2002).

149. A. Martinez, R. Rodriguez-Vera, J. A. Rayas, and H. J. Puga, "Error in the Measurement Due to the Divergence of the Object Illumination Wavefront for in-Plane Interferometers," Opt. Commun. 223, 239-246 (2003).

150. S. Schedin, G. Pedrini, H. J. Tiziani, and F. Mendoza Santoyo, "Simultaneous three-dimensional dynamic deformation measurements with pulsed digital holography," Appl. Opt. 38, 7056-7062 (1999).

151. G. D. Byrne, S. W. James, and R. P. Tatam, "A Bragg Grating Based Fibre Optic Reference Beam Laser Doppler Anemometer," Meas. Sci. Technol. 12, 909-913 (2001).

152. E. Chehura, C. C. Ye, and R. P. Tatam, "In-Line Laser Doppler Velocimeter Using Fibre-Optic Bragg Grating Interferometric Filters," Meas. Sci. Technol. 14, 724-735 (2003).

153. J. D. V. Robles, D. Harvey, and J. D. C. Jones, "Automatic Heterodyning in Fiber Optic Speckle Pattern Interferometry Using Laser Velocimetry," Opt. Eng. 31, 1646-1653 (1992).

154. Polytec, "Model 302 LDV," Manual (1995).

155. Lister-Petter, Private Communication (1999).

156. J. M. Huntley and J. R. Buckland, "Characterization of Sources of 2-Pi Phase Discontinuity in Speckle Interferograms," J. Opt. Soc. Am. A 12, 1990-1996 (1995).

157. David Marr, *Vision : a computational investigation into the human representation and processing of visual information* (W.H. Freeman, San Francisco : 1982).

158. Andrew Blake and Michael Isard, *Active contours : the application of techniques from graphics, vision, control theory and statistics to visual tracking of shapes in motion* (Springer, London : 1998).

159. F. J. Harris, "On the use of windows for harmonic analysis with the discrete Fourier transform," Proc. IEEE 66, 51-83 (1978).